Summer 2016

Implementation and modeling of in situ magnetic hyperthermia

Joel Coffel
University of Iowa

IMPLEMENTATION AND MODELING OF IN SITU MAGNETIC HYPERTHERMIA

by

Joel Coffel

A thesis submitted in partial fulfillment
of the requirements for the Doctor of Philosophy
degree in Chemical and Biochemical Engineering in the
Graduate College of
The University of Iowa

August 2016

Thesis Supervisor: Associate Professor Eric E. Nuxoll

Graduate College
The University of Iowa
Iowa City, Iowa

CERTIFICATE OF APPROVAL

_____

PH.D. THESIS

_____

This is to certify that the Ph.D. thesis of

Joel Coffel

has been approved by the Examining Committee for
the thesis requirement for the Doctor of Philosophy degree
in Chemical and Biochemical Engineering at the August 2016 graduation.

Thesis Committee: _____
Eric E. Nuxoll, Thesis Supervisor

_____
Julie L. P. Jessop

_____
Ching-Long Lin

_____
Syed Mubeen

_____
David G. Rethwisch

ABSTRACT

Health-care associated infections (HAIs) on medical implant surfaces present a unique challenge to physicians due to their existence in the biofilm phenotype which defends the pathogen from antibiotics and the host's own immune system. A 2004 study in the U.S. showed that 2 to 4% of implanted devices become infected and must be treated via surgical explantation—a process that is both expensive and dangerous for the patient. A potential, alternative strategy to antibiotics and surgery is to use heat delivered wirelessly by a magnetic coating. This thermal treatment strategy has the potential to kill these HAIs directly on the implanted surface and without the patient requiring surgery.

This thesis introduces an iron oxide nanoparticle composite coating that is wirelessly heated using energy converted from an alternating magnetic field. Iron oxide nanoparticle composites are demonstrated to be remotely heated in both hydrophilic and hydrophobic polymer composites. In designing the composite coating, multiple parameters were investigated for how they impact the normalized heating rate of the material. Specifically, the amount of iron in the coating, the coating thickness, the polymer type, and the orientation of the coating relative to the applied magnetic field were investigated. Power output was shown to increase proportionally with iron loading whereas nearly two times the amount of power output was observed for the same coatings positioned parallel to magnetic field lines versus those positioned perpendicular—a result believed to be due to magnetic shielding from neighboring particles.

Microscope slides coated with 226 μm of composite delivered up to 10.9 W cm^{-2} of power when loaded with 30.0% Fe and positioned parallel in a 2.3 kA m^{-1} AMF. *Pseudomonas aeruginosa* biofilms were grown directly on these coatings and heated for

times ranging from 1 to 30 min and temperatures from 50 to 80 °C. Less than one order of magnitude of cell death was observed for temperatures less than 60 °C and heat shock times less than 5 min. Up to six orders of magnitude reduction in viable bacteria were observed for the most extreme heat shock (80 °C for 30 min).

Introducing this wirelessly heated composite into the body has the potential to kill harmful bacteria but at the risk of thermally damaging the surrounding tissue and organs if the treatment is not designed and predicted intelligently. Thermal energy will propagate differently depending on the surrounding heat sink, with convective heat sinks (*i.e.* those due to blood flow) requiring much more power to reach the same surface temperature than a conduction-only heat sink. To study how heat is transferred in biological tissues, a robust, poly(vinyl alcohol) tissue phantom was developed that can be poured to accommodate any geometry, is volume stable in water and under thermal stress, and can be modified with inert particle fillers to adjust its thermal conductivity from 0.475 to 0.795 W m^{-1} $°C^{-1}$. *In vitro* heat transfer was measured through this hydrogel tissue phantom with at least 10 °C of temperature rise, penetrating 5 mm of tissue in less than 120 sec for an 80 °C boundary condition.

A computational model was used to solve three-dimensional energy transfer through a combined fluid mimic/tissue mimic heat sink spanning the same surface boundary condition. The model was validated with experimental models using a custom designed heat transfer station. This scenario is applicable in the instance where the same coating is subject to starkly different heat sinks: half subject to convective heat loss, half to conductive heat loss. Based on these conditions, a magnetic coating would need to be designed that has a power gradient up to 15 times larger on the fluid half versus the other.

PUBLIC ABSTRACT

Millions of medical devices are implanted in patients annually; of these, hundreds of thousands become infected on difficult-to-treat implant surfaces such as artificial hip joints, bone pins, catheters, and cardiac devices. The bacteria that cause these infections are highly resistant to antibiotics and the patient's immune system. Consequently, the majority of infected devices are surgically removed to treat the infection with a subsequent additional surgery to replace the implant. The complications resulting from medical device infections cost patients and hospitals upwards of $5 billion annually, in addition to costing the patient a diminished quality of life. This work develops a material that can be used to remotely treat (*i.e.* without having the patient go under the knife) implanted medical device associated infections with heat energy delivered from a magnetic coating. By increasing the temperature of the bacteria using wirelessly delivered energy, a potential treatment is developed that does not rely on any drugs or chemicals (to which bacteria can develop resistance) or invasive surgery techniques. Wirelessly heated coatings were developed that can heat bacteria grown on their surface to temperatures as hot as 175 °F. These coatings are shown to kill bacteria that cause medical device infections to non-quantifiable levels. Additionally, by modeling the heat transfer from this coating in the human body, we can predict how much power is needed by the magnetic coating and how to deliver the treatment safely without causing severe thermal damage to the tissue and organs surrounding the medical device in the patient.

TABLE OF CONTENTS

LIST OF TABLES

LIST OF FIGURES

CHAPTER 1: INTRODUCTION

1.1 Infections associated with medical implants

Even in the twenty-first century, medical implant associated infections continue to plague doctors and patients. In fact, nearly 4% of all implanted devices will become infected, costing patients an additional $7,300 to $34,700 in medical expenses per infection event.[1-2] A recent study found that 25.6% of all hospital acquired infections (HAIs) are related to a medical device, while 21.8% of HAIs are a result of patient surgery whether or not a device was implanted.[3]

Current methods used to prevent implanted medical device infections include pre-surgical sterilization of the implant and antibiotic treatment.[3] Despite increasingly stringent sterilization protocols, infection rates remain unchanged and treatment is largely limited to post-surgery device explantation and replacement. Implementation of antibacterial and non-fouling surfaces are two common areas of research aimed at preventing infection but fail to combat all pathogenic strains without being toxic or eliciting an unwanted biological response.[4,5] It is well established that antibiotics alone cannot always cure these infections.[4] Resistance to antibiotics is not only due to genetic mutations, but also because the bacteria thrive in surface colonies called biofilms which are inherently more resistant to drugs. This combined evidence suggests infections on implanted surfaces cannot be prevented. Conclusively, developing a treatment strategy that avoids device explantation and deactivates infections—regardless of genotype—is the only viable solution.

1.2 Biofilms

1.2.1 Definition

Biofilms are colonies of bacteria that exist in a low-metabolism, low-oxygen environment with up to 90% of their volume being comprised of a protective, polysaccharide-dense matrix called extracellular polymeric substance (EPS).[5-6] Commonly observed as a thick slime found in moist environments such as faucets, ship hulls, and teeth, biofilms can form on any surface under favorable conditions—including medical implants.[7-9] Biofilm colonies on medical implants form after a foreign surface has been surgically placed inside the body.[1] Once colonized, these bacteria can persist to elicit an infection in the respective patient post implantation.

The formation of a biofilm occurs once a free floating, or planktonic, bacteria attaches to a surface as depicted in Figure 1.1.[6]

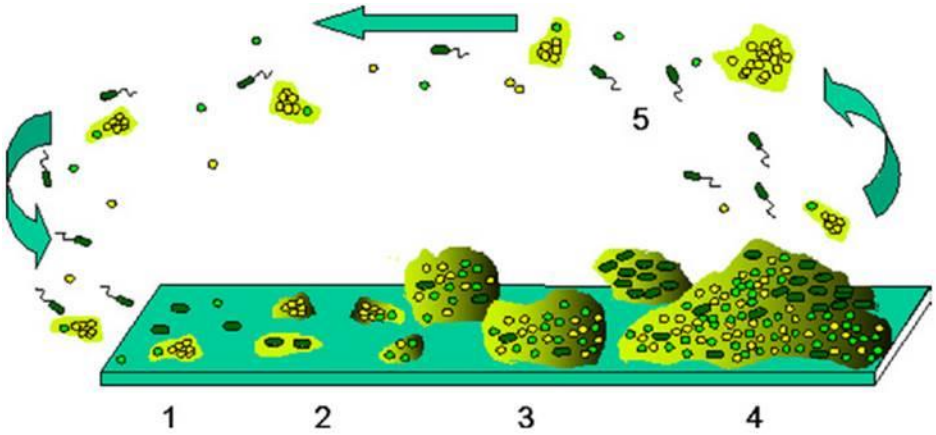

Figure 1.1. Bacteria attach to surfaces to form a biofilm. Planktonic, or free-floating, bacteria will attach to a surface and irreversibly begin producing EPS (1 and 2) followed by early expansion of the biofilm (3) which can contain multiple species of bacteria, expressing different proteins based on their location in the biofilm. Biofilms mature when the bacteria are at a pseudo steady state (4) which leads to detachment of bacteria (5) and reversion to planktonic phenotype. Obtained from Ref. 5 which was adapted from Ref. 6.

This adhesion triggers different gene expression (up to 70% different proteins expressed) which results in immediate production of the EPS.[10-11] The EPS enables cell-cell

communication through chemical signals which result in phenotypic heterogeneity throughout the biofilm with older bacterial cells (referred to as persister cells) in the center of the colony resting at a diminished metabolic rate compared to planktonic cells.[12] The combination of these factors set the stage for bacteria to form very resilient, pathogenic colonies with increased resistance to antibiotics, dehydration, metals toxicity, and UV light exposure.[5, 13] From an evolutionary stand point, the biofilm phenotype is a remarkable protection mechanism that make the residing bacteria very difficult to kill, especially in a patient where the patient's safety must also be considered when designing various preventative and treatment strategies.

Of the tens of millions of devices that are implanted in the human body annually, catheters are the most susceptible to causing infection.[14-15] One account estimates that urinary catheters make-up 40% of all infections acquired in a hospital setting.[16-17] Fortunately, catheter-associated infections are more easily treated due to both their removable nature and the use of a technique known as catheter-lock which exposes the bacteria on the catheter to a higher dose of antibiotic than could normally be tolerated by the patient if delivered to the patient's blood stream.[18]

Still, biofilms infect other types of medical devices such as orthopedics, hernia meshes, sutures, and cardiovascular implants but at a much lower rate than catheters: 4.3% of orthopedic devices and 7.4% of cardiovascular implants.[19] The fully-implanted nature of these devices makes them much more difficult to treat with antibiotics. Consequently, nearly all infections associated with these types of implants can only be treated by surgically removing and replacing the device from the patient in a procedure known as revision surgery.[5, 20]

Research that aims to propose alternatives to revision surgery fall into two general categories: 1) those which prevent bacterial adhesion through non-fouling, or protein resistant, coatings and 2) surfaces laden with antibiotic compounds that diffuse to deactivate the bacterial cells.[21-22] Bone cement compounds mixed with antibiotics are used in total joint arthroplasty, but even these compounds have still been shown to become infected.[23] To date, no material in clinical use currently exists to fully prevent bacterial attachment or subsequent bacterial death within the biofilm. Moreover, it is unclear whether one mode of surface repellent or antibiotic can be effective against multiple strains of pathogen as most biofilms are heterogeneous in the types of opportunistic bacteria that comprise them (*e.g. Staphylococcus epidermidis, Staphylococcus aureus,* and *Pseudomonas aeruginosa*).

1.2.2 Thermal deactivation

Thermally treating bacteria could be a more universal approach towards targeting multiple types of bacteria on multiple types of medical devices. This technique has proven effective in the food and drug industry as is the case in pasteurization and autoclaving.[24-26] However, the literature for thermal deactivation in this setting is usually reported for planktonic bacteria or at temperatures of boiling or super-heated water which cannot be administered *in vivo*. Biofilms are inherently more resistant to environmental stresses which may not exclude heat treatment. To investigate the effect heat treatment has on biofilms, *P. aeruginosa* biofilms have been thermally shocked at medically accessible times and temperatures ranging from 1 min to 30 min and from 37 °C to 80 °C.[27] In that study, the thermal load was provided by a temperature controlled water bath

and demonstrated up to six orders of magnitude reduction in colony forming units (CFUs) per cm^2 of living bacteria as shown in Figure 1.2.

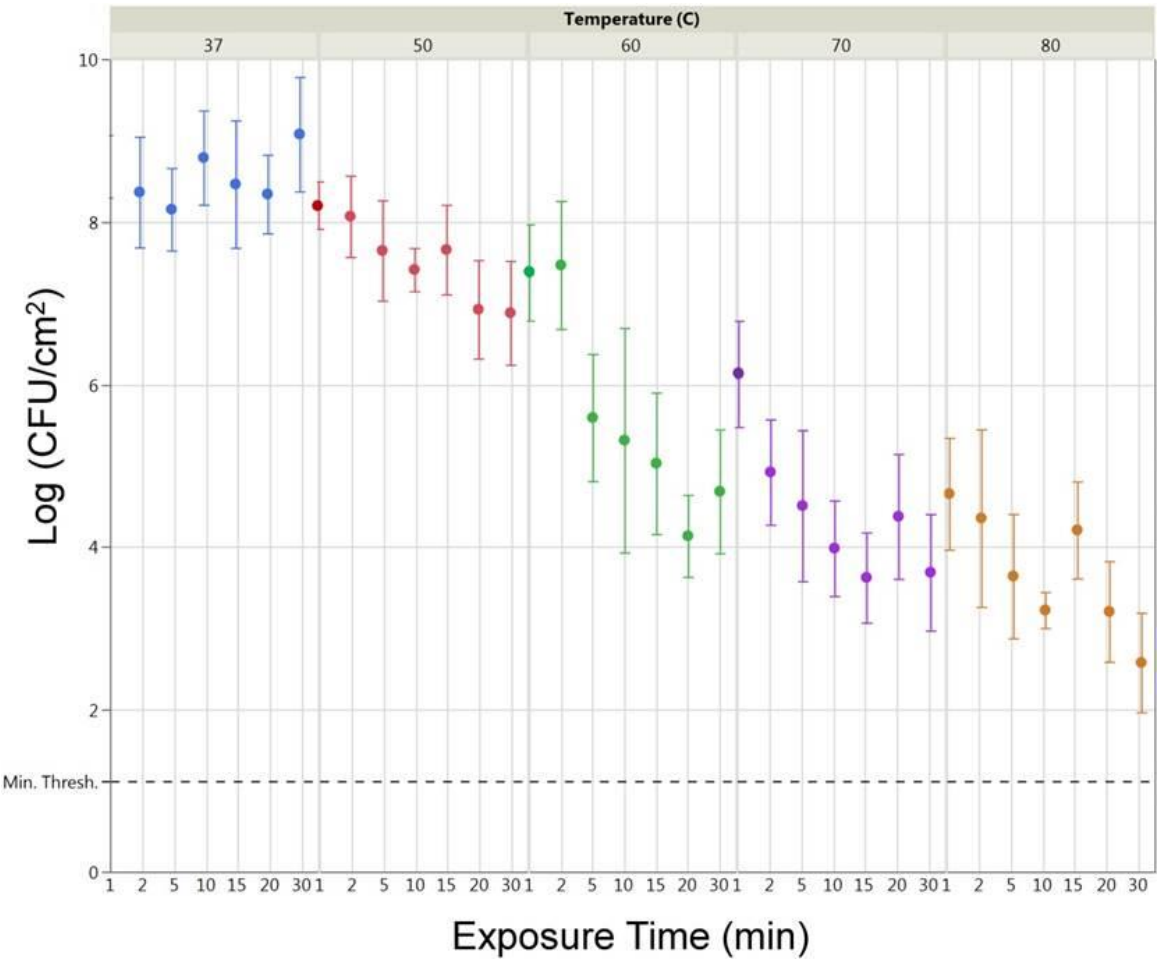

Figure 1.2. Thermal deactivation of biofilms using a water bath heat shock method. *P. aeruginosa* biofilms were cultured with bacterial densities up to 1.7 x 10^9 CFU cm^{-2} on glass microscope slides using a drip-flow reactor (ASTM standard E2647-08). These biofilms were thermally shocked in a temperature controlled water bath at temperatures ranging from 37 °C (controls) to 80 °C. This was done at times ranging from 1 to 30 min for each temperature. The reported data are the remaining, viable CFUs per cm^2, which were enumerated via serial dilution plate counting. Bacteria death for biofilms grown using this method exhibit a stronger dependence on the heat shock temperature than the duration of the heat shock. This figure is from Ref. 27.

For the first time, biofilm cell death was shown to correlate with an Arrhenius-style dependence with temperature and a Weibull-style dependence with time as reported by the equation from Ref. 27 given as Equation 1.1 where x is the concentration of bacteria in the biofilm with units of CFU cm^{-2} and T and t are the deactivation temperature and time, respectively:

Equation 1.1

$$\log(x) = \log(x_0) - [0.079 + 0.044\log(t)](T - 37)$$

These thermal deactivation data for biofilms provide promising results that could enable cell death of hibernating bacteria in biofilms at temperatures that could be feasibly implemented *in vivo.*

1.3 Magnetic hyperthermia

1.3.1 Superparamagnetic iron oxide nanoparticles

Magnetite (Fe_3O_4) nanoparticles are ubiquitous in the field of magnetic nanoparticle (MNP) research for their medical applications in cancer treatment, drug delivery, and as a contrasting agent in diagnostic imaging.[28-31] A widely exploited property of MNPs is their ability to wirelessly heat upon exposure to an alternating magnetic field (AMF); *i.e.*, magnetic induction heating.[32-33] On the nanoscale, (less than 30 nm) iron oxide particles exhibit superparamagnetic behavior affording them the ability to heat more efficiently than larger MNPs.[34] Since the 1950s, magnetite nanoparticles have been used to wirelessly heat specific regions of the body in a process termed magnetic hypertherapy.[35] To date, magnetic hypertherapy has been used almost exclusively for cancer treatment as a means to selectively ablate cancerous cells without damaging the surrounding tissue.[36] While this approach has shown great promise, it is dogged by the critical challenge of dispersing the MNPs throughout the tumor but not in the surrounding tissue.[37-38]

To achieve heating rates from magnetic nanoparticles that can lead to heating and killing of bacteria on implant surfaces, nanoparticles can be distributed throughout a

polymer composite matrix. Such polymer/magnetite composites can be used to create a coating or film that avoids the dispersion problems faced in cancer therapy and localizes the heat source to the precise location needed with more accurately controlled and predicted heating rates.

Remote heating of biofilms using magnetite nanoparticles has been demonstrated before by Park *et al.*[39] In that study, *P. aeruginosa* biofilm colonies were grown on polycarbonate coupons. The biofilms were then doped with aqueous magnetite nanoparticle suspensions at concentrations ranging from 10 to 60 mg mL^{-1}; these coupons were then placed in a constant AMF strength coil for 8 min. Thus, targeting specific deactivation temperatures was not the objective of this study; rather, the transient temperature of the biofilm was monitored with an infrared thermal camera given a specific nanoparticle concentration. For the most extreme 60 mg mL^{-1} case, the biofilm was heated to 60 °C for 5 min after 3 min of temperature rise and exhibited four orders of magnitude reduction in viable bacteria. Since steady temperatures were not achieved until after 38% of the total treatment time, it is difficult to correlate deactivation temperature or exposure time with cell death. Further, the obvious pitfalls of using an injectable magnetic suspension to target exact locations in the body were discussed previously in the case of targeting tumor cells. The benefit of the magnetic composite coating is that the energy is localized to produce a nearly uniform temperature field at the exact location where the bacteria are growing. The increased power loading provided by the coating also allows nearly instantaneous application of a temperature boundary condition at the coating's surface.

1.3.2 Magnetic specific absorption rate

The key parameter for measuring the heating rate in a magnetically susceptible material is its magnetic Specific Absorption Rate (SAR), defined as the thermal power provided by a magnetite composite film divided by the weight of iron in the film. SAR values reported in literature for magnetic fluid hyperthermia suspensions in water vary widely. For example, 15 nm, chitosan-coated, Fe_3O_4 nanoparticles will heat 50% more (119 W g^{-1}) than non-coated particles due to increased dispersion as a result of the hydrophilic coating.[40] Commercially available particles from Micromod exhibit a wide, but relatively low, range of heating (4 – 90 W g^{-1}), while 70 nm magnetic vortex nanorings demonstrate perhaps the most remarkable efficiency (2213 W g^{-1}).[41-42] Most current hyperthermia suspensions have iron concentrations of 0.1 to 5 mg Fe mL^{-1}, which are then dispersed throughout the tissue. As will be shown in Chapters 3 and 5, power loads exceeding 4.5 W cm^{-2} of heating would be needed to deactivate biofilms inside the body. Even magnetite nanoparticles with a SAR of 1000 W g^{-1} would need to be concentrated to *300* mg Fe mL^{-1} in a 150 μm thick coating to provide this power density. Thus, any polymer/magnetite material must have an MNP loading orders of magnitude larger than current materials, which may introduce significant particle-particle interactions and aggregation potential that complicate the design of an effective implant coating. This application may also require mechanical moduli significantly different from current magnetic composites.

Magnetite composites of poly(vinyl alcohol) (PVA), poly(ethylene glycol), poly(N-isopropylacrylamide), and poly(acrylamide) have all been reported to wirelessly heat in an AMF, though they are too soft in aqueous environments to be appropriate for

orthopedic devices which comprise the largest share of the medical implant market.[1, 43-46] Moreover, these composite materials were not prepared with large enough iron loadings to meet the power demands described above, nor were they tested with any rigor for determining how the composite will heat differently for different iron loadings as will be shown in Chapter 2 for magnetic composites made with PVA and hydrophobic poly(styrene).

1.4 Heat transfer in biological tissues

Perhaps the greatest challenge towards heating surfaces inside the body is concern over heat propagation into the surrounding tissue and blood vessels that may irreversibly damage these tissues and cause patient harm. Determining the heat transfer for such scenarios usually involves one or more of the following methods: direct *in vivo* temperature measurement,[47-48] numerical modeling,[49-51] and *in vitro* modeling using tissue phantoms.[52-55] *In vivo* measurements have obvious availability issues and can explore only a limited region of parameter space, while some scenarios require additional coupled processes which are not accurately incorporated computationally (*e.g.*, bacterial cultures).

Many analytical and numerical solutions exist that model the heat transport (often termed 'bioheat transfer') through blood-perfused tissue.[49-51] Rarely are these models validated with experimental temperature measurement due to the difficulty in mimicking physiological conditions. Nearly all models are derived from Pennes' equation formulated in 1948 and given as Equation 1.2 where T_t is the tissue temperature and T_a is the blood artery temperature.[51]

Equation 1.2

$$\rho c_p \frac{\partial T_t}{\partial t} = \nabla k \cdot \nabla T_t + (\rho c)_b \omega_b (T_a - T_t) + q_m$$

This model assumes a local blood/tissue thermal equilibrium effect and accounts for heat effects generated by blood perfusion and cellular metabolism exhibited in native body tissue (second and third terms on the right hand side).

Thermal modeling of the energy transport through tissue is difficult when attempting to predict temperature gradients from iron oxide nanoparticle suspensions used in magnetic hyperthermia. These suspensions cannot be reliably localized to a specific area or volume due to the inhomogeneity of tissue and the cellular uptake of these particles. Thus, defining accurate boundary conditions for thermal modeling, both experimentally and computationally, is nearly impossible. Moreover, defining a source term for the heat generated by a suspension is difficult due to the decrease in magnetic susceptibility as a result of particle-tissue interactions and decreased colloidal stability. Nearly all of these problems (nanoparticle location, accurate boundary conditions, repeatable heating rates) are eliminated when particles are immobilized to a controlled volume or surface such as a coating. For example, Satarkar *et al.* numerically modeled heat transfer from an iron oxide nanoparticle/poly(ethylene glycol) disk.[45] Boundary conditions were specified from experimental SAR measurements generated via magnetic induction heating of the disk in air with a magnetic field strength, *H*, of 25kA m^{-1} operating at a frequency, *f*, of 293kHz. The SAR data was used to correlate a steady state disk surface temperature as a function of iron concentration. For a 5mm diameter disk with 5% iron content surrounded by tissue, the steady state temperature rise of the tissue

directly next to the disk was 13°C (using a finite element model with Equation 1.2 in COMSOL3.4). Despite the lack of comparison between experimental and computational data for the same heat sink condition, this work is a first step in predicting the power requirements from a magnetic/polymer composite for a solid tissue mimic heat sink in the body.

1.5 Tissue phantoms

1.5.1 Hydrogel tissue phantoms

Towards the goal of modeling heat transfer in a setting that mimics biological tissue, this work required a tissue phantom to perform robust experimental heat transfer measurements *in vitro*. Tissue phantoms are key components in the development of many medical advances including the localized application of extreme temperatures within the body (hyperthermia/hypothermia). In principle, these materials allow low-risk experimental investigation of complex phenomena with precisely defined, complex geometries and well-controlled, accurately measured parameters; *e.g.*, phantom size, porosity, temperature, and optical opacity.[56] Current tissue phantoms each have a combination of major drawbacks, however, such as poor reproducibility, poor thermal stability, poor volume control, rapid degradation, inability to achieve complex geometries, and elaborate fabrication protocols. Additionally, tuning the thermal properties of a phantom to match those of various tissues and organs is an important feature. For instance, most biological materials exhibit thermal diffusivities close to water, but the stark variations between that of bone (0.55 ± 0.02 W m^{-1} $°C^{-1}$)[57] , fatty tissue (0.34 W m^{-1} $°C^{-1}$)[58] , and muscle (0.41 ± 0.02 W m^{-1} $°C^{-1}$)[59] demonstrate the need for more tunable phantom properties.

Biomimetic polymer systems have been studied for decades; *e.g.*, agar, gelatin, poly(ethylene glycol), and the more ubiquitous poly(acrylamide) (PAA).[60-61] The advantages and limitations of these hydrogels in modeling heat transfer have been summarized elsewhere.[62-63] For example, gelatin liquefies at temperatures approaching 50 °C, meat decomposes at room temperature, and poly(dimethyl siloxane) exhibits thermal properties significantly different from most tissues. PAA, arguably the most common phantom material, can be polymerized *in situ* to achieve complex geometries with reproducible properties and good thermal stability due to its covalent crosslinking, but its volume stability is poor and difficult to control. Additionally, the thermal properties of a PAA gel can be difficult to tune due to its low pre-polymerization viscosity making it nearly impossible to maintain a dispersion of thermally-modifying fillers.

1.5.2 Poly(vinyl alcohol) hydrogels

Poly(vinyl alcohol) (PVA) is a well-studied polymer which is commercially available at high purity in a wide range of well-controlled molecular weights, combining a robust hydrocarbon backbone with a lining of pendant hydroxyl groups which make it easy to dissolve into a pourable aqueous solution.[64] This combination also makes it readily crosslinkable via a wide range of chemical and physical methods.[65-66] For example, glutaraldehyde (GTA) will form acid-catalyzed acetal linkages which cause the solution to gel, rendering the polymer network insoluble.[67-68] Like most hydrogels, the swelling ratio (volume of dry PVA divided by the volume of swollen PVA) of crosslinked PVA depends on the crosslink density and the degree of crystallinity though

the crystalline volume fraction of chemically crosslinked PVA gels tends to be quite low, making the swelling ratio solely dependent on chemical crosslink density.[69-70]

Conventionally, PVA tissue phantoms have been formed by physically crosslinking the polymer using the freeze-thaw method, in which the PVA solution is cycled through temperature extremes (below -20 °C to room temperature) at controllable cooling and thawing rates.[71-72] While this capitalizes on PVA's biocompatibility by avoiding chemical cross-linkers which may interfere with *in vivo* applications, the resulting fluctuations in the phantom's volume due to the dramatic temperature swings are not amenable to applications with precise geometries, and the resulting crystalline crosslinks are susceptible to dissolution at elevated temperatures. Reproducibly executing the freeze-thaw cycles *in situ* in a variety of geometries may also be experimentally challenging; chemically crosslinking PVA, on the other hand, is experimentally straightforward and generally independent of its surroundings, and produces crosslinks which are stable at higher temperatures.

If the chemical crosslinking is not carefully controlled and systematically optimized, however, the variability in swelling ratio—both batch to batch and in a single phantom over time—can make chemically crosslinked PVA an unattractive candidate as a tissue phantom.

1.6 Thesis objectives

The goal of this thesis is to quantify the thermal output of an iron oxide nanoparticle/polymer composite needed to administer coating surface temperatures inside the body for various heat sink conditions. Additionally, the extent of tissue hyperthermia surrounding this heated surface will be quantified with the long term goal of

implementing a wireless thermal deactivation protocol that can be administered effectively while minimizing tissue damage.

The following specific objectives will be used for accomplishing these goals:

- **Objective 1:** Demonstrate controlled, wireless heating using an iron oxide nanoparticle composite.
- **Objective 2:** Experimentally estimate the power requirements and temperature gradients surrounding composite coatings under different heat sink conditions.
- **Objective 3:** Build a computational model to determine power requirements and thermal profiles under conditions that are not experimentally accessible.

Wireless heating is achieved in Chapter 2 through synthesis of iron oxide nanoparticle composite whose design parameters are investigated for how they affect the composites' normalized heating rates. These composite coatings are then shown in Chapter 3 to wirelessly heat bacteria grown on their surface up to 80 °C. The resulting tissue hyperthermia that would be induced by this coating is explored via a range of heat sink scenarios, from the most extreme case of blood flow to the conduction-dominated heat transfer scenario induced in a tissue phantom heat sink. Such a tissue phantom is systematically designed in Chapter 4 to produce a volume and temperature stable hydrogel whose thermal properties are modified with inert fillers. Experimental temperature profiles are used to validate a computation model in Chapter 5 which is then used to quantify the power loads required by a composite coating which is subject to two different heat sinks across the same surface demonstrating the full range of design parameters that must be considered for implementing this technology.

CHAPTER 2: IRON OXIDE NANOPARTICLE COMPOSITE COATINGS[1]

This chapter compares iron oxide nanoparticles dispersed through two opposing polymer matrices: hydrophilic poly(vinyl alcohol) (PVA) and hydrophobic poly(styrene) (PS). Section 2.6 demonstrates the effect of several design parameters on the normalized power output from these magnetic composites. In particular, magnetite concentration, coating thickness, polymer matrix, and coating orientation (relative to the applied alternating magnetic field) were all investigated. The orientation of the film relative to the magnetic field source is the largest contributor towards affecting the normalized power output of the coating. Composites were produced with large heating power densities which can be supplied from conventional magnetic field generators using materials commonly used in FDA-approved implants.

2.1 Magnetite synthesis

Magnetite nanoparticles were coprecipitated by reacting Fe^{3+} and Fe^{2+} in a 2:1 molar ratio in concentrated potassium hydroxide.[73] $FeCl_3 \cdot 6H_2O$ (6.46 g) and $FeCl_2 \cdot 4H_2O$ (2.38 g) (Sigma Aldrich) were dissolved in 18.1 MΩ·cm DI water (12.5 mL). A nucleated solution of iron oxide nanocrystals was prepared by diluting the iron solution (5 µL) with water (5 mL) followed by the addition of 15 M potassium hydroxide (10 mL) (Fisher Scientific) while vortexing. An ultrasonication probe (Cole-Parmer, model CV33, 0.318 cm probe diameter) operating at 20 kHz and 300 W was submerged into the nucleated reaction vessel while simultaneously dispensing the iron salt solution into the vessel over a 90 s period using a 30 mL syringe fitted with a 22 AWG needle; black, iron oxide nanocrystals precipitated immediately. The reaction vessel was kept at 65 °C for 3 hr to

[1] This work was published on August 25, 2015: Coffel, J.; Nuxoll, E., Magnetic nanoparticle/polymer composites for medical implant infection control. *Journal of Materials Chemistry B* **2015**, 3, 7538-7545

allow for crystal growth via Ostwald ripening.[74] Suspensions were rinsed to remove excess iron, potassium, and chloride ions by centrifuging (The Drucker Company, Model 755V-24) for 5 min at 2400 rpm (using 11.5 cm-long tubes positioned 15 cm away from the centrifuge rotor axis at the bottom of the tube) then decanted, probe-sonicated for 90 s, and re-suspended with DI water (30 mL) via mixing with a vortexer; this process was repeated an additional four times. Non-aqueous suspensions were prepared by rinsing an additional three times with 2-propanol (Fisher Scientific) followed by one rinse with toluene (Fisher Scientific) which was necessary to dissolve the hydrophobic PS resin.

2.2 Magnetite characterization

2.2.1 Particle size and morphology

Particle morphology of superparamagnetic iron oxides is known to strongly influence SAR. Heating efficiency is best achieved with monodiperse particles at a particle size just below the superparamagnetic limit (20 – 30 nm).[33, 75] Iron oxide nanoparticle size was observed via scanning electron microscopy (SEM) using a Hitachi S-4800 electron microscope at 1.8 kV accelerating voltage. The co-precipitation method described in Section 2.1 produced nanoparticles approximately 20 nm in diameter as shown in Figure 2.1, thus conforming to superparamagnetic behavior for optimal heating.

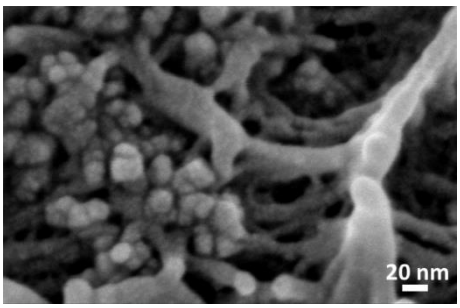

Figure 2.1. SEM image of iron oxide nanoparticles. Nanoparticles synthesized via the co-precipitation method in Section 2.1 are approximately 20 nm spheres which are superparamagnetic. Image shows nanoparticles aggregated in PS polymer matrix.

2.2.2 Iron stoichiometry

Pure magnetite (Fe_3O_4) readily oxidizes at atmospheric conditions to maghemite (γ-Fe_2O_3) in the absence of an encapsulating oxygen barrier and exhibits higher magnetization saturation (84 emu g^{-1})—and thus SAR—than oxidized maghemite (74 emu g^{-1}).[34, 76] To quantify the degree of oxidation of the nanoparticles produced per Section 2.1, the iron stoichiometry (notated as x_D = Fe^{2+}/Fe^{3+} which is 0.5 for pure magnetite and 0.0 for pure maghemite, γ-Fe_2O_3) was measured spectrophotometrically via the phenanthroline method[77] and by interpolating from powder x-ray diffraction patterns (pXRD).[78]

Freshly prepared and rinsed iron oxide nanoparticle suspensions were digested in concentrated HCl in preparation for the phenanthroline method. The iron stoichiometry for these suspensions was x_D = 0.44 ± 0.01 (n = 2) demonstrating that the suspensions were largely unoxidized immediately prior to suspending the nanoparticles in solvent/polymer resin for composite synthesis.

The unit-cell length, a, of a pure magnetite crystal is 8.396-8.400 Å as measured by pXRD. As magnetite oxidizes to maghemite, Fe^{2+} occupied sites are vacated and the unit-cell length decreases; a = 8.33-8.34 Å. Gorski and Scherer previously reported a linear trend of decreasing unit-cell length for decreasing iron stoichiometry in magnetite nanopowders: $a = 0.108x_D + 8.341$; $R^2 = 0.914$; $n = 9$.[78] This trend can be used to interpolate the degree of oxidation of magnetite samples with reasonable accuracy from the pXRD pattern for a dry, magnetite powder sample. These patterns were collected using a Rigaku MiniFlex II system equipped with a Co source (Co$K\alpha$ = 1.7899Å). Samples were analyzed at room temperature from 15-80 °2θ with a 0.02° step size and a

3.0 s dwell time. The unit-cell length was calculated from fitted patterns using Jade 6 software (Materials Data, Inc.); patterns were smoothed, background subtracted, and $K\alpha_2$ stripped prior to fitting. The pXRD pattern for a typical magnetite sample prepared by the co-precipitation method in Section 2.1 matched the peak localities of previously reported magnetite pXRD patterns as shown in Figure 2.2.[78-79] The calculated unit-cell length from the fitted pXRD pattern was 8.379 which corresponds to an iron stoichiometry of 0.352.[77-78] Thus, some oxidation had occurred as a result of drying the suspensions in preparation for pXRD.

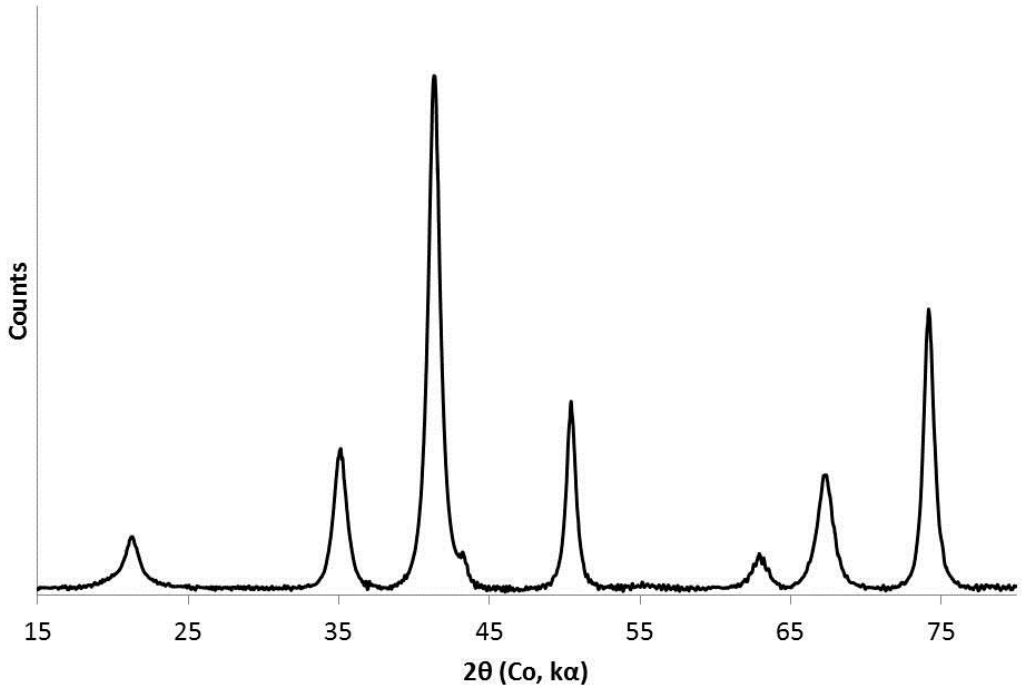

Figure 2.2. pXRD pattern of dry magnetite powder at room temperature.; unit-cell length = 8.379 Å.

Iron stoichiometry could not be measured for magnetite in the composites using either method due to unwanted oxidation of Fe^{2+} at the higher acid concentrations needed to extract and digest the iron from the polymer matrix for the phenanthroline method and interference with the diffraction pattern from the encapsulating polymer. A longevity

study—which measured the power output of coatings over a period of 18 months—was performed to check for any diminished power output over time that would be a result of oxidation; this study is discussed in Section 2.7.

2.3 Composite synthesis

The magnetite nanoparticle suspensions prepared in Section 2.1 were prepared in PVA and PS composite films to compare the influence, if any, the polymer matrix has on the specific absorption rate (SAR). Both polymer matrices were loaded with three distinct iron concentrations and three distinct thicknesses to produce nine composites per polymer.

2.3.1 Poly(vinyl alcohol) composites

Magnetite-loaded PVA (99 mol% hydrolyzed, ~133,000 MW, Polysciences, Inc.) composites were prepared as films via solvent casting with an adjustable doctor blade at 750, 1250, and 1750 µm to produce the thin, medium, and thick films, respectively. PVA composites were prepared from rinsed magnetite suspensions (0.082 g Fe_3O_4 g^{-1} slurry in water ± 0.007) by dissolving 2.0, 4.0, and 8.0 g of PVA powder in suspensions at 90 °C for 10 min under continuous stirring to produce the 18, 28, and 40 wt% Fe in the dry films, respectively. These same films had an iron concentration 60 to 70% lower in their hydrated state due to the hydrogel's swelling ratio. Magnetite-PVA suspensions were cast on poly(tetrafluoroethylene) (PTFE) sheets, covered, and allowed to dry under ambient conditions for 24 hr. Composite films were vacuum dried for an additional 24 hr followed by hydrothermal cross-linking at 150 °C for 3 hr. Magnetite composites dried as uniform,

black films with little to no surface defects. All samples were cut from the bulk film into circular coupons using a 12 mm diameter cork borer.

2.3.2 Poly(styrene) composites

Poly(styrene) (~280,000 MW, Sigma Aldrich) composites were formed by dissolving 3.75, 7.5, and 15 g of PS resin in magnetite-toluene suspensions (0.082 g Fe_3O_4 per g of slurry in toluene) under continuous stirring for 60 min at room temperature to produce 9.0, 18, and 27 wt% Fe dry films, respectively. These iron concentrations closely matched the iron concentrations in the hydrated, PVA films. Magnetite-PS-toluene suspensions were allowed to rest for 30 min at room temperature to eliminate air bubbles, cast on PTFE, dried, and cut into circular coupons in the same manner as PVA composites.

2.3.3 Film thickness and iron concentration

Dried film thicknesses were measured using a hand-held micrometer (Mitutoyo, ± 0.001 mm). The total iron concentration was measured in each coupon by digesting the dry composites in 8 M HCl (5 mL) for 24 hr, reducing all iron species to Fe^{2+} with 10% hydroxylamine hydrochloride, complexing with 1% 1,10-phenanthroline monohydrate, buffering with 3.7 M ammonium acetate, (Sigma Aldrich) and measuring the absorbance of 510 nm light with a UV/Vis spectrophotometer (Cary 50, Varian Inc.). The total weight of iron was divided by the total, dry coupon weight to calculate the wt% Fe in each composite; these values varied less than 3.4% from the mean value for all coupons cut from the same film.

2.3.4 SEM composite imaging

Polymer-magnetite composites were prepared for SEM imaging by freeze fracturing the composite film using liquid nitrogen and then sputter coating the fractured edge with 1 – 2 nm of gold-paladium (5 mA, 60 s coating time, Emitech Sputter Coater K550). SEM images of the nanoparticles distributed throughout both polymer matrices are shown in Figure 2.3.

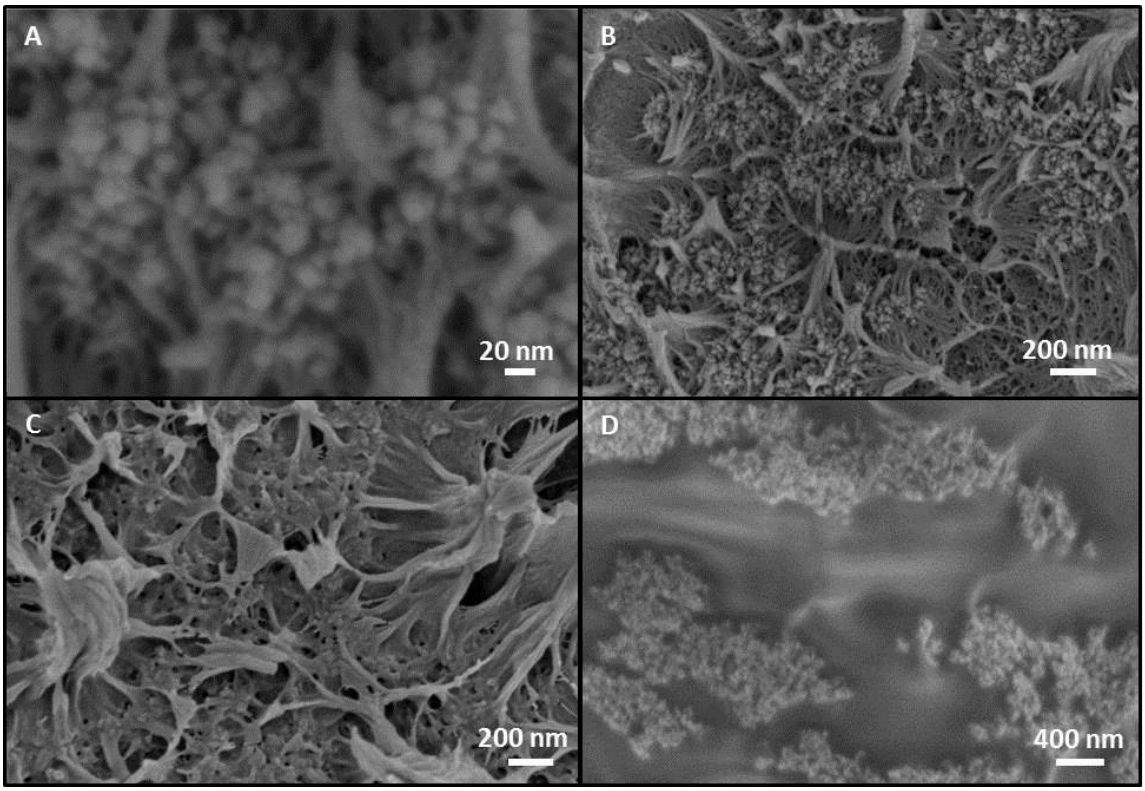

Figure 2.3. SEM images of iron oxide nanoparticles in composites. Images of composite cross-sections for magnetite nanoparticles in PS (A and B) PS matrix after magnetite removal via acid digestion (C) and magnetite nanoparticles in PVA (D).

2.4 Alternating magnetic field (AMF) mapping

Composites were heated using a 6-turn, 53-mm tall solenoid supplied by a 7.5 kW AMF generator (MSI Automation, Inc.) operating at 302 kHz with an rms current of 19.8 A at maximum power. To confirm the uniformity of the AMF generated by the induction coil, the magnetizing field strength, *H*, was measured throughout the sample chamber

using a custom-built magnetometer probe. The probe measured the potential, ε, induced in the probe coil (an 8-turn, 1.90 mm-diameter, 5 mil tungsten wire solenoid) when placed in the AMF generated by the 52 mm-diameter induction coil. From the measured ε, the magnetic flux density, B, was calculated using Equation 2.1 derived for a solenoid from Ampere's and Faraday's Law where f is the AC frequency, N_P is the number of turns in the probe coil, and A_P is the cross-sectional area of the probe coil.

Equation 2.1

$$B_{\text{probe}} = \frac{\varepsilon_{\text{probe}}}{2\pi f N_{\text{p}} A_{\text{p}}}$$

Conversion of the magnetic flux density, B, in units of gauss to the magnetic field strength, H, in oersted is equal to unity in a vacuum; conversion from oersted to A m^{-1} is a factor of 79.58. The measured H-field was 2.32 kA m^{-1} at the center of the coil at maximum power. This value was in good agreement with the theoretical calculation of the field strength from the rms current in the coil, I, the coil length, L, and the number of turns in the coil, N; i.e., $B = \mu NI/L$ = 28.2 gauss = 2.24 kA m^{-1} where μ is the permeability constant equal to $4\pi \times 10^{-7}$ in SI units. Mapping measurements were taken at the center and around the circumference of the 16 mm-diameter sample chamber at multiple planes along its 17 mm height as shown in Figure 2.4.

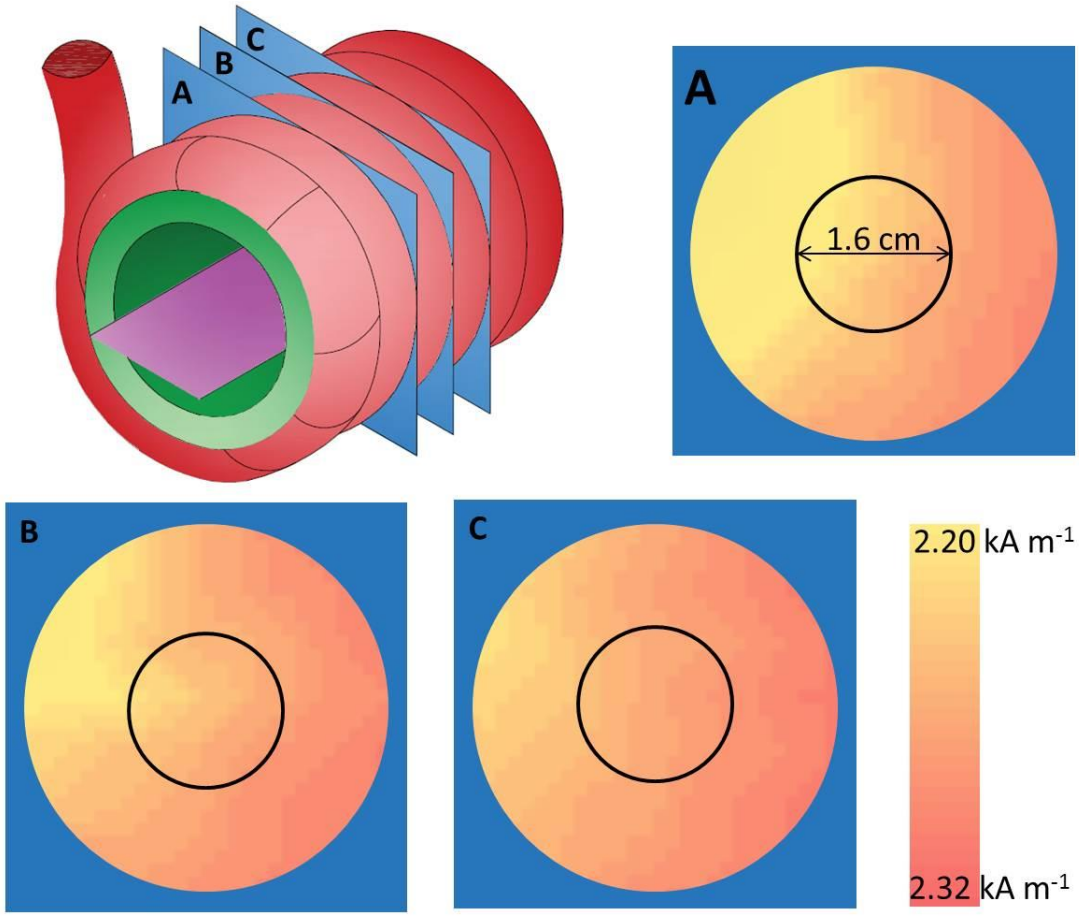

Figure 2.4. Alternating magnetic field mapping. Values are the measured magnetic field strength, H, in kA m^{-1} at three planes along the coil height. Mapping indicates less than 1% variation in field strength from the average throughout the entire volume used for heating the composites.

2.5 Specific absorption rate (SAR) measurement

Transient temperature measurements of the solvent surrounding the composite were collected using a minimum of six fiber optic temperature probes (0.170 mm OD, ± 0.3 °C, Opsens) and an 8-channel data acquisition device (USB-TEMP, Measurement Computing) using LabVIEW software (National Instruments). The solvent and composite were placed in a 3 mL plastic-well sample chamber which was placed in an insulating, 1.3 cm-thick styrofoam holder as shown in Figure 2.5. Temperature measurements were collected every second for all temperature probes.

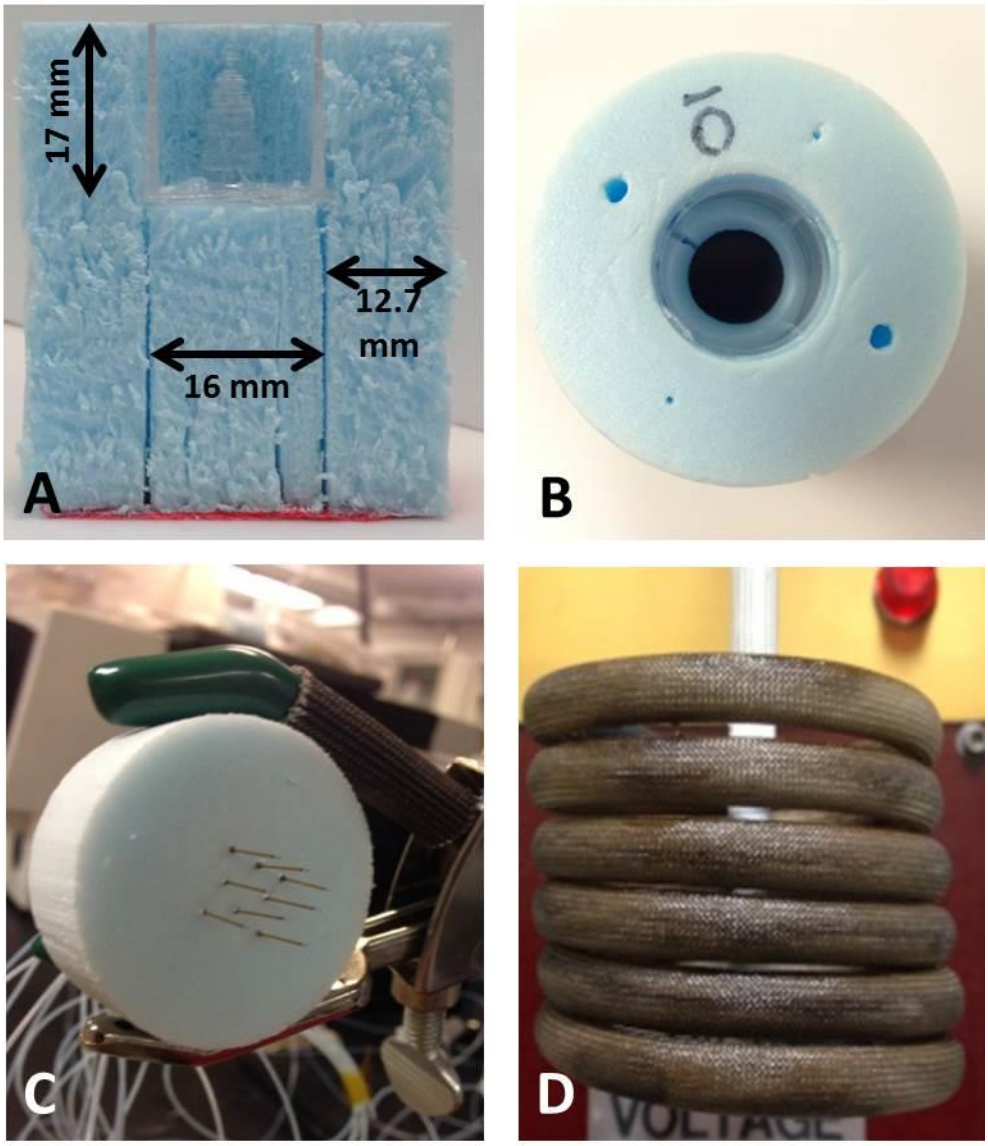

Figure 2.5.Foam holder used for SAR measurements. A) Cross-section of foam sample holder with polystyrene-lined sample chamber. B) Top-view of sample holder/chamber with 12 mm composite coupon in the perpendicular orientation. C) sample holder lid with 8 fiber optic temperature probes. D) side-view of 52 mm AMF coil.

The SAR was calculated from transient temperature data using Equation 2.2 which is a simplified energy balance on the sample chamber assuming no heat loss to the environment, negligible spatial gradients in temperature, and negligible heat transfer resistance between the composite-solvent interface.

Equation 2.2

$$\text{SAR} = m\frac{c_P}{x_{Fe}} \text{ where } m = \frac{\Delta T_{avg}}{\Delta t}$$

where m is the slope of the $T_{avg}(t)$ curve calculated over a time period, Δt, in which the temperature in the sample chamber rose 5 °C. Thus, for a large slope (m = 0.3 °C s^{-1}) the time period for calculating m is less than the period for a small slope (m = 0.03 °C s^{-1}) but over the same temperature range; *i.e.,* ΔT = 5 °C for all SAR calculations. T_{avg} is the average temperature recorded from all temperature probes; c_p is the weighted heat capacity of both the solvent and plastic-well (3.50 J g^{-1} K^{-1} for all water trials and 2.2 J g^{-1} K^{-1} for all dodecane trials); x_{Fe} is the weight fraction of iron in the heated sample chamber calculated from the wt% Fe in the coupon and the weights of the sample well, solvent, and coupon in the sample chamber. All slopes were corrected for the amount of heat conducted into the chamber from the induction coil during the same 5 °C temperature rise used to calculate m via an iron-free control as shown in Figure 2.6. Additional controls which used PS and PVA composites made without iron oxide nanoparticles were also heated in the coil. The heating rate for these controls were identical to the solvent-only controls shown in Figure 2.6B and C, suggesting no magnetic susceptibility of the polymers on their own.

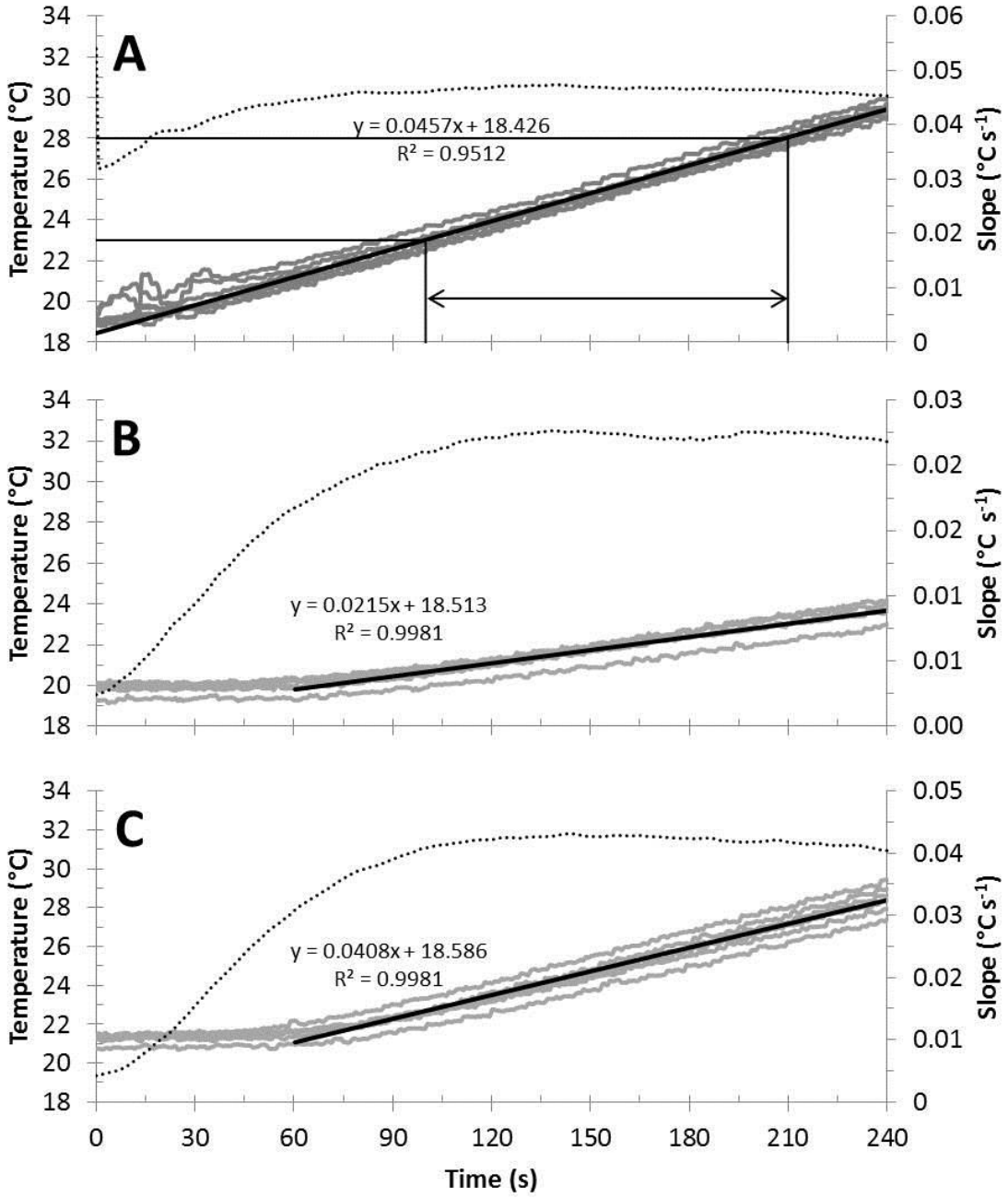

Figure 2.6. Temperature profiles for calculating SAR. A) Transient temperature rise in sample chamber for a 9.0wt% Fe, 81 µm-thick PS composite in water, orientated perpendicularly to AMF. B) Temperature rise in water and C) dodecane for an iron-free control indicating heat transfer into system from induction coil. Grey lines indicate measurements from all 8 temperature probes (left, vertical axis); solid black line indicates linear fit to average of all temperature measurements; dotted line indicates transient slope, *m*, from Equation 1 (right vertical axis); vertical and horizontal black lines in (A) indicate Δt used in calculating SAR that corresponds to a 5 °C temperature rise.

2.6 Composite parameters that affect SAR

Composites were tested in water (2.7 mL) and dodecane (2.5 mL) (Sigma Aldrich) to investigate the effect of swelling behavior on SAR for the PVA composites; PS composites did not swell in either solvent. Composite films were positioned both parallel and perpendicular to magnetic field lines to investigate the effect of orientation on SAR. SAR measurements were collected for these parameters for both polymer types across all film thicknesses and iron concentrations and are tabulated in Table 2.1.

Table 2.1. Magnetite/polymer composite properties and corresponding SAR values; $n = 3$.

Polymer	Dry wt% Fe	Dry film thickness (μm)	SAR (W g^{-1}) in water, ⊥ AMF	SAR (W g^{-1}) in dodecane, ⊥ AMF	SAR (W g^{-1}) in water, ∥ AMF	SAR (W g^{-1}) in dodecane, ∥ AMF
PS	8.9 ±0.1	81 ±1	289 ±29	264 ±32	489 ±43	448 ±26
PS	8.9 ±0.0	139 ±2	311 ±18	269 ±17	451 ±82	460 ±35
PS	9.3 ±0.1	182 ±0	329 ±12	293 ±15	485 ±87	420 ±30
PS	18.7 ±1.0	78 ±2	242 ±28	218 ±14	439 ±29	416 ±26
PS	19.5 ±0.1	129 ±8	261 ±14	253 ±11	488 ±23	468 ±32
PS	16.6 ±0.1	211 ±2	282 ±19	279 ±17	498 ±29	489 ±53
PS	27.4 ±0.9	68 ±3	209 ±14	193 ±35	499 ±28	451 ±41
PS	26.4 ±0.2	105 ±5	239 ±15	238 ±36	547 ±18	444 ±28
PS	26.1 ±0.0	193 ±19	250 ±10	290 ±48	562 ±37	489 ±26
PVA	17.6 ±0.6	45 ±6	322 ±30	203 ±29	626 ±37	623 ±44
PVA	17.6 ±0.1	63 ±3	329 ±18	196 ±15	636 ±51	652 ±48
PVA	17.6 ±0.1	98 ±5	361 ±15	221 ±15	717 ±33	681 ±25
PVA	28.1 ±0.2	39 ±1	359 ±28	141 ±22	666 ±53	611 ±55
PVA	27.9 ±0.1	68 ±2	308 ±29	193 ±14	633 ±26	561 ±61
PVA	28.3 ±0.4	109 ±1	336 ±19	153 ±17	637 ±29	640 ±26
PVA	39.7 ±0.1	40 ±1	188 ±18	116 ±32	656 ±37	618 ±29
PVA	40.0 ±0.2	68 ±2	207 ±12	123 ±22	574 ±36	586 ±23
PVA	40.2 ±0.5	97 ±12	330 ±50	100 ±10	574 ±46	714 ±35

2.6.1 Orientation relative to AMF

The change in the coating's orientation relative to the magnetic field results in the most dramatic difference in SAR as shown in Figure 2.7 which organizes all SAR data from Table 2.1 by polymer type, orientation to the AMF, and the solvent in which the composite was heated.

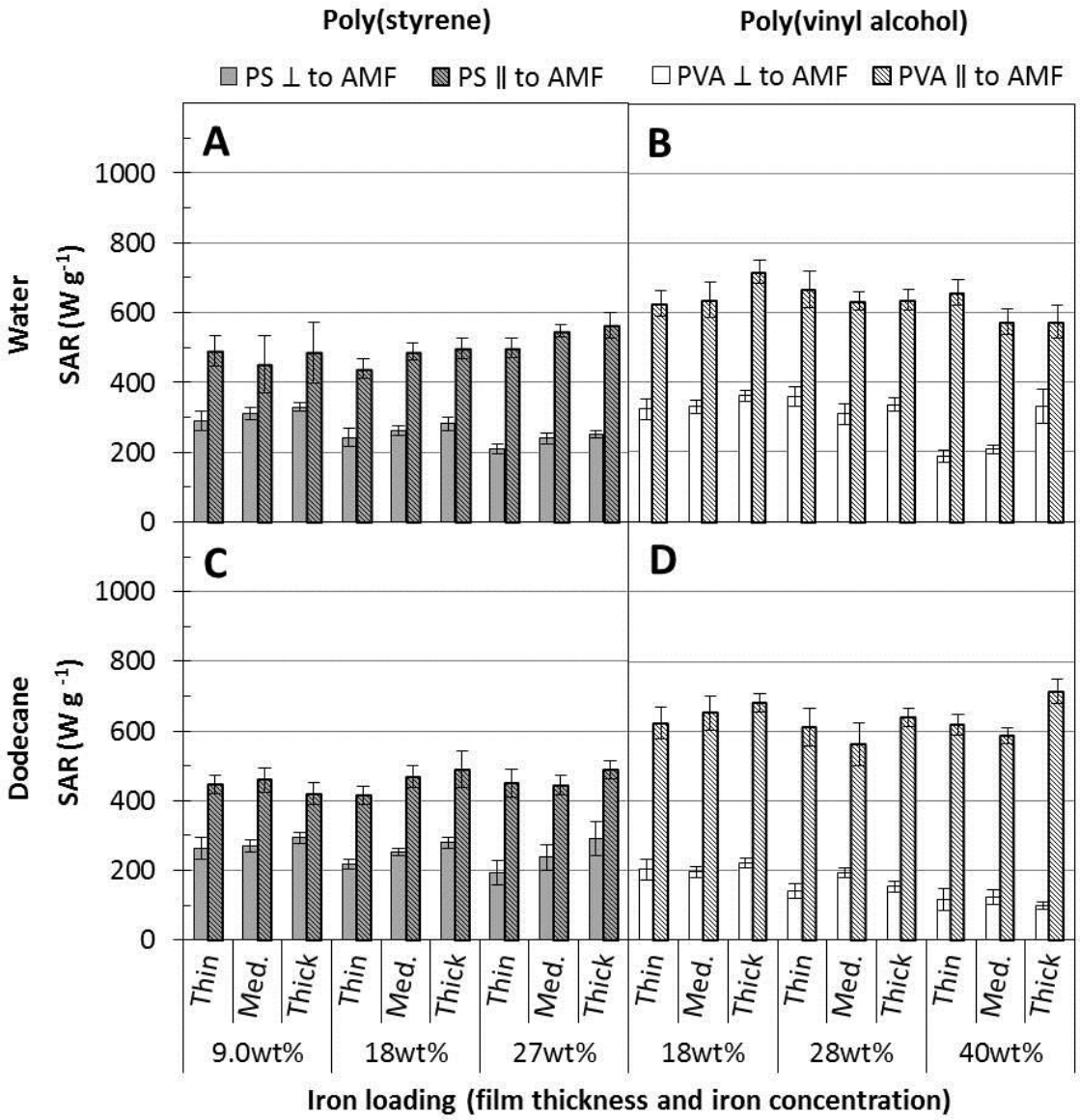

Figure 2.7. Compiled SAR data for PVA and PS composites for all thicknesses and iron concentrations; all samples were tested in positions perpendicular and parallel to the applied AMF in water (A and B) and dodecane (C and D); n = 3 for all measurements.

Films exhibited twice (1.96 ± 0.50) the heating power when aligned parallel to magnetic field lines than the same film in the perpendicular orientation. The effect is even more pronounced in PVA/dodecane (Figure 2.7D) where SAR increased by a factor of 4.19 ± 1.54 due to the polymer's swelling capabilities as discussed next in Section 2.6.2. While mapping indicated less than 1.0% variation in field strength across the 3 mL chamber volume (see Figure 2.4), the field strength experienced by a given MNP decreases as more magnetically-susceptible material is situated between it and the generating coil. In this study, no MNP in a parallel-oriented coating has more than 210 µm of magnetic composite between it and the AMF source. By contrast, an MNP at the lateral center of a perpendicularly-oriented coating has 6.0 *mm* of magnetic composite between it and the AMF source. This effect was further observed by measuring the temperature of a composite's surface during the first 15 – 20 s of heating using spatially varied temperature probes across the coupon's surface as shown in Figure 2.8. The center of the coating heated the slowest, despite having far less heat sink volume than the edge.

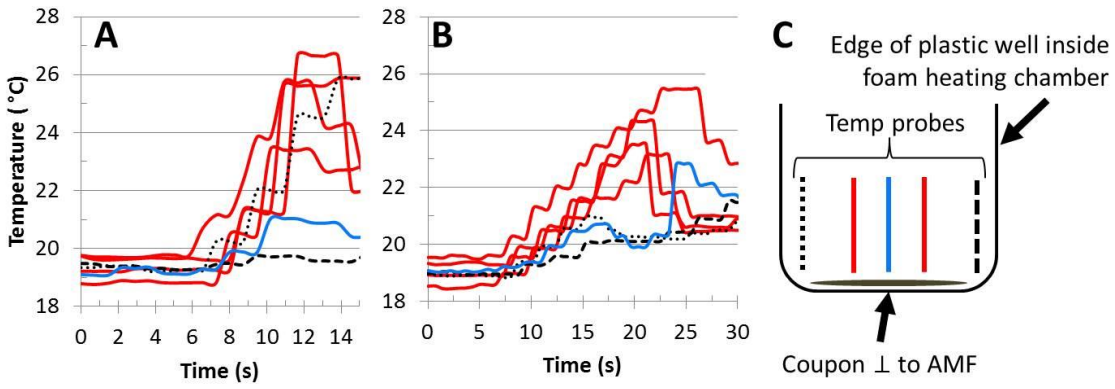

Figure 2.8. Initial temperature rise across composite surface as measured from 7 fiber optic temperature probes placed directly on the surface of a 14 mm magnetite composite coupon in water oriented perpendicular to the AMF for a 193 ± 19 µm-thick, 27wt% Fe, PS composite (A) and a 68 ± 3 µm-thick, 27wt% Fe, PS composite (B); AMF turned on at t = 5 s; C) schematic of temperature probe placement relative to AMF with colors corresponding to plots in A and B. solid blue line indicates temperature probe placed in the center of the coupon; red lines indicate 4 temperature probes placed 3.3 mm equidistant from the center probe; dashed and dotted black lines indicate temperature probes placed at the perimeter of the coupon/next to sample chamber edge.

2.6.2 Swelling

For PVA, the SAR of a hydrogel coating scales with its swelling factor in the perpendicular orientation. PS composites yield similar SAR values whether immersed in water or dodecane. As both solvents have comparatively little magnetic susceptibility and heat transfer/loss issues appear to be negligible, the lack of a solvent effect for the PS samples is not surprising. The SAR value of PVA composites doubles, however (factor of 1.96 ± 0.68) when measured in water instead of dodecane in a perpendicular orientation. While PS does not swell in either dodecane or water, the PVA will swell to 62% of its dry weight in water, decreasing the iron concentration by a factor of 1.6-1.7 depending on the iron loading. This alters the SAR by changing the amount of magnetic material between a given MNP and the AMF source as discussed above. For PVA coatings in a parallel orientation, however, swelling has no significant effect. Here, the amount of magnetic material between an individual particle and the coil is effectively the same in either state due to the films' thinness (40 – 110 μm).

2.6.3 Polymer type

The composite's polymer type influences SAR even in the absence of swelling, and despite the fact that the matrices have no significant magnetic susceptibility of their own. PVA composites heated 1.27 ± 0.24 times more than the PS composites across all solvent/orientation combinations except in dodecane in the perpendicular orientation for reasons discussed above. This is believed to be due to differences in MNP dispersion in different polymer matrices rather than polymer/particle interactions during heating. In the parallel orientation where the shielding effects discussed above are minimal, PVA composites outperformed PS composites by roughly the same factor whether they were

swollen in water (1.3 ± 0.22) or not swollen in dodecane (1.4 ± 0.18) though the mechanical moduli, and presumably the particle adhesion, of the PVA changes drastically in those circumstances. At such high loadings, MNPs consistently formed 1 – 2 μm aggregates in both polymers as seen in the SEM images of Figure 2.3; additional SEM images of PS composite showing the entire span of the film are shown in Figure 2.9. The most apparent difference between the two polymer composites is their structure where PS composites exhibited an open, porous network while MNP aggregates in PVA composites were distributed in a more continuous phase of polymer. Acid digestion of the PS composites revealed the polymer structure is retained in the absence of magnetite (Figure 2.3C).

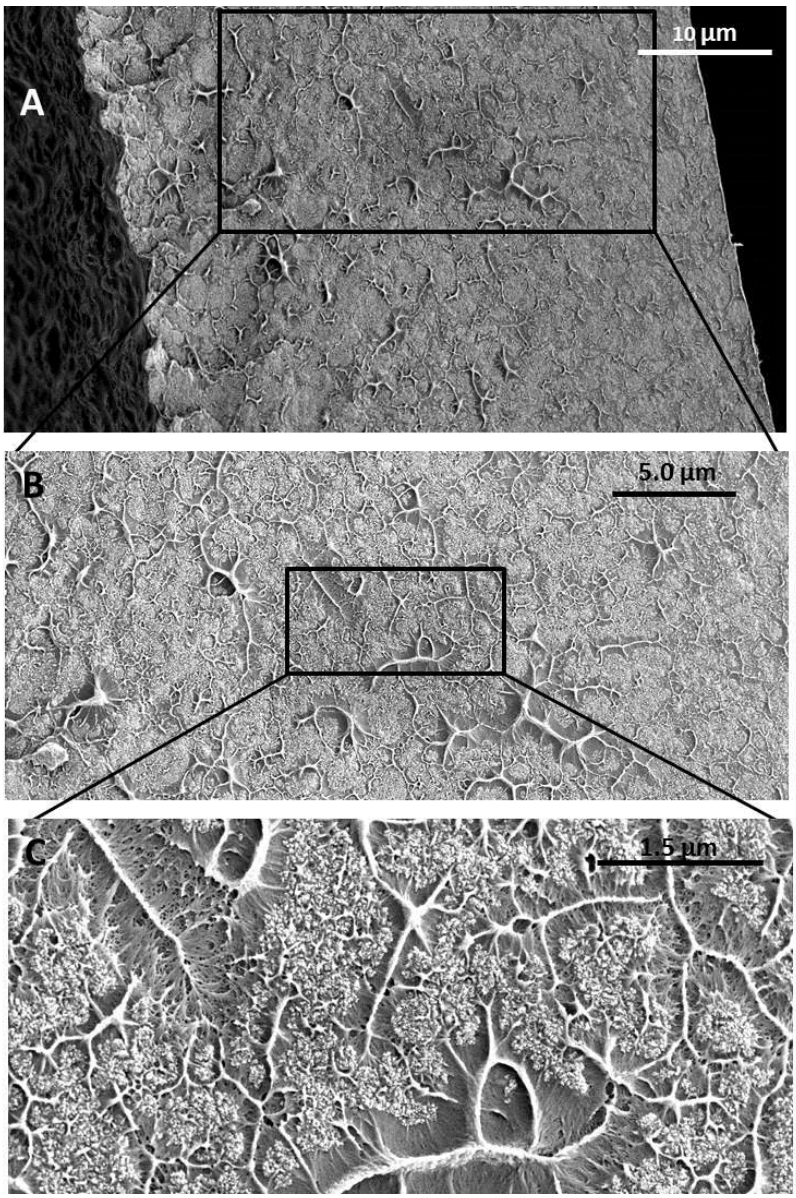

Figure 2.9. SEM images of PS composite for a 26.1 %Fe, 193 ± 19 µm-thick PS composite at three magnifications. Shown in (C) are evenly dispersed aggregates of iron oxide nanoparticles; at lower magnifaction this dispersion is retained in (B) and across the entire film thickness as shown in (A).

2.6.4 Iron loading

The performance of a given polymer will change with advances in MNP dispersion techniques at high loading and in hydrophobic media. The practical implication of this result is not necessarily that improved MNP dispersion techniques are needed, however, as SAR values did not strongly change with iron loading across all solvents, polymers, and orientations investigated. When designing a coating for magnetic

hyperthermia, this means that increasing the desired power density can be achieved simply by scaling up the magnetite loading proportionally, either through increased iron concentration or increased film thickness. However, based on the results discussed previously, one would expect SAR to be independent of the iron weight percent in the parallel orientation and decrease with iron weight percent in the perpendicular orientation. Both effects may exist experimentally (-0.38 ± 0.12 W g^{-1} $\%Fe^{-1}$ in the perpendicular orientation but $+0.03 \pm 0.26$ W g^{-1} $\%Fe^{-1}$ in the parallel orientation) but are too small to be significant across the range of iron concentrations investigated here as shown in Figure 2.10. Similarly in Figure 2.11, one might perceive an increase in SAR for increasing thickness, (0.35 ± 0.19 W g^{-1} μm^{-1} for PS) but again this trend is not significant across the factor of three thickness variation investigated.

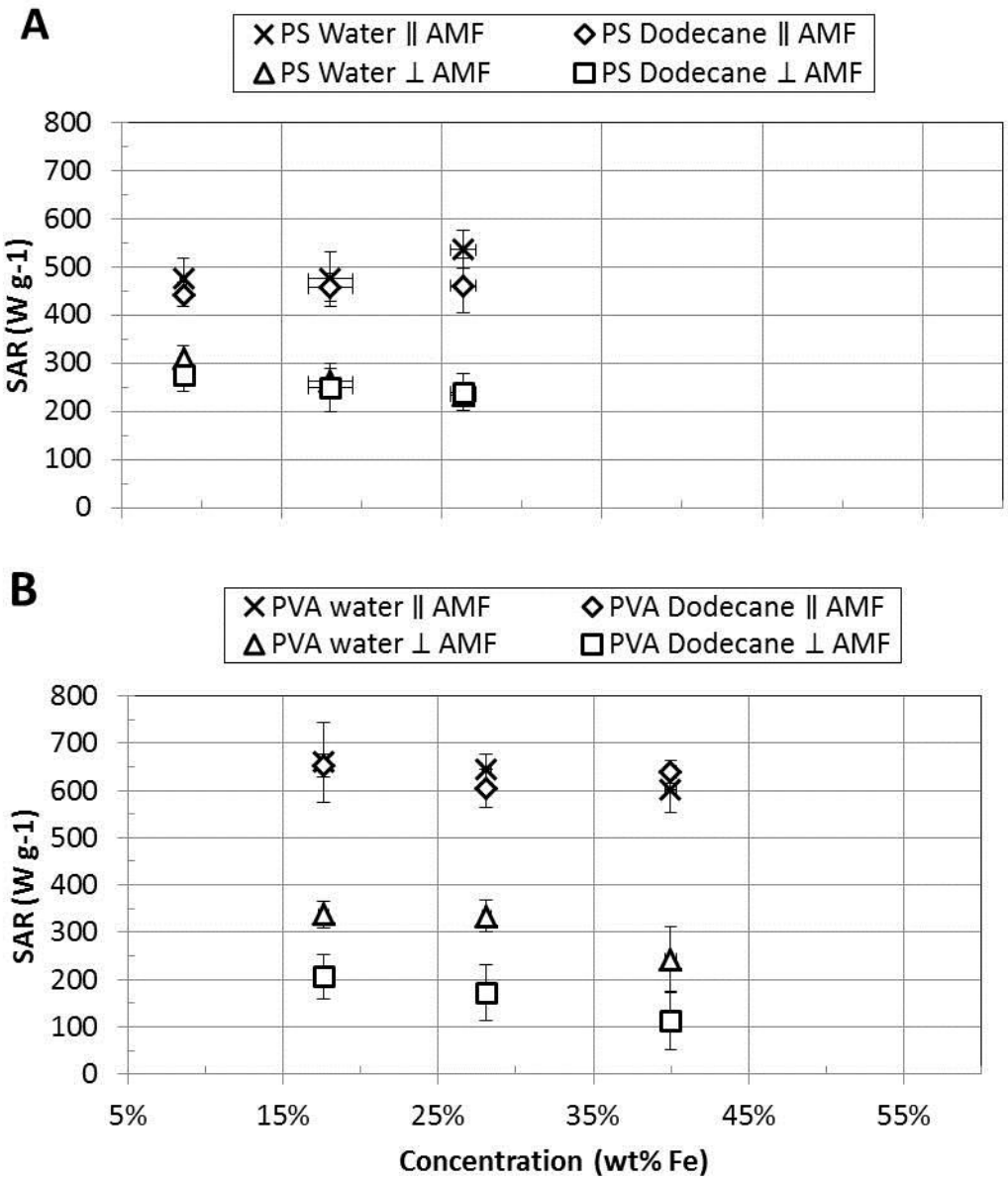

Figure 2.10. SAR versus iron concentration for PS (A) and PVA (B) composites; n = 9 for concentration and SAR, 3 thicknesses per concentration, 3 samples per thickness.

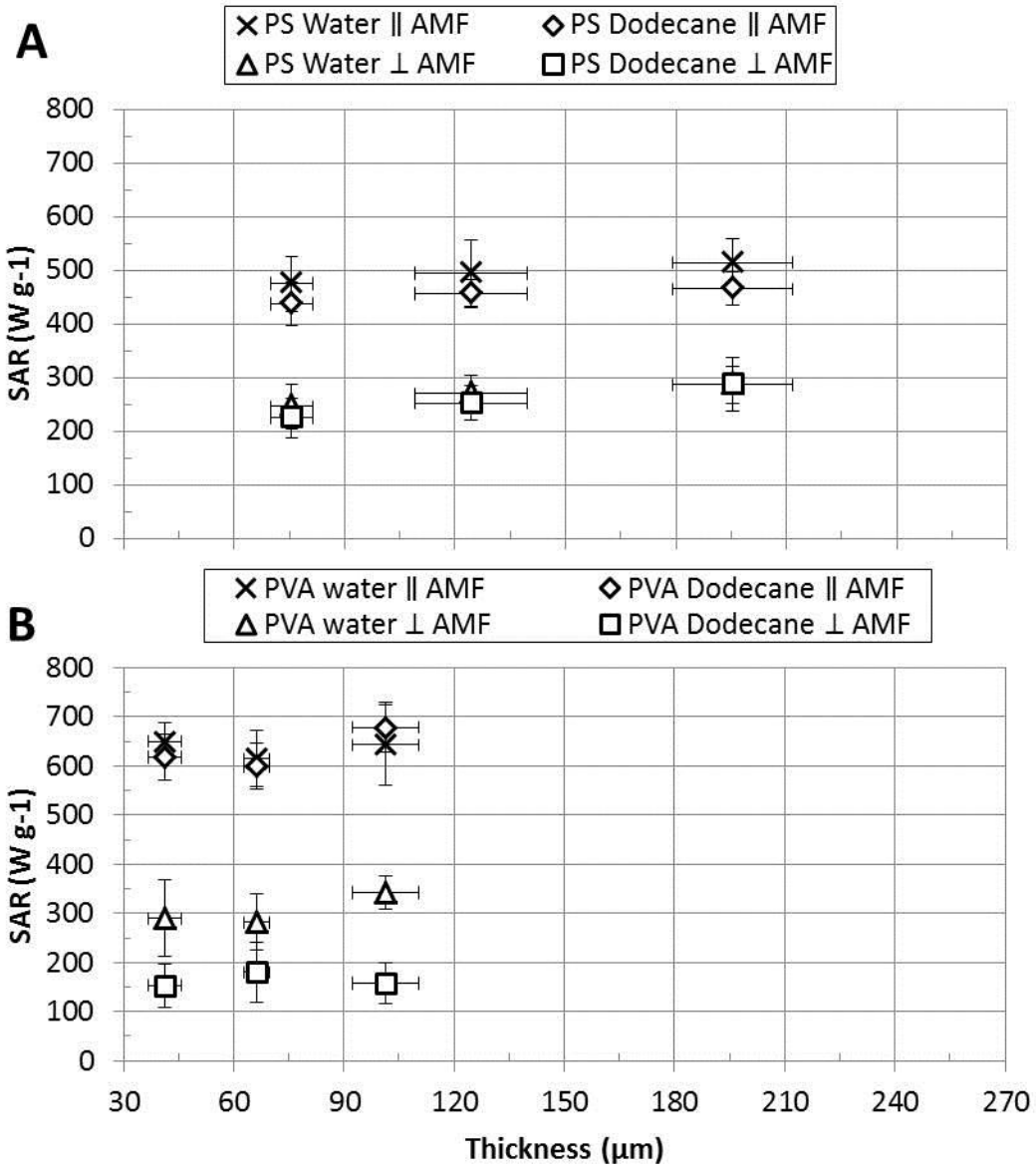

Figure 2.11. SAR versus film thickness for PS (A) and PVA (B) composites; *n* = 9 for thickness and SAR, 3 concentrations per thickness, 3 samples per concentration.

2.7 Composite longevity

The thickest PS and PVA composites were measured twice for their SAR across all iron concentrations, once at the beginning of this study in November of 2014 (the data reported in Table 2.1) and again 18 months later in May of 2016; the composites were stored at atmospheric conditions during the time between measurements. The data for both tests are shown in Figure 2.12 which shows a factor of 1.6 decrease in SAR for the

PS composites and no decrease in SAR for the PVA composites. Magnetite in the PS composites is believed to undergo oxidation to maghemite due to the increased transport of oxygen through the membrane—a result of the open, porous-like structure observed in these films from the SEM images of Figures 2.3 and 2.9. In contrast, the PVA films did not exhibit any open structure in the dry, polymer matrix. Increased nanoparticle dispersion throughout the PVA film likely results in better oxygen barrier between the nanoparticles and the environment. Further, PVA is known to be an excellent gas-barrier with an oxygen permeability on the order of 0.35×10^{-13} (cm^3 cm) × (cm^{-2} s^{-1} kPa^{-1}) at a relative humidity below 60%.[80] Although this result is surprising, distribution of the nanoparticles in the PS composites can be enhanced with improved dispersion techniques which would limit oxygen transport and improve the shelf life of these hydrophobic coatings.

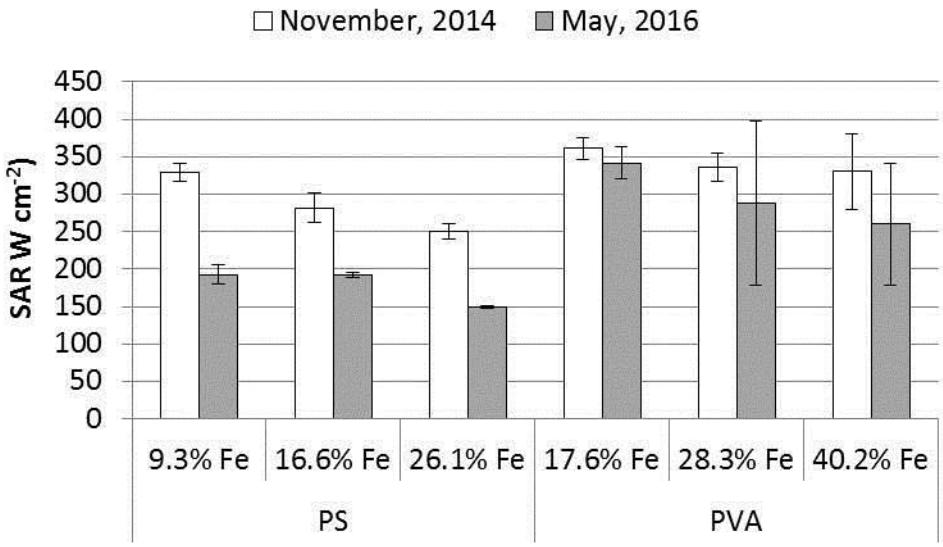

Figure 2.12. SAR Longevity study. The thickest films whose SAR was reported in Figure 2.7 was measured again 18 months later. The PS films' SAR decreased over this period whereas the PVA films' did not, suggesting the magnetite in the PS had oxidized and that PVA acts as a better encapsulating oxygen barrier than PS.

2.8 Power density

These results indicate that the heating power density of a composite coating can be scaled-up linearly by increasing the iron loading in the coating. Figure 2.13 plots the power loading (in W per cm^2) from the composites' measured SAR in Figure 2.7 assuming a weighted composite density based on the amount of iron and polymer in the composite.

Power requirements (as predicted in Chapters 4 and 5) to reach an 80 °C surface temperature beneath a hydrogel tissue mimic are also plotted against these composites' power delivery potential. The highest iron-loaded PS and PVA composites are able to supply the maximum power demanded by the 80 °C conduction-only scenario which is measured in Chapter 4.7. In the human body, higher power requirements may be necessary for a more extreme heat sink (*e.g.*, a convection-driven scenario due to blood flow) which can be provided by thicker (greater than 211 μm) films and iron concentrations above 40 wt%.

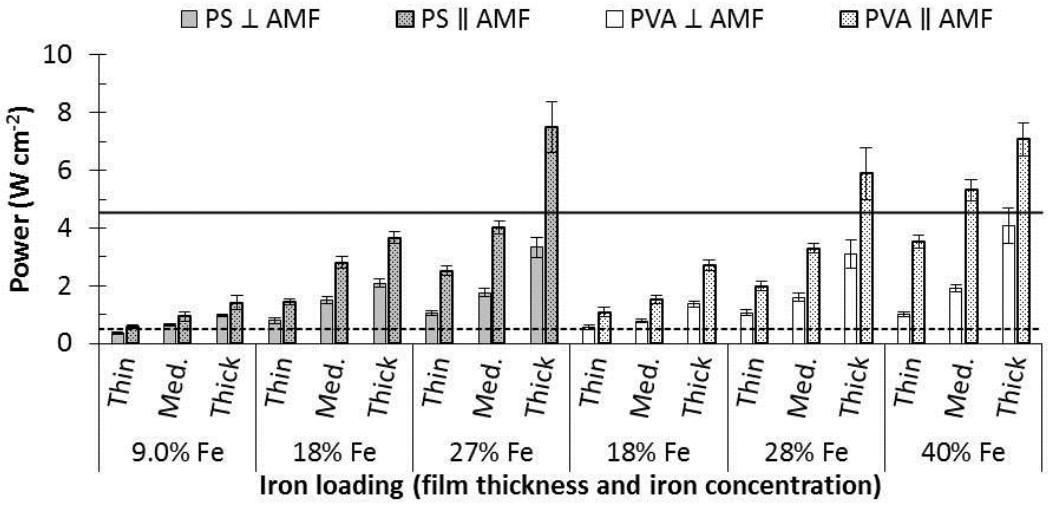

Figure 2.13. Power output from composites in water positioned perpendicular and parallel to the AMF; solid, horizontal line indicates peak power requirement for an 80 °C surface temperature subject to a hydrogel, tissue mimic heat sink; dashed, horizontal line indicates steady-state power requirement for the same scenario after 5 min of heating.

2.9 Conclusions

The composite coatings produced here exhibit power output that increases proportionally with increasing iron loading. Despite this, the SAR—regardless of polymer type and iron loading—will increase by a factor of two when the coatings are positioned parallel to magnetic field lines versus their perpendicular orientation. This result is believed to be due to magnetic shielding of neighboring particles. This hypothesis is supported by the observation that swollen PVA films will heat more than non-swollen films in the perpendicular orientation by a factor which is proportional to the decrease in concentration due to the hydrogel's swelling ratio in water. In other words, hydrogel swelling moves particle aggregates further apart which decreases magnetic shielding which increases SAR. Lastly, PVA composites exhibit higher SAR than PS composites which is likely due to particle dispersion differences in the two polymers and not due to differing magnetic interactions between the two polymers. Coatings with higher iron loadings are fabricated in Chapter 3 which can provide larger power loadings to heat bacteria up to 80 °C grown on the coating's surface.

CHAPTER 3: DEACTIVATING BIOFILMS GROWN ON REMOTELY HEATED MAGNETIC COATINGS[2]

In Chapter 2, it was shown that magnetic composite coatings can be fabricated to remotely heat surfaces with power loads exceeding 7.5 W cm^{-2}. These composite materials transform magnetic field energy to thermal energy with conversion efficiencies optimized for coatings positioned parallel to magnetic field lines. In this chapter, hydrophobic coatings that are 8.5 times larger in surface area and with 24% more iron per unit surface area are wirelessly heated in the same 50 mm solenoid. In Section 3.4, it is shown that these coatings can supply sufficient power loadings to target deactivation temperatures that kill bacteria grown directly on the composite's surface. Due to the composite's larger surface area, however, parts of the coating extend into regions of the generated AMF that exhibit lower field strengths, resulting in non-uniform surface heating. Reducing the size of coating's surface area to accommodate a more uniform magnetic field demonstrates the material's use as a wireless source for thermally treating biofilms up to 80 °C that do not rely on any chemical means to disrupt the living bacteria.

The objective of the work in this chapter is to demonstrate comparable bacteria death using a wireless heat shock method as was achieved by the water bath heat shock method used by O'Toole *et al.* in Chapter 1.2.2. The following work will demonstrate use of a magnetite, polystyrene coating designed with a large enough SAR to reach the targeted temperature in seconds. This was done for temperatures ranging from 37 to 80 °C and sustained for times ranging from 1 to 30 min. Biofilms were cultured directly on the composite coating and placed inside a magnetic induction coil integrated with

[2] This work was filed as part of a provisional patent. No. 62/355.100. Magnetically-Activated Coating for Treating Biofilms, and Associated Systems and Methods.

feedback control heating based on temperature measurements obtained directly at the composite surface.

3.1 Magnetite/polystyrene coatings for bacterial culture

3.1.1 Coating synthesis and characteristics

Fe_3O_4 nanoparticles were synthesized via a coprecipitation reaction with $FeCl_3 \cdot H_2O$ and $FeCl_2 \cdot 4H_2O$ (Sigma Aldrich) in a 2:1 mol ratio under basic conditions (KOH, Sigma Aldrich) using the same methods presented in Chapter 2.1. Composite coatings were prepared by dissolving 3.2 g of polystyrene (PS) resin (~280,000 MW, Sigma Aldrich) in approximately 40 g of rinsed iron oxide nanoparticle slurry (0.082 g Fe_3O_4 per g of slurry in toluene) and cast on frosted glass microscope slides in 1 mm wet layers, three times, to produce dry coatings that were 226 ± 6 µm thick. PVA composites were not used for these biofilm heat shock experiments due to unwanted delamination of the PVA from the microscope slide as a result of the swelling pressure induced once the film began to hydrate. After casting, films were dried at ambient conditions for 8 hr followed by 12 hr of drying at 90 °C to evaporate all remaining solvent. Coatings were remotely heated in the same 6-turn AMF generating coil used in Chapter 2 operating at up to 2.32 kA m^{-1} and 302 kHz. The coating's parameters, including SAR, are summarized in Table 3.1. SAR was measured using 12 mm coupons and the same methods/calculations developed in Chapter 2.5.

Table 3.1. Magnetic composite coating properties used for biofilm culture.

Iron concentration (wt% Fe)	30.3 ± 1.03
Film thickness (µm)	226 ± 6
SAR ∥ AMF at max. power (W g^{-1})	675 ± 26
SAR ⊥ AMF at max. power (W g^{-1})	194 ± 5

3.1.2 Biofilm culture

Pseudomonas aeruginosa PAO1 (15692, American Type Culture Collection) biofilms were grown on the magnetite/polystyrene coated glass microscope slides prepared in Section 3.1.1, totaling 9.38 cm^2 in surface area coverage. *P. aeruginosa* biofilms were cultured in 5.0 mL of 30 g L^{-1} tryptic soy broth media (TSB, BD Bacto) with an additional 3.33 µL of 2.12 ± 0.07 x 10^9 CFU mL^{-1} inoculum for 96 hr at 37 °C on an orbital shaker (VWR) operating at 160 rpm.

Heat shock experiments were conducted in triplicates at exposure times of 1, 5, and 30 mins and temperatures of 37, 50, 60, 70, and 80 °C for a total of 45 heat shock experiments. Biofilms were grown on freshly prepared coatings for each trial; coatings were not reused from trial to trial. Details of the implementation of the wireless heat shock are described in Section 3.2.

After heat shock, the quantity of viable bacteria remaining was enumerated via serial dilution. Heat shocked biofilms/microscope slides were sonicated (VWR Symphony 9.5 L sonicator) in 5 mL of fresh, sterile DI water for 10 min. This solution was serially diluted tenfold, seven times; each dilution was spot plated in 20 µL droplets on agar plates. Plates were incubated at 37 °C for 20 to 24 hr before counting the colony forming units (CFUs). Final bacteria populations were reported as log(CFU cm^{-2} + 1) values using Equation 3.2:

Equation 3.2

$$\log(x) = \log\left[\frac{\left(\frac{5\ mL}{0.02\ mL}\right)(plate\ count)x10^{dilution\ factor}}{9.38\ \frac{cm^2}{slide}}\right]$$

One CFU cm^{-2} was added to each count to avoid mathematically undefined colony counts (*i.e.* log(1) is equivalent to zero CFUs). The reported plate count was determined from the dilution that grew CFUs in the range of 3 to 63 CFUs. Plate counts at or below 3 CFUs (equivalent to 1.90 CFU cm^{-2} using Equation 3.2) were inconclusive and within the error of one viable CFU. Thus, the quantification limit for viable CFUs was considered to be 1.90 CFU cm^{-2}.

3.2 Heat shock method and AMF field strength distribution

Biofilms grown on magnetite/polystyrene composite coatings were heated and submerged in 3 mL of sterile, degassed DI water, situated in a 3D-printed (Fortus 400mc, Stratasys) plastic heating chamber shown in Figures 3.1A and 3.1B. This circular chamber was designed to fit within the 50 mm AMF coil with 6.4 mm of foam insulation placed between it and the coil as shown in Figure 3.1C.

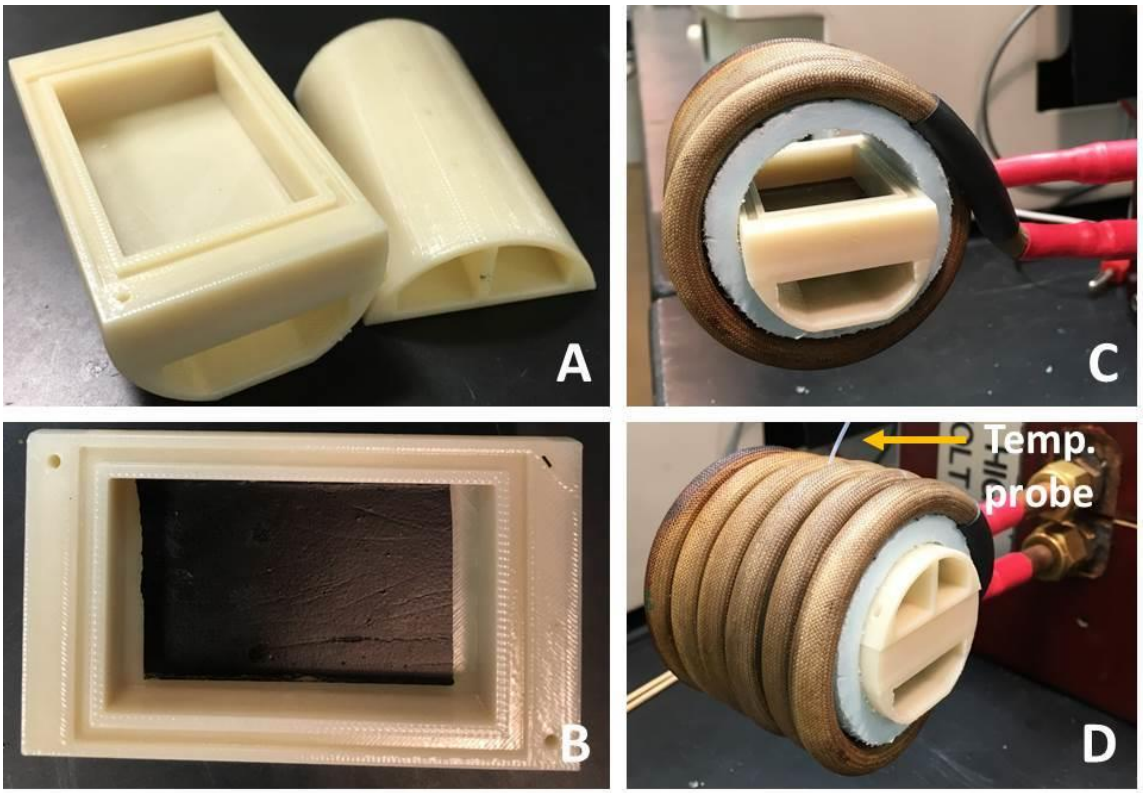

Figure 3.1. Chamber used for wireless heat shock. A) Circular chamber base and lid with hollow voids to insulate chamber from heat loss and B) with coating in chamber base. C) Chamber placed in 50 mm AMF coil with insulating foam between the coil and chamber. D) Chamber fully assembled in coil with fiber optic temperature probe passed through coil rungs and into the chamber.

The positioning of the composite coating/biofilm in the coil was determined based on AMF strength measurements shown in Figure 3.2 which plots the AMF strength (kA m) in the same plane as the coating as interpolated from measurements obtained in Chapter 2.4. Figure 3.2 shows a roughly uniform field strength except, perhaps, in the upper left corner which is likely due to the asymmetrical nature of the wrapping of the copper coil used to make the solenoid.

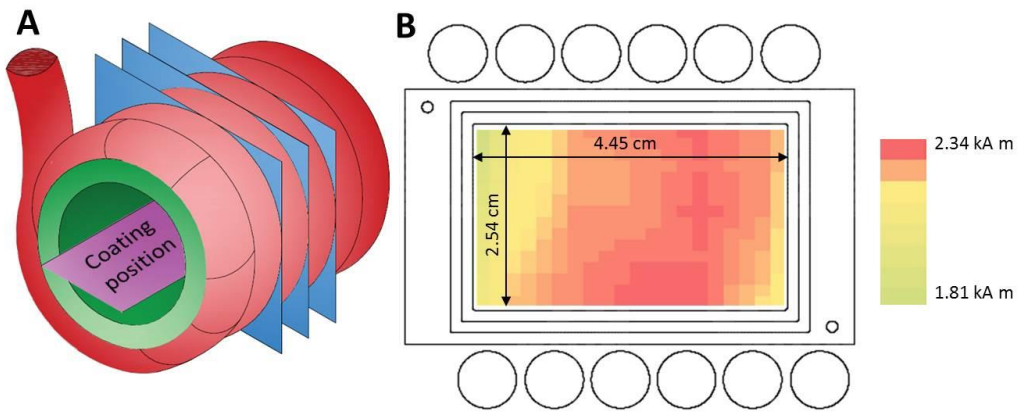

Figure 3.2. Alternating magnetic field mapping. A) Schematic of AMF coil indicating position of coating relative to the coil (purple plane). B) AMF intensity measurements at this plane within the coil indicating uniform AMF throughout the chamber except near the left side of the chamber.

Temperature feedback control (operated by an Omega.com iSeries temperature controller) was implemented using a fiber optic temperature probe (Opsens) placed directly on the coating's surface. This probe was threaded through the center-most rungs in the AMF coil and through a small hole in the lid of the heating chamber which was positioned directly over the center of the coating/microscope slide as shown in Figure 3.1D. The power delivered by the AMF coil (and thus power inducted by the magnetic coating) was manipulated in response to the temperature measured by this fiber optic temperature probe. Controller tuning parameters were adjusted to minimize both the time required to reach the specified surface temperature setpoint and the amount of overshoot from the setpoint.

3.3 Wireless heating performance of the magnetite coating

3.3.1 SAR versus AMF field strength

As shown in Figure 3.1, the orientation of the coating was positioned parallel to magnetic field lines in order to optimize the power generated by the incorporated magnetite nanoparticles. The SAR for this orientation was 675 ± 26 W g^{-1} compared to

194 ± 5 W g^{-1} in the perpendicular position. The SAR of the composite coating in the parallel position was measured as a function of AMF field strength (reported as a percent of maximum power) and was converted to W cm^{-2} as shown in Figure 3.3.

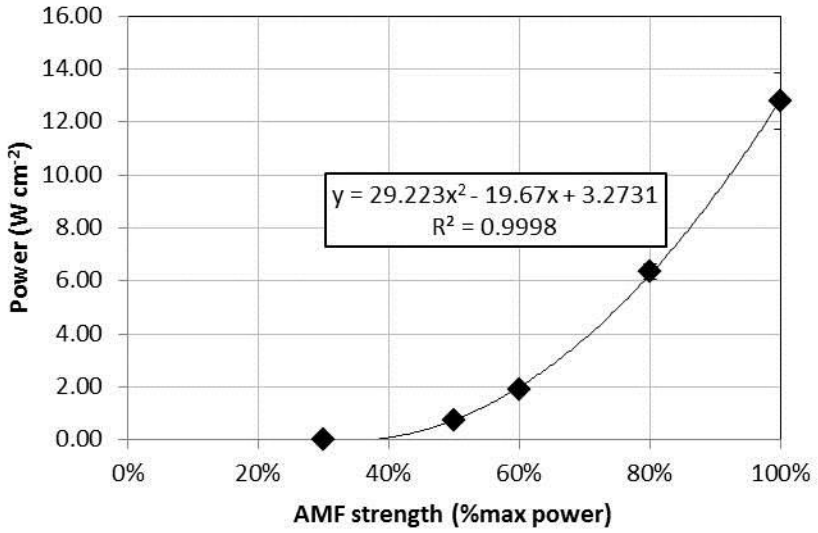

Figure 3.3. Power output from magnetic coating as a function of the power delivered to the AMF coil. The power delivered from the magnetic coating is quadratic with AMF strength. Power delivery is near zero at 30% AMF strength which indicates a scaling or offset issue with the field generator controller but does not impact the power delivery efficiency of the coating.

A typical transient profile of the power delivered by the composite coating during an 80 °C heat shock is shown in Figure 3.4. An initial, maximum power of 12.8 W cm^{-2} is delivered to bring the surface temperature up to its 80 °C setpoint. Once the temperature approaches this setpoint, the controller reduces the power delivery dramatically and reaches a steady state value near zero after 12 min of heating, suggesting minimal heat losses from the heating chamber to the environment.

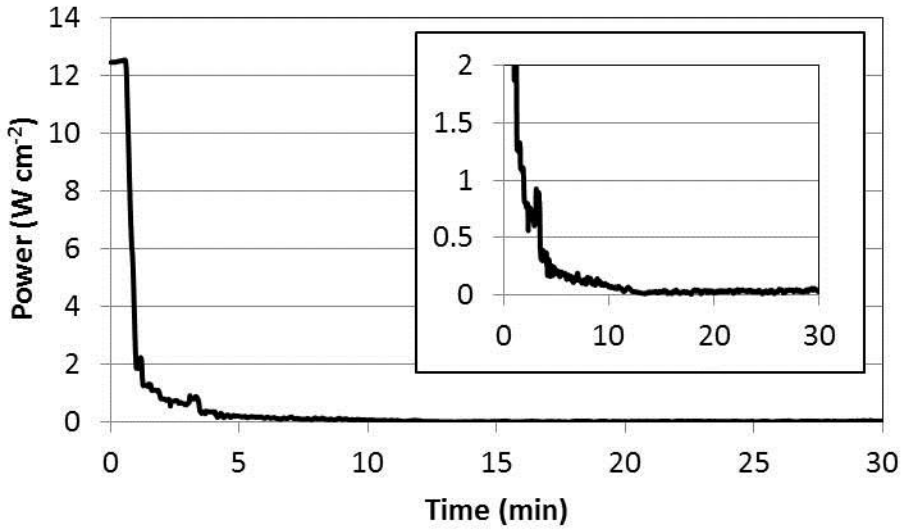

Figure 3.4. Transient power delivery from magnetic coating during a typical heat shock trial for an 80 °C surface setpoint. At early times, the power output from the coating is at a maximum. As the coating nears its setpoint temperature, the power output decreases exponentially to maintain the 80 °C setpoint with minimal overshoot and offset. Steady state output is achieved after 12 min with near zero power delivery, indicating minimal heat loss to the environment.

3.3.2 Transient temperature profiles

Typical transient temperature profiles for the coating under feedback control are shown in Figure 3.5. The most extreme temperature rise (from 21 to 80 °C) was achieved in approximately 30 to 45 s with lower setpoints reaching their target temperature more quickly.

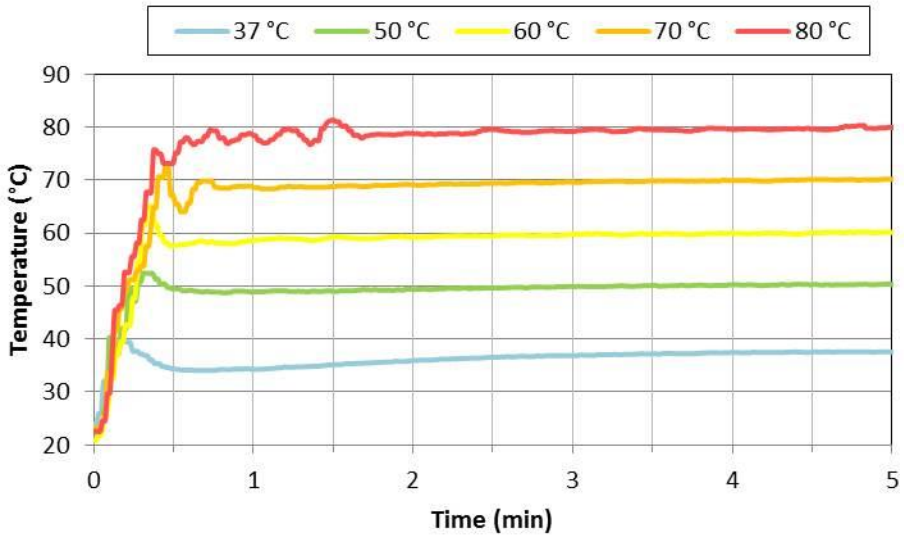

Figure 3.5. Transient temperature profiles of coating surface. Setpoint surface temperatures were achieved in less than 45 s from the time the AMF generator was turned on to begin the heat shock. Less than 0.5 °C offset is observed once steady state is achieved.

The amount of time the coating was not at its setpoint was quantified by dividing the area underneath the temperature curve by the ideal area that would be obtained if the coating reached its setpoint instantaneously at $t > 0$. Further, the offset (defined as the difference the actual temperature deviated from its setpoint value) was quantified by time averaging this value over the entire trial period. These two numbers are summarized in Table 3.2 for all time/temperature combinations and provide a measure for how well the heat shock was maintained at its specified time and temperature. The amount of time the coating was not at its setpoint value for the 1 and 5 min heat shocks is higher due to the span of time required to reach its target temperature. Negative offset values for these trials were more desirable over positive values which indicate longer periods of temperature overshoot during the initial temperature climb. Consequently, the percent of time away from the setpoint and amount of offset was negligible for the longer, 30 min trials.

Table 3.2. Integrated temperature profiles and time averaged offset values from heat shock trials.

Setpoint (°C)	Time (min)	T(t)/ Setpoint(t)	Offset (°C)
37	1	0.89 ±0.17	-1.4 ±1.9
37	5	0.93 ±0.06	-0.7 ±0.7
37	30	0.99 ±0.01	0.2 ±0.0
50	1	0.89 ±0.02	-2.6 ±0.6
50	5	0.96 ±0.02	-0.8 ±0.1
50	30	0.96 ±0.08	0.1 ±0.1
60	1	0.81 ±0.01	-6.1 ±0.8
60	5	0.96 ±0.01	-1.3 ±0.4
60	30	0.99 ±0.00	0.0 ±0.1
70	1	0.78 ±0.06	-10.1 ±2.4
70	5	0.93 ±0.00	-2.4 ±0.2
70	30	0.98 ±0.01	-0.2 ±0.1
80	1	0.71 ±0.05	-15.1 ±2.2
80	5	0.93 ±0.02	-3.6 ±0.6
80	30	0.99 ±0.01	-0.5 ±0.1

3.3.3 Steady state temperature map

Five temperature probes were positioned directly on the coating's surface, along the center axis that was parallel to magnetic field lines; *e.g.*, these probes measured temperature differences down the center of the coating along the 4.45 cm span shown in the AMF map of Figure 3.2. These temperature differences are attributed to variation in the magnetic field strength generated by the AMF coil. Steady state values for all five probes at various temperature setpoint values are shown in Figure 3.6.

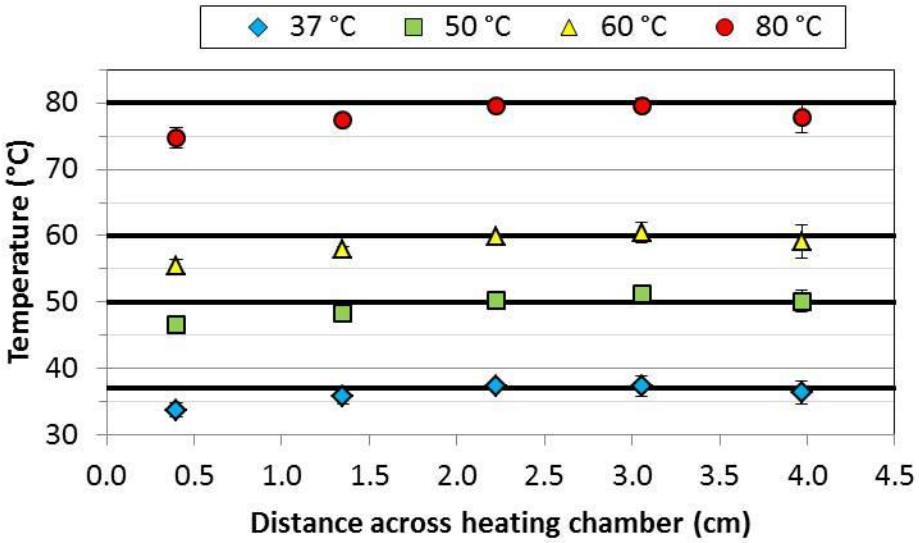

Figure 3.6. Temperature measurements across coating surface correspond to deficiencies in the magnetic field strength near the left end of the coil/heating chamber which result in parts of the coating being heated to lower temperatures than the desired setpoint value.

Significant cold spots are observed on the left side of the coating which correspond to areas within the AMF coil that produce a weaker field as shown in the AMF map of Figure 3.4. The portion of the coating that was nearest the left side of the heating chamber/coil experienced a diminished AMF intensity that resulted in as much as a 5 °C temperature drop from the rest of the coating in the heating chamber. This means that a 60 °C setpoint specified at the center of the coating would also produce areas on the coating that were 55 – 56 °C. Thus, biofilm bacteria in these cooler areas would not experience the same thermal shock as bacteria on the rest of the coating. This temperature gradient, however, was not measured until after an initial set of heat shock trials was performed for all times and temperatures and is discussed next in Section 3.4.

3.4 Biofilm deactivation

3.4.1 Initial cell counts

The amount of viable bacteria remaining after wireless heat shock is quantified in Figure 3.7 for biofilms grown on 3.8 cm-long coatings (9.4 cm^2 surface area) and demonstrate an acceptable trend in decreasing live bacteria for increasing heat shock times and temperatures. The degree of cell viability after the controlled heat shocks at 37 °C is the same for all time durations. Despite the presence of the iron oxide composite coating, the colony counts for these controls match those of biofilms grown on plain, frosted glass microscope slides using the same growth protocol and media.[27]

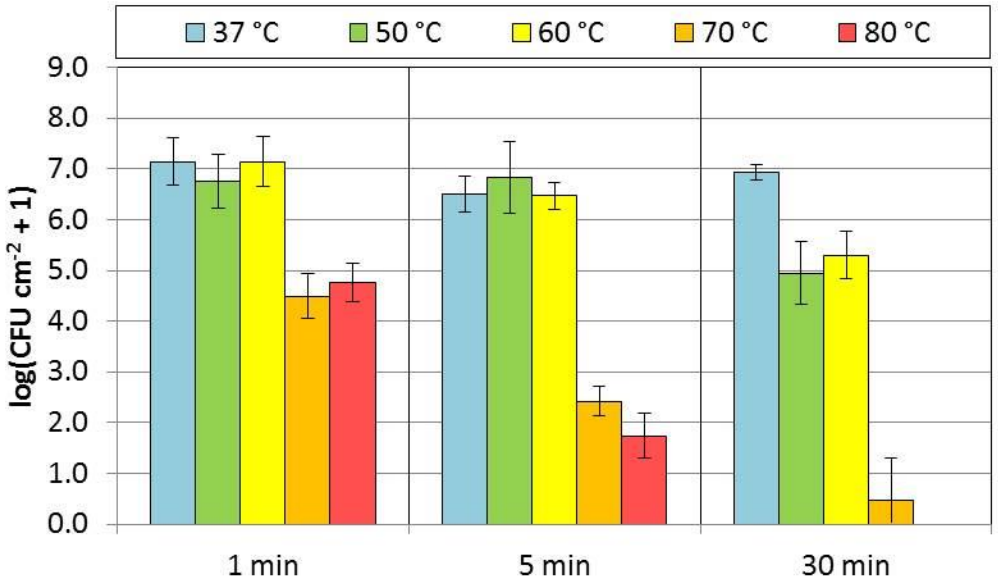

Figure 3.7. Cell death for bacteria grown on 9.4 cm^2 surface area coating. Wireless heat shocked biofilms demonstrate less than an order of magnitude reduction in viable bacteria for all 50 °C trials and 60 °C trials at times less than 30 min.

There are, however, some discrepancies between the data reported for these wireless heat shocks and a similar study that used a temperature controlled water bath to perform the heat shock for the same times and temperatures.[81] That study was performed concurrently by Ricker *et al.* in the same lab as the wireless heat shock data reported

here. In both studies, biofilms were grown using a shaker plate method which produces biofilms roughly two order of magnitude less dense than the drip flow reactor biofilms introduced in the heat shock study in Section 1.2.2 and presented in Figure 1.2. Ricker *et al.* point out that these less dense shaker plate biofilms colonize with fewer bacteria due to added stresses as a result of the growth protocol which includes increased shear, lack of waste removal, and lack of nutrient replenishment. As a result, these shaker plate biofilms are hypothesized to be more resistant and less susceptible to the environmental stress of the subsequent heat shock.

When subjected to a 50 °C heat shock, the shaker-plate-grown biofilms in the water bath heat shock study did not show any significant cell death greater than one order of magnitude from the controls, irrespective of time as shown in Figure 3.8.

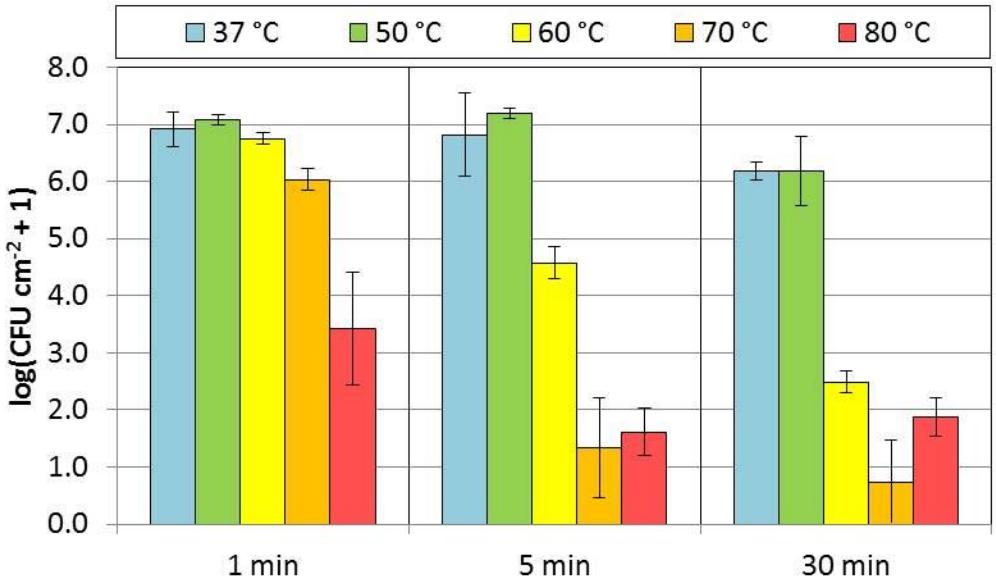

Figure 3.8. Cell death after water bath heat shock. Data reproduced from Ref. 81. These water bath heat shocked biofilms show larger amounts of cell death for the 60 °C trials compared to the wireless heat shocked biofilms in Figure 3.9. The 50 °C heat shocked biofilms are the same for both methods.

Even at 60 °C for 1 min, the amount of viable bacteria remaining after heat shock was nearly the same compared to the controls. Higher thermal loads (*i.e.* 60 °C at times

greater than 1 min and temperatures greater than 60 °C for all times) demonstrate a more measurable effect at heat treating bacteria in biofilms. At 80 °C for times greater than 1 min, the amount of viable bacteria after the heat shock falls below the minimum detection limit for the enumeration assay used to quantify CFUs. Since the biofilms grown for the wireless heat shock study reported here were incubated under identical conditions (except for the presence of the coating), the amount of cell death should follow these same trends as reported by Ricker *et al*., given the wireless heat shock is implemented as effectively as the water bath heat shocks.

Analyzing the wireless heat shock data in Figure 3.7, the 50 °C heat shocks all demonstrate cell counts that are in line with the water bath heat shock data reported in Figure 3.8. Increasing the thermal load by 10 °C to 60 °C, the wireless heat shocks at 5 and 30 min did not appear to kill the bacteria as effectively as the water bath heat shocks. Moreover, the amount of viable bacteria remaining after the 80 ° wireless heat shock at 1 min is unusually high.

When considering differences between the two types of heat shock modalities (water bath vs. wireless) the most obvious difference can be seen in the coating's steady state temperature map in Figure 3.6. This temperature map demonstrates the wireless heat shocks are subject to non-uniform steady state temperature gradient due to variations in the field strength; whereas the biofilms heated using the water bath method reach a uniform target temperature nearly instantaneously due to the thermal inertia provided by the large, temperature controlled water bath. As much as a 5 °C temperature drop is observed on the left side of the coating, which for a 60 °C setpoint, would mean this part of the biofilm is only being heated to approximately 55 °C. From the 50 °C heat shock

trials in both water baths and AMF, it is clear that these biofilm bacteria exhibit far less thermal deactivation at these lower thermal loads. If parts of the coating were actually at 54 to 56 °C, this could explain why higher amounts of viable cells were observed in the 60 °C AMF trials than in the corresponding water bath trials.

3.4.2 Revised temperature map

In an effort to minimize the temperature gradient across the entire coating, the length of the microscope slide was reduced from 3.8 cm to 2.5 cm to fit the coating/microscope slide in a more uniform field (shown in Figure 3.2) in the center of the coil. The same volume of water (3 mL) was added to the heating chamber to impose the same depth of water, and thus heat sink, on top of the biofilm/coating. However, because of the shorter length of coating used in the same heating chamber, unheated water on either side of the coating created an unwanted heatsink at the coating's edge, which resulted in a temperature gradient across the coating's surface. To reduce the amount of heat transfer at the edge of the coating, two pieces of foam insulation were placed on either side of the coating as shown in Figure 3.9A. Temperature probes positioned at the surface of this insulated coating measured steady state temperature profiles across the entire coating surface with less than 1 °C variation from end to end as shown in Figure 3.9B.

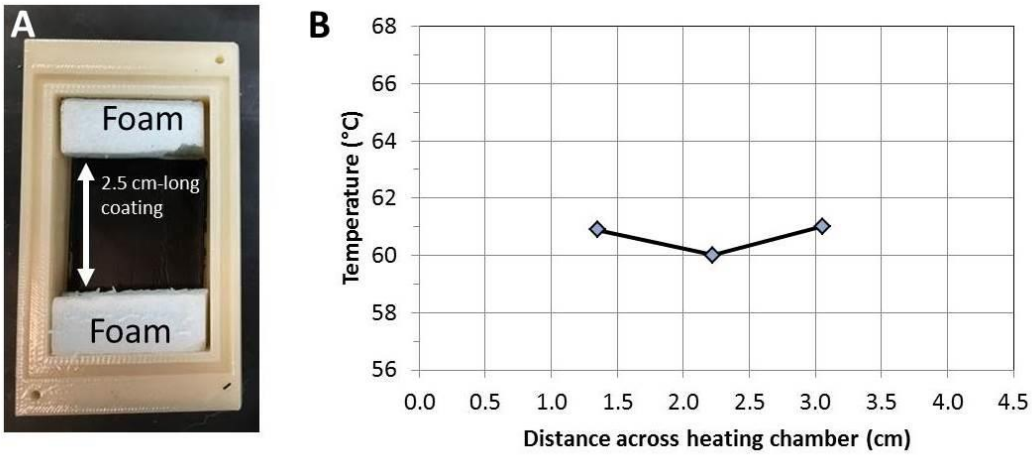

Figure 3.9. Temperature map for 6.3 cm^2 surface area coating. This coating was insulated by two pieces of foam (A) to produce a temperature field that varied < 1 °C across the entire 6.3 cm^2 surface (B).

3.4.3 Final cell counts

With a more uniform temperature gradient established, wireless heat shock trials were repeated with biofilms grown on the smaller coatings for temperatures at 60 °C at 5 and 30 min, 70 °C at 1 min, and 80 °C at 1 min; the results are shown in Figure 3.10.

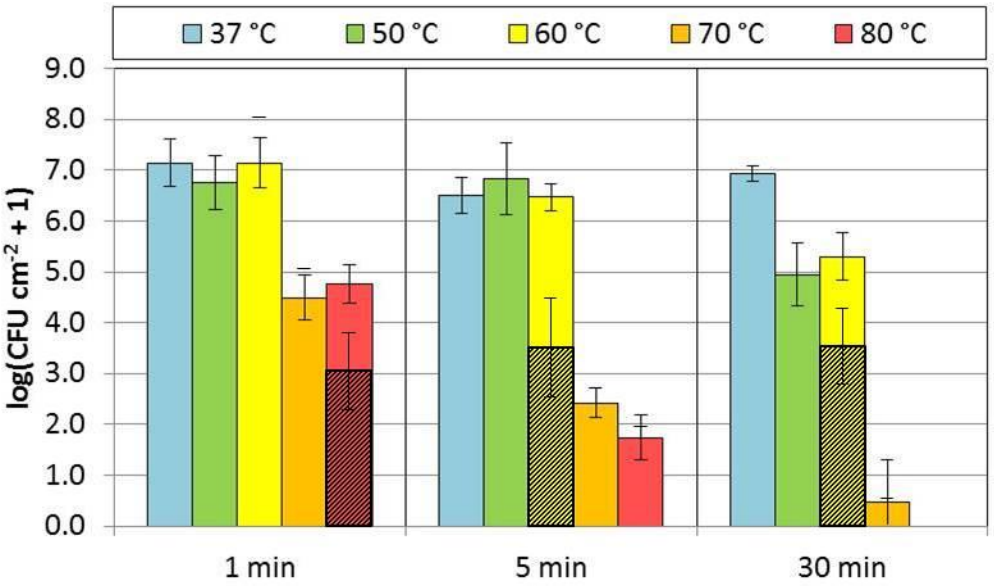

Figure 3.10. Cell death for bacteria grown on a 6.3 cm^2 coating. Revised cell death counts are overlaid on the data from Figure 3.7 as indicated by the shaded boxes for the 60 °C heat shocks at 5 and 30 min and 80 °C for 1 min. These heat shocks are in better agreement with the water bath heat shocks in Figure 3.8. The 70 °C heat shock for 1 min did not show any increase or decrease in viable bacteria for this smaller coating compared to the 9.4 cm^2 coating.

The 70 °C, 1 min heat shock did not show any statistically different cell death than the previous trial carried out on the larger coating. The repeated 60 °C trials for 5 min and 30 min demonstrated larger quantities of cell death which were in better agreement with the water bath trials in Figure 3.8. The 80 °C at 1 min heat shock also demonstrated more cell death, though, the 1 min wireless heat shock trials are arguably more difficult to directly compare to the water bath heat shocks since more than half of the wireless heat shock time is devoted to bringing the coating up to its target temperature. Despite this, the wireless heating method used here more accurately reflects how a surface would be heated inside the body as there will always be a time lag between the initial, *in situ* body temperature and the desired deactivation target temperature.

3.5 Conclusions

Combined, the water bath heat shock data set and the wireless heat shock data set suggest biofilms grown using the shaker plate method do not undergo significant cell death at times and temperatures below 60 °C for 5 min. This is not to say that the biofilm is more or less susceptible to other forms of attack (*e.g.* antibiotics or the host's immune system) when heat shocked at these lower thermal loads. At higher thermal loads, *P. aeruginosa* biofilms will experience a population reduction of three to four orders of magnitude reduction in viable bacteria when heated to 80 °C for 1 min. This is despite a 30 to 45 s time lag between when the coating is first heated and when the coating reaches its target temperature.

80 °C may seem like an extreme temperature to be heating a surface inside the body. In Chapters 4 and 5, a tissue phantom material and a predictive model are developed to begin to understand the ramifications of heating tissues and organs at these

extreme temperatures. Additionally, the coating developed in this chapter was capable of delivering up to 12.8 W cm^{-2} of power in a 302 kHz, 2.32 kA m^{-1} AMF which was adequate for the 3 mL of stagnant water heat sink used here. Some parts of the body—such as a surface next to an artery or vein—could experience much higher heat sinks due to convective forces provided by blood flow. Thus, the experimental conditions used to mimic *in vivo* heat transfer in Chapter 4 and the modeling in Chapter 5 will also be used to quantify the power loads needed by a magnetic coating for these types of heat sinks and other heat sink combinations.

CHAPTER 4: POLY(VINYL ALCOHOL) HYDROGELS AS A TISSUE PHANTOM FOR MODELING IN VITRO HYPERTHERMIA[3]

The benefits of using a hydrogel tissue phantom as a means for measuring heat transfer in a medium that mimics biological tissues were discussed in Section 1.5.1. Here, the effects of crosslinker ratio, curing temperature, curing time, and property modifiers were investigated to enable the reproducible fabrication of a poly(vinyl alcohol) (PVA) hydrogel tissue phantom with targeted swelling and thermal properties. By tuning each of these parameters, Sections 4.4 and 4.5 demonstrate the benefits of chemically crosslinked PVA over traditional tissue mimic materials and compares them with conventional poly(acrylamide) (PAA) phantoms. The key advantages of these mimics are: 1) crosslinking, and thus gel/network formation, occurs after the PVA solution has been poured (*i.e.*, cast) into its desired geometry, producing bubble-free, optically-clear phantoms which conform to complex geometries with micron-scale features; 2) the gelation rate is rapid compared to the settling rate of property-modifying fillers, allowing the fillers to be homogenously dispersed in the resulting phantom; 3) the swelling ratio can be carefully tuned to increase, decrease, or remain constant with a shelf-stability of at least 25 days in water, even under extreme conditions such as 80 °C; and 4) the phantom is a hydrogel, largely mimicking most of the chemical and physical properties of biological tissue, even before incorporating any of a wide variety of non-reactive fillers to precisely tune the phantom's thermal and mechanical properties. The ability to perform facile, highly controlled heat transfer studies using a hydrogel tissue mimic are ascribed

[3] This work was published on June 15, 2016. Coffel, J.; Nuxoll, E., Poly(vinyl alcohol) tissue phantoms as a robust in vitro model for heat transfer. *International Journal of Polymeric Materials and Polymeric Biomaterials* **2016**, 65 (15), 797-806.

to these attributes as demonstrated here via an *in vitro* model with temperature acquisition at submillimeter spatial resolution and ± 0.1 °C accuracy.

4.1 PVA phantom synthesis

Hydrogel phantoms were prepared from 8 wt% poly(vinyl alcohol) (PVA) solutions by dissolving dry PVA resin powder (99 mol% hydrolyzed, ~133,000 MW, 1.29 g cm^{-3}, Polysciences, Inc.) in deionized water at 90 °C for 10 min. Clear PVA solutions were cooled to room temperature and adjusted to a pH of 2.0 using 1 M HCl. PVA solution viscosity was measured with a falling ball viscometer (GV-2200, Thermo Fisher Scientific) at 22 °C. Glutaraldehyde (GTA) (50 wt%, Fisher Scientific) was then added in the desired crosslinking ratio (x_{CL} ≡ mol GTA/mol PVA monomer units) under vigorous stirring at either 80 °C or room temperature (22.0 ± 0.5°C) prior to pouring 110 g of the solution into a 9.5 cm-diameter crystalizing dish to produce approximately 1.5 cm-thick phantoms for swelling studies. The crosslinking ratio x_{CL} was varied from 0.0025 to 0.04 for syntheses at both 80 °C and 22 °C.

Crosslinked hydrogel phantoms prepared at 22 °C were quenched in 5 L DI water to remove the acid catalyst after a specific time duration following the addition of GTA (defined as the quenching time, t_q). The effect of quenching time was investigated with the highest crosslinker density (x_{CL} = 0.04) with t_q ranging from 50 min to 3 hr. Phantoms prepared at 80 °C were allowed to cool to room temperature for 1 hr and then stored in DI water at room temperature.

4.2 PAA phantom synthesis

PAA phantom hydrogels were polymerized from a previously published method by dissolving 8.8 g of acrylamide monomer in water in a 150:1 mol ratio with methylene *N,N'*-methylenebisacrylamide (MBA) and 295 µL of tetramethylethylenediamine accelerator to produce 100 g of monomer solution.[82] To this, 0.0762 g of ammonium persulfate (APS) dissolved in 10 g of water was mixed with the monomer solution for 30 sec at room temperature to initiate polymerization and then poured into a 9.5 cm-diameter crystalizing dish. The monomer solution gelled in approximately 5 min to produce a 110 g, 8.0 wt% PAA phantom. After 12 hr, PAA phantoms were transferred and stored in DI water at room temperature.

4.3 Phantom pourability

While many phantom materials are initially pourable, few can be poured directly into their final dimensions, particularly if the material will later be subject to higher temperatures. Temperature stability typically requires chemical crosslinking or polymerizing the hydrogel *in situ* as is the case for the PVA and PAA hydrogel phantoms, respectively. Alternatively, a hydrogel phantom can be poured into a generic monolith of arbitrary dimensions, cured into a volume-stable state, and then carved into the target dimensions after it has reached its equilibrium volume. However, this becomes difficult with complex geometries and virtually impossible for sub-millimeter features such as thermistor niches or perfusion channels.

4.3.1 Gelling time vs. crosslinking temperature

For the PVA system, the time window for pourability can be controlled by the temperature. The time required for the PVA solution to crosslink and immobilize a stir bar at 250 rpm was defined as the gelling time and demonstrated an Arrhenius temperature dependence which is shown in Figure 4.1 for 8 wt% PVA solutions for GTA concentrations of x_{CL} = 0.01. Solutions crosslinked at 22 °C required approximately 90 min to achieve a non-pourable, elastic phantom (time recorded in Figure 4.1) and approximately 120 min to achieve a more rigid state. At 80 °C, the PVA solution crosslinked to form a rigid phantom in less than 30 sec as indicated in the inset of Figure 4.1.

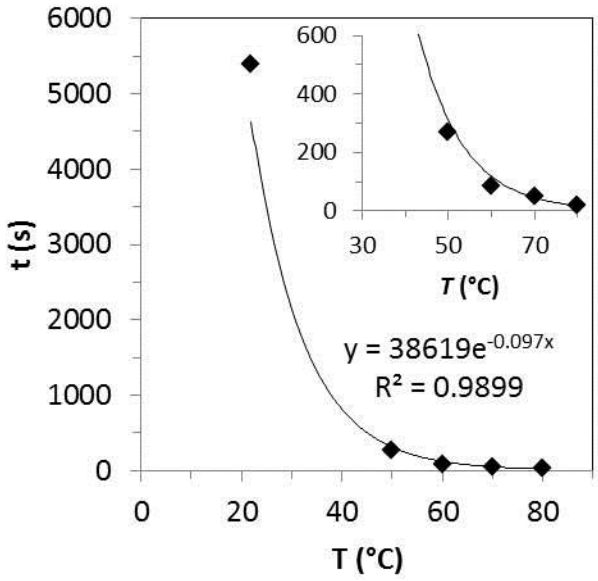

Figure 4.1. Temperature dependent curing time. PVA tissue phantom curing time (defined as the amount of time required to render the PVA solution immobile) after the introduction of GTA (x_{CL} = 0.01) for 8 wt% PVA solutions, demonstrating the crosslinking rate is temperature dependent and consistent with Arrhenius kinetics.

The gelling time for PAA phantoms at room temperature is well-studied and was observed to occur in approximately 5 min after adding the APS initiator at the concentrations of reagents investigated here. This gelling time is difficult to optimize at

higher temperatures, however, since the polymerization reaction is exothermic and heating the monomer solution may result in a runaway polymerization and a gel with non-homogeneous physical properties.

4.3.2 Conformity to submillimeter features

A cross-section of a hydrated, room temperature phantom prepared at 80 °C (x_{CL} = 0.01) is depicted in Figure 4.2A showing a clear, bubble-free phantom. Figure 4.2B shows a crosslinked PVA tissue phantom in the acrylic heating chamber demonstrating conformity and surface-to-surface contact between the phantom and the sub-millimeter thermistor probes and heating element (shown without phantom in Figure 4.2C). PAA solutions polymerized around these features with the same degree of conformity (not shown) and demonstrated identical characteristics, optically.

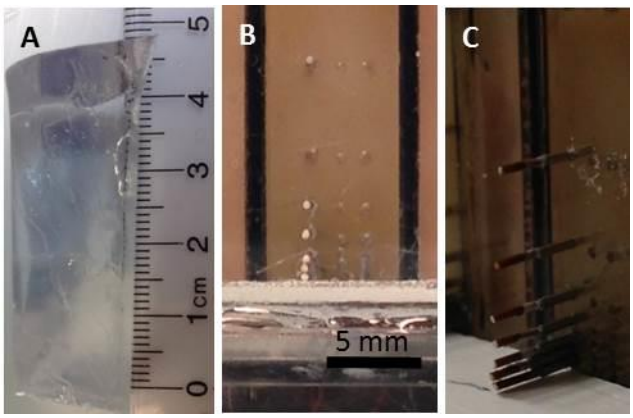

Figure 4.2. Submillimeter surface contact to thermistor probes. A) cross-section of a 1.4 cm-thick, hydrated PVA phantom prepared at 80 °C demonstrating a bubble-free and optically clear tissue mimic. B) an approximately 2.5 cm-thick phantom cast at 80 °C around the thermistor probe array used for heat transfer studies and C) shown without polymer phantom.

4.4 Phantom swelling characterization

Each phantom (approximately 9.5 cm diameter, 1.3 cm thick) was periodically removed from its water bath and patted dry with a paper towel before weighing. The degree of swelling was quantified from this measurement by calculating the volumetric

polymer fraction, Q_s, using Equation 4.1 where ρ_{PVA} is the density of pure PVA and ρ_s is the phantom density.

Equation 4.1

$$Q_s = \frac{\text{mass of dry PVA in hydrogel}}{\text{mass of swollen hydrogel}} \times \frac{\rho_s}{\rho_{PVA}}$$

Phantom volume was determined by immersing the hydrogel in *iso*-octane and weighing the displaced liquid, then dividing by the density of *iso*-octane at 22.5 °C (0.7003 g cm^{-3}).[70] The equilibrium polymer volume fraction, $Q_{S,eq}$, of a PVA phantom was defined when Q_s changed less than 10% over the course of a 7 day period between measurements and less than 2% over the course of a 1 day period. The density of the phantom was measured at the end of each swelling trial; this value was used to calculate Q_s. Across all crosslinking densities, Q_s remained within the range of 1.028 to 1.070 g cm^{-3}. Since this range varied by only 4% across phantoms with substantially different swelling, the end-of-trial density measurement for each phantom was assumed to be representative of the entire trial.

4.4.1 PVA Phantoms prepared at 80 °C

The transient swelling ratio of PVA phantoms crosslinked at 80 °C as a function of x_{CL} is shown in Figure 4.3 which demonstrates a decrease in the polymer volume fraction as a function of time for x_{CL} less than 0.01 and an increase in the polymer volume fraction for x_{CL} greater than 0.01.

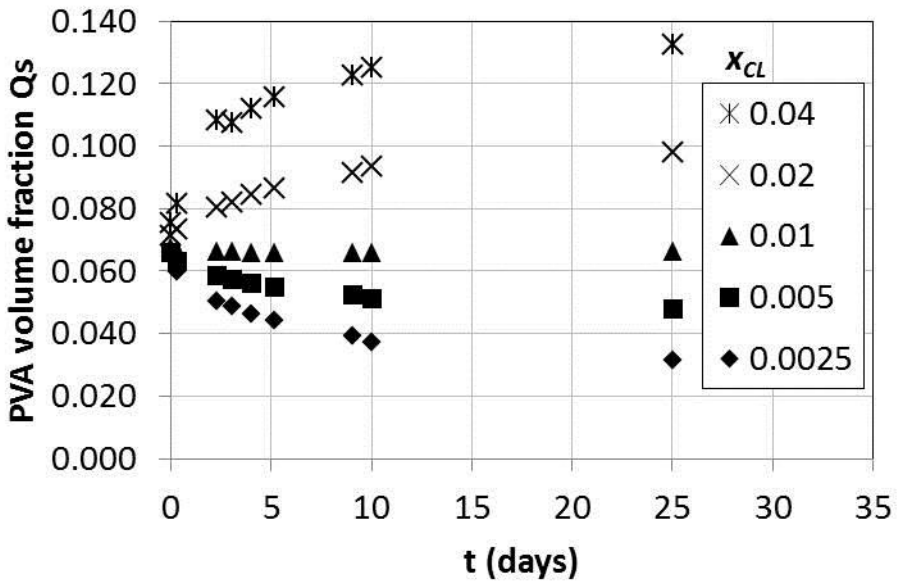

Figure 4.3. Transient volumentric swelling for PVA phantoms crosslinked at 80°C. Mimics were prepared at crosslinking ratios, x_{CL}, ranging from 0.0025 to 0.04, demonstrating an increasing equilibrium PVA volume fraction for increasing x_{CL}; Q_s at t = 0 for all phantoms at all crosslinking ratios was 0.066.

PVA phantoms crosslinked at 80 °C maintain their pre-crosslinked volume if the polymer volume fraction of the PVA solution is equal to $Q_{s,eq}$. For example, an 8 wt% PVA solution crosslinked with 100 mol PVA monomer units to 1 mol GTA (x_{CL} = 0.01) will meet this condition. The volume change in this phantom was less than 0.2% after three weeks in water which indicates excellent shelf-stability at room temperature. To create volume stable phantoms at other polymer volume fractions (*e.g.*, to achieve different mechanical properties) the data presented next in Section 4.4.2 can be used to target a desirable equilibrium polymer volume fraction and interpolate the necessary crosslinker ratio.

Alternatively, 80 °C-prepared tissue phantoms can be purposely designed to trigger a swelling or shrinking event by adjusting the crosslinking ratio. For the 6.6 vol% PVA solutions used here, the phantom will swell to more than twice its volume over a three week period for x_{CL} = 0.0025, but shrink by more than half its volume over the

same time period when x_{CL} = 0.04. All equilibrium swelling data are summarized in Table 4.1 which tabulates the corresponding crosslinking density and temperature.

Table 4.1. Physical properties of PVA tissue phantoms. x_{CL} is the crosslinking ratio, t_q is the quenching time (time when phantom is submerged in water bath), $Q_{s,eq}$ is the equilibrium volumetric swelling ratio, and ξ is the mesh size of the crosslinked network calculated from $Q_{s,eq}$; ∞ indicates curing/quenching times over 3 hours which did not affect the degree of crosslinking.

x_{CL} (mol GTA/mol PVA)	Crosslinking temperature (°C)	t_q (min)	$Q_{s,eq}$ (mL dry PVA/mL hydrogel)	ξ (Å)
0.04	22	110	0.092	76
0.04	22	90	0.087	87
0.04	22	70	0.079	106
0.04	22	50	0.066	145
0.0025	22	∞	0.032	346
0.005	22	∞	0.055	187
0.01	22	∞	0.075	116
0.02	22	∞	0.105	89
0.04	22	∞	0.154	50
0.0025	80	-	0.031	344
0.005	80	-	0.048	221
0.01	80	-	0.066	144
0.02	80	-	0.098	64
0.04	80	-	0.132	66

4.4.2. PVA Phantoms prepared at 22 °C

In addition to varying the amount of GTA, the degree of crosslinking in the PVA phantoms was varied by submerging 22 °C-prepared phantoms in water at various quenching times, t_q, (50 to 110 min) following the introduction of GTA (x_{CL} = 0.04). The transient swelling profiles shown in Figure 4.4 demonstrate the effect of t_q on the equilibrium polymer volume fraction which increases (more crosslinking) for longer quenching times. The equilibrium polymer volume fraction was reduced by more than half when the reaction was quenched at times less than 120 min due to the removal of

unreacted GTA molecules and hydronium ions which catalyze the crosslinking reaction. These shortened reaction times can be implemented to the user's advantage to achieve different swelling ratios for the same crosslinking ratio (*i.e.*, if it is desirable to crosslink at low temperatures and short reaction times). Increasing the quenching time above 120 min did not have any effect on the final equilibrium swelling ratio (not shown). Thus, all phantoms prepared at 22 °C were kept unexposed to water for at least 3 hr (denoted as $t_{q,\infty}$) when varying x_{CL} in order to achieve the maximum amount of crosslinking for a specific GTA concentration.

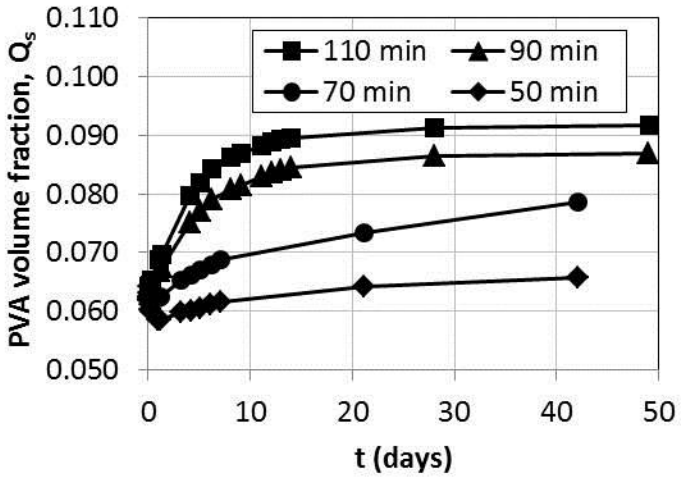

Figure 4.4. Transient volumetric swelling ratio for PVA phantoms crosslinked at 22 °C. Phantoms were quenched in 5 L of water at times, t_q = 50, 70, 90, and 110 min after the introduction of GTA (x_{CL} = 0.04); Q_s = 0.066 at t = 0 which was the initial PVA volume fraction in the prepared solution. The equilibrium swelling ratio, $Q_{s,eq}$, decreased for decreasing t_q, which indicates fewer crosslinks form at shorter t_q.

Previously reported swelling ratios by Canal and Peppas for PVA gels of unknown thickness and crosslinked with GTA at room temperature for 2 hr are given in Figure 4.5 as a function of x_{CL} (0.0033 to 0.056).[69] The values were in good agreement with the $Q_{s,eq}$ values reported here for 1.5 cm-thick PVA hydrogels crosslinked at 22 °C for 3 hr. This suggests that not only are GTA-crosslinked PVA gels reproducible as a

tissue phantom material, but that the aspect ratio of the PVA gel does not impact the time required for the PVA network to completely crosslink.

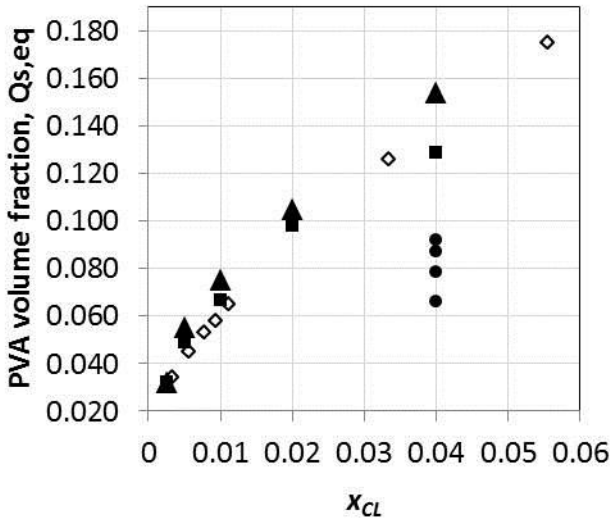

Figure 4.5. Equilibrium swelling versus crosslinking ratio. Equilibrium volumetric swelling ratios of GTA-crosslinked, PVA tissue phantoms prepared at 80 °C (■) demonstrate the same dependence on crosslinking ratio as PVA hydrogel films reacted for 2 hr by Canal and Peppas (◊).[23] PVA phantom crosslinking completes in approximately 3 hr regardless of GTA content as demonstrated by unquenched ($t_q = \infty$) phantoms prepared at 22 °C (▲). Phantoms prepared at 22 °C that were quenched at 110, 90, 70, and 50 min after the addition of GTA (●) (x_{CL} = 0.04) resulted in lower equilibrium Q_s for decreasing t_q indicating a lower degree of crosslinking despite the same initial concentration of GTA.

4.4.3 Differences in equilibrium swelling at 22 vs. 80 °C

The equilibrium swelling ratio for an 80 °C-prepared PVA phantom was 10% (± 7.3%) lower than $Q_{s,eq}$ for the 22 °C-prepared phantoms at identical crosslinking ratios (Figure 4.5). Although both phantoms were crosslinked with the same initial amount of GTA, the slightly higher equilibrium swelling ratio indicates a slightly higher degree of crosslinking in the 22 °C-prepared phantoms. One hypothesis is that the faster crosslinking kinetics in the 80 °C-prepared phantom increases the probability that both dialdehyde moieties of a GTA molecule react on the same polymer chain, creating a short loop rather than a cross-link between chains. At room temperature this probability decreases as the unreacted end of a PVA-linked GTA moiety has more time to diffuse

with its polymer chain into proximity with another polymer chain before reacting, thereby creating a true cross-link. Physically, this means the room temperature prepared phantoms produce a more highly crosslinked network and thus a measurably higher $Q_{s,eq}$ despite the same amount of GTA reacting. To produce a tissue phantom with the same volume stability observed with the 80 °C-prepared phantom from an 8 wt% PVA solution, the amount of GTA for a 22 °C-prepared phantom would need to be decreased as indicated in Figure 4.5.

4.4.4 PAA phantom swelling

Similar to the PVA phantoms prepared at low crosslinking densities (x_{CL} less than 0.01), the PAA phantoms increased in volume as a function of time when stored in water as shown in Figure 4.6 which demonstrates a 16% decrease in the polymer volume fraction in the first 48 hours of swelling and roughly 5% per day after day four. Even when increasing the amount of crosslinker (MBA) by a factor of 10, the PAA phantoms still swell by 13% after 10 days. In addition, the gelled phantoms at this higher crosslinking density are opaque (not shown) which would hinder its use in applications that require a transparent phantom such as medical imaging. Further, this opacity could indicate non-homogenous polymerization throughout the hydrogel which would result in spatially varying thermal properties throughout the tissue phantom.

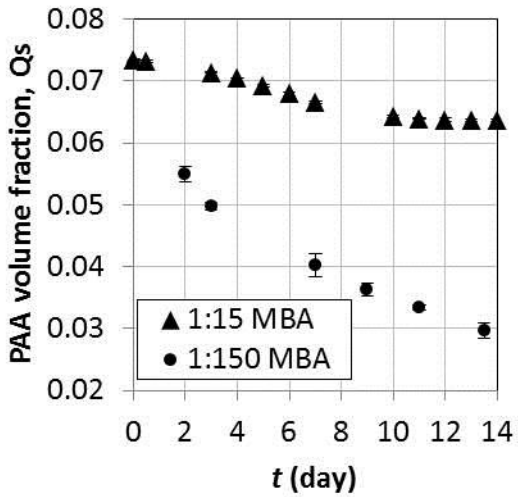

Figure 4.6. Transient volumetric swelling ratio for PAA phantoms. 8 wt% acrylamide solutions polymerized with MBA:AA = 1:150 swelled to nearly 2.5 times their original volume when stored for 2 weeks in water. PAA phantoms crosslinked with 10 times more MBA swelled by 13% in the same time.

4.4.5. Mesh size

Using Equation 4.2 reported by Canal and Peppas, the mesh size, ξ, of a GTA-crosslinked PVA network was calculated from the equilibrium swelling value where k_1 = -310.1 Å, k_2 = 117.0, and n = -0.5 for $Q_{s,eq}$ values between 0.01 and 0.10 (R^2 = 0.9972) and k_1 = -31.6 Å, k_2 = 12.6, and n = -1.0 for $Q_{s,eq}$ values greater than 0.10 (R^2 = 0.9091).[69]

Equation 4.2

$$\xi = k_1 + k_2\left(Q_{s,eq}\right)^n$$

Using the 80 °C method to prepare PVA tissue phantoms, small molecule agents can be diffused into the phantom post-gelation by taking into account this mesh size reported in Table 4.1 as a function of x_{CL}. Such scenarios have been reported elsewhere for crosslinked PVA although these systems usually incorporate the reagent during crosslinking.[83-84]

4.4.6 Temperature dependent swelling

For measuring changes in hydrogel swelling as a function of temperature, hydrogels were transferred from room temperature immersion into a temperature controlled, circulating water bath (Model 9101, Fisher Scientific) whose initial temperature of 37 °C was increased to 50 °C after one hour, then increased in 10 °C increments each hour up to 80 °C. The hydrogel mass was measured every hour, in triplicate.

Figure 4.7 demonstrates the percent decrease in volume for both 22 °C- and 80 °C-prepared phantoms with x_{CL} = 0.01 when heated in a temperature controlled water bath, 24 hr after casting. The 80 °C-prepared phantoms lost less than 5% or their original volume over the course of a 5-hour trial reaching 80 °C (far longer and hotter than the time duration of a typical hyperthermia experiment) while the 22 °C-prepared phantoms lost nearly 10% of their volume. The reason for this slight decrease in volume when exposed to heat treatment is not immediately obvious but is likely due to non-covalent interactions between water and the hydroxyl groups that are affected by temperature. These phantoms were not returned to a room temperature water bath and thus swelling ratios were not measured after the experiment to check if this phenomenon was reversible. However, this phenomenon is likely similar to the temperature sensitivity of the hydrogel material, poly(n-isopropylacrylamide) (pNIPAM). At temperatures below 33 °C, pNIPAM is hydrophilic but will shrink by up to 90% by volume as the temperature of the hydrogel is elevated due to hydrophobic interactions which are induced at temperatures above 33 °C.[85] This same effect is likely driving the slight loss of volume in the crosslinked PVA mimics used here but at a much smaller degree.

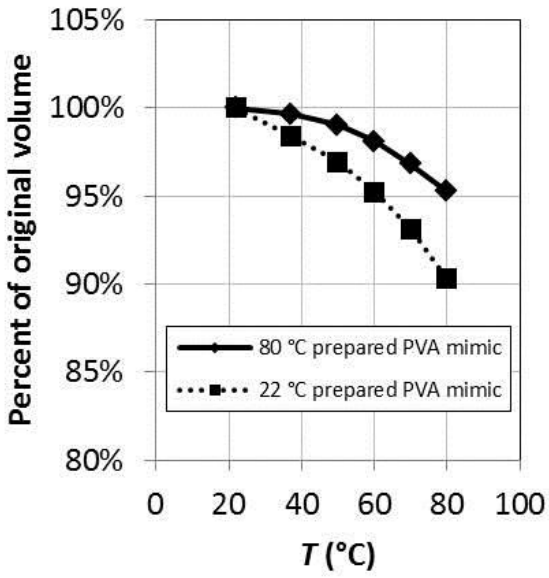

Figure 4.7. Temperature dependent volume stability. Degree of volume loss for PVA phantoms when submerged in a temperature controlled water bath for 1 hr at 50, 60, 70, and 80 °C, measured consecutively in that order. Both the 80 °C- and 22 °C-prepared mimics lost 5 and 10% of their volume, respectively over the course of the 5 hr experiment; x_{CL} = 0.01.

4.5 Phantom/filler composite synthesis

Silicon carbide (SiC) (400 mesh particle size, Sigma Aldrich) and low molecular weight poly(vinyl chloride) (PVC) resin (150 mesh particle size, Sigma Aldrich) were added as fillers (25 wet wt%) to both the acrylamide monomer solution and noncrosslinked PVA solutions to modify the phantoms' thermal properties. For the PVA system, these materials were added to 8 wt% PVA solutions at 80 °C under vigorous stirring to maintain particle dispersion. Immediately after adding the crosslinker, these solutions were poured into their intended mold which gelled within 20 to 30 sec. PAA-filled phantoms were prepared per Section 4.2 but with the filler replacing an equal amount of 8 wt% acrylamide solution. Monomer/filler solutions were then poured into their intended mold 30 sec after adding the initiator.

Filler dispersion in the cross-sections of gelled phantoms was observed visually and with an optical microscope. Light microscope images of hydrated phantoms

containing 19.7 vol% PVC and 10.4 vol% SiC (both 25 wt%) are shown in Figure 4.8, indicating homogenous distribution of the filler throughout the PVA hydrogel matrix and PVC and SiC particle sizes less than 150 and 20 μm, respectively. The observed settling time for a 10.4 vol% SiC, 8 wt% PVA solution at room temperature was much slower than the Stokes Law prediction (0.85 mm min^{-1}) for a room temperature 8 wt% PVA solution, whose viscosity was measured at 31.8 ± 0.3 cP.[86] This indicates not only that particle aggregation was minimal, but also that the viscosity of the PVA solution at rest is much higher than that measured with a falling ball viscometer, typical of non-Newtonian liquids such as polymer solutions. Consequently, the 22 °C-prepared phantoms experienced less than 0.5 mm of particle settling during the 90 min curing time required for crosslinking. At 80 °C the viscosity of the filler solution is lower, but the short gelation time (20 sec) still makes settling negligible as seen in Figure 4.8C. In the PAA system, particle fillers loaded at identical volume fractions settled completely to the bottom of the mimic prior to gelling as shown in Figure 4.8D due to the monomer solution having a viscosity comparable to water and despite a gelation time of less than 5 min.

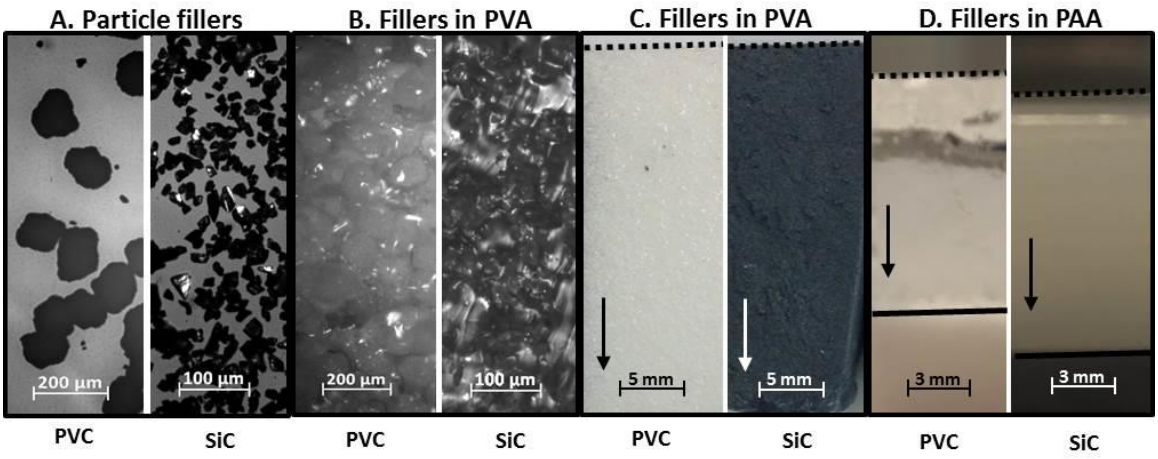

Figure 4.8. Filler dispersion in hydrogel phantom. A) Light microscope images of dry, PVC and SiC filler particles B) Light microscope images of 19.7 vol% PVC and 10.4 vol% SiC immobilized in hydrated PVA phantoms C) Macroscopic images of 19.7 vol% PVC and 10.4 vol% SiC immobilized in hydrated PVA phantoms; arrows indicate direction of settling during curing; dashed lines indicate top of phantoms demonstrating uniform dispersion throughout the entire thickness of the phantom; D) Macroscopic images of 19.7 vol% PVC and 10.4 vol% SiC immobilized in hydrated PAA phantoms; solid line indicates top of settled fillers in the polymerized hydrogel demonstrating a significant thickness of clear phantom between the top of the mimic (dashed line) and the filler.

4.6 Heat transfer characterization

Thermal characterization of the PVA phantoms was performed in a custom-built, 6.45 cm^2 by 15.2 cm-long acrylic chamber shown in Figure 4.9A. PVA solutions with or without thermal modifiers were poured into the chamber immediately after GTA addition at 80 °C and allowed to crosslink and cool to room temperature for 6 hr prior to thermal modeling. The gelled phantom's thickness was measured after the heat transfer study using a hand-held micrometer; all phantoms were approximately 2.5 cm thick and wide and spanned the entire 15.2 cm length of the heating chamber.

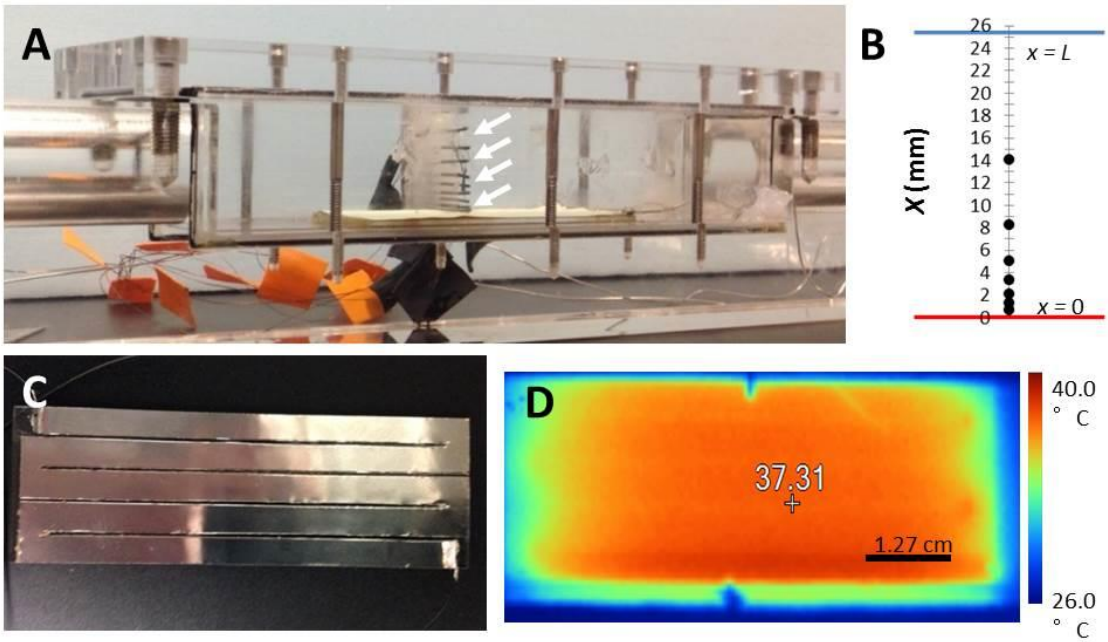

Figure 4.9. Heat transfer measurement station. A) PVA phantom solution is poured into a rectangular, acrylic chamber around protruding temperature probes (indicated by white arrows) B) distribution of temperature probes in chamber as a function of the distance, *x*, away from the heating element C) nichrome foil heating element used for applying temperature boundary conditions via PID temperature feedback control D) IR thermal image of heating element with a 37 °C temperature setpoint, demonstrating uniform heating.

A temperature boundary condition was imposed at the bottom surface of the PVA phantom using a 2.5 cm by 7.6 cm electrical resistance heater positioned under the middle of the phantom. A 0 °C temperature boundary condition was imposed on the top of the phantom using a 19.4 cm^2 by 6.4 mm-thick slab of ice positioned directly over the heating element.

The 19.4 cm^2 resistance heater was fabricated from 25 µm-thick nichrome foil (Ni80/Cr20, Goodfellow Corporation) as shown in Figure 4.9C. The foil was cut to achieve five, 5.1 mm-thick paths totaling a length of approximately 12.7 cm to produce an electrical resistance of approximately 3.24 ohm. The surface of the foil heating element was coated with approximately 500 µm of thermal grease made from a 50/50 mixture of zinc oxide/vacuum grease (submicron zinc oxide, 99.9%, Sigma Aldrich/Dow corning) to uniformly distribute the temperature across the heating element surface.

Temperature variance across the middle 5.1 cm of the heating element was ± 1.2 °C, measured with an IR, thermal camera (FLK-TIR4-FT-20, Fluke) as shown in Figure 4.9D. The temperature boundary condition was monitored at the heating element/phantom interface using a 550 µm-diameter, polyimide-insulated thermistor probe (± 0.1 °C, Selco Products) attached directly to the nichrome foil surface with a silver nanoparticle colloid adhesive (PELCO conductive silver 187, Ted Pella, Inc.) and embedded in the thermal grease. Using this probe, a PID feedback control system in LabVIEW software (National Instruments) drove a 0 – 18 V, 0 – 5 A programmable DC power supply (1785B, BK-Precision) to maintain the target surface temperature.

Each mimic was used only once per heat transfer trial then removed and discarded. The target surface temperature boundary condition at the bottom of the phantom was set between 40 and 80 °C (± 0.1 °C) and was held for no more than 7 min per heat transfer trial. For trials requiring a 0 °C boundary condition, the ice-block was placed on top of the mimic immediately after the power source was turned on to the heating element so that both the top and bottom temperatures were implemented at the same time (± 5 sec). An array of thermistor probes (550 µm-diameter, polyimide-insulated) were aligned between the temperature-controlled boundary surfaces at distances shown in Figure 4.9B whose spacing was measured optically with a custom-designed scale-bar of known spacing. Temperature measurements from all probes were logged every second using an 8-channel temperature DAQ device (USB-TEMP, Measurement Computing Corporation) and LabVIEW software.

4.6.1 Thermal diffusivity

Temperature boundary conditions were imposed at the top (T = 0 °C) and bottom (T = 40 °C) surface of an approximately 2.5 cm-thick PVA phantom using the heat transfer station in Figure 4.9. The resulting transient temperature profile was used to back calculate the thermal diffusivity, α, from a least squares fit to the exact solution of $T(x,t)$ derived from the one-dimensional, transient heat equation (Equation 4.3) with constant temperature boundary conditions presented by Carslaw and Jaeger in Equation 4.4; where k is the thermal conductivity, C_P is the specific heat capacity, ρ is the density, T_0 is the temperature in the phantom at t = 0 determined by averaging the room temperature values of all temperature probes at t = 0, and L is the thickness of the phantom and the location of the 0 °C temperature boundary condition (*i.e.*, $T(x,0) = T_0$ = averaged room temperature value, $T(0,t) = T_1$ = 40 °C and $T(L,t) = T_2$ = 0 °C).[87]

Equation 4.3

$$\frac{\partial T}{\partial t} = \alpha \frac{\partial^2 T}{\partial x^2} \qquad \text{where } \alpha = \frac{k}{c_P \rho}$$

Equation 4.4

$$T = T_1 + (T_2 - T_1)\frac{x}{L}$$

$$+ \frac{2}{\pi}\sum_{1}^{\infty} \frac{T_2 \cos n\pi - T_1}{n} \sin\frac{n\pi x}{L} e^{-\frac{\alpha n^2 \pi^2 t}{L^2}}$$

$$+ \frac{2}{L}\sum_{1}^{\infty} \sin\frac{n\pi x}{L} e^{-\alpha n^2 \pi^2 t/L^2} \int_0^L T_0 \sin\frac{n\pi x}{L} dx$$

Experimentally, the 40 °C boundary condition was achieved in 10 s by the PID controlled heating element with 5.1 °C overshoot and a steady, 40 °C temperature was achieved within 1 °C of the setpoint in less than 25 sec indicating a very rapidly applied boundary condition at t = 0 s as shown in the left plot of Figure 4.10.

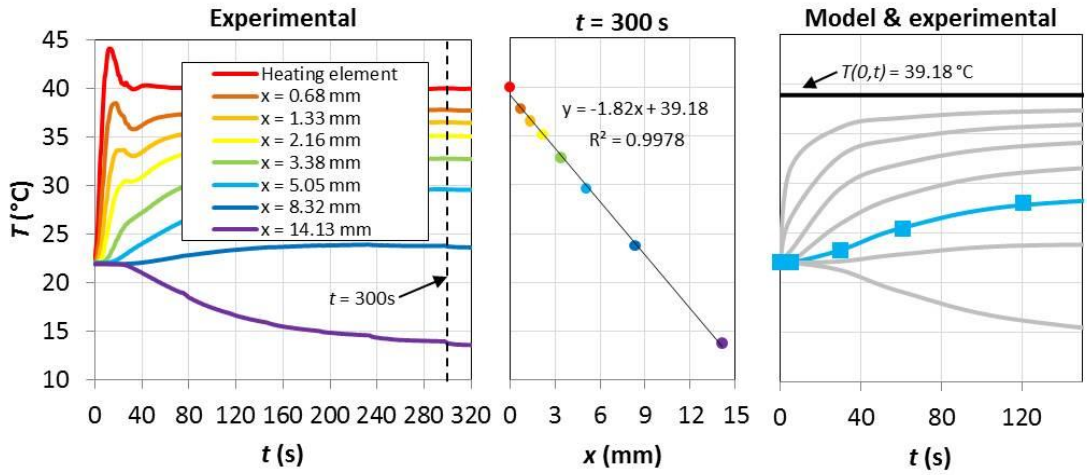

Figure 4.10. Thermal diffusivity calculation from experimental data. The left graph gives the experimental, transient temperature data obtained from a 2.5 cm-thick, plain PVA phantom cured in the heat transfer station. At the top and bottom of the mimic, T = 0 °C and 40 °C, respectively, demonstrating a 40 °C setpoint/boundary condition achieved at the heating element surface in 15 s with less than 5 °C overshoot (red curve); steady state was achieved at t = 300 s (vertical, dashed line). The middle graph plots this steady state temperature profile as a function of the distance away from the heating element, x, (R^2 = 0.9978) which was used to interpolate the boundary condition $T(0,t)$ used for fitting Equation 4.4 to experimental data. The right graph plots the transient solution of Equation 4.4 for all corresponding thermistor probe distances, x, away from the T = 39.18 °C boundary condition; blue squares indicate the temperature measurements pulled from the experimental data corresponding to the thermistor at x = 5.05 mm (blue curve) used for fitting Equation 4, demonstrating good agreement with the model.

Since the driving thermistor was attached directly to the nichrome foil and imbedded in thermal grease, the exact temperature boundary condition at the PVA phantom interface was interpolated from a linear fit to the steady state temperature profile as a function of x, shown in the middle plot of Figure 4.10.

A typical temperature profile for a plain PVA phantom used for calculating thermal diffusivity obtained from Equation 4.4 is shown in the right plot of Figure 4.10. Temperature data collected with the thermistor probe at x = 5.05 mm was used for calculating k to minimize the error induced by the overshoot in power to achieve the 40

°C boundary condition at $x = 0$. After fitting, the analytical temperature profile was in good agreement with the experimental transient temperature profile for this thermistor as shown by the solid blue curve (analytical solution) and the blue squares (experimental) in the right plot of Figure 4.10.

The mass-averaged heat capacities used for the phantoms investigated here were calculated from the heat capacity of PVA,[88] PVC,[89] SiC,[90] and water (1.6, 0.97, 0.70, and 4.18 J g^{-1} $°C^{-1}$, respectively). These values, in addition to the measured densities (buoyancy method in *iso*-octane, see Section 4.4), were used to back-calculate the thermal conductivity, $k = \alpha\rho C_P$ from the experimental thermal diffusivity. Thermal conductivity values were measured in triplicates for all three tissue phantom/filler combinations: plain PVA, PVA with PVC resin (volume fraction, ϕ = 19.7 vol%), and PVA with SiC powder (ϕ = 10.4 vol%) and are listed in Table 4.2.

Table 4.2. Experimentally measured thermal conductivity for PVA phantom, PVA/PVC composite phantom, and PVA/SiC composite phantom. Indicated error is standard deviation (n=3).

Material	ϕ	$\alpha \cdot 10^7$ (m^2 s^{-1})	C_P (J g^{-1} $°C^{-1}$)	ρ (g cm^{-3})	k (W m^{-1} $°C^{-1}$)	k_{eff} (W m^{-1} $°C^{-1}$)
Water	-	1.44	4.18	0.998	0.600	-
PVA	-	1.41 ±0.01	3.97	1.028 ±0.002	0.578 ±0.002	-
PVA/PVC	0.197	1.36 ±0.05	3.21	1.091 ±0.005	0.475 ±0.019	0.473
PVA/SiC	0.104	1.97 ±0.09	3.16	1.274 ±0.024	0.795 ±0.038	0.777

In addition, the theoretical thermal conductivity, k_{eff}, of a composite material containing spherical, non-interacting particles was estimated using Equation 4.5 derived by Maxwell , where ϕ is the volume fraction of filler, k_0 is the thermal conductivity of the continuous phase (0.578 W m^{-1} $°C^{-1}$ for PVA hydrogel), and k_1 is the thermal conductivity of the filler material (1.4 and 120 W m^{-1} $°C^{-1}$ for PVC and SiC, respectively).[86]

Equation 4.5

$$\frac{k_{eff}}{k_0} = 1 + \frac{3\phi}{\left(\frac{k_1 + 2k_0}{k_1 - k_0}\right) - \phi}$$

The PVC and SiC fillers used here show that PVA phantoms can be homogeneously incorporated with particles as large as 150 µm to achieve a desirable mechanical or thermal property effect. Equation 4.5 predicts thermal conductivities of 0.473 and 0.777 W m^{-1} $°C^{-1}$ for the 19.7 vol% PVC and 10.4 vol% SiC filled phantoms, respectively, which are in good agreement with the experimentally measured values in Table 4.2. Thus, the required volume fraction of filler can be predicted using Equation 4.5 for a desired thermal conductivity over a range of physiologically relevant values from 0.475 to 0.795 W m^{-1} $°C^{-1}$ as shown here.

This investigation reports a method for calculating the thermal diffusivity of a hydrogel that does not require a known heat flux or insulating boundary conditions due to the transient nature of the one-dimensional solution procedure and accurate temperature acquisition at carefully measured locations using submillimeter-sized thermistor probes. In addition, steady temperature boundary conditions were obtained very rapidly (less than 25 sec) as demonstrated in Figure 4.10. The strong agreement (less than 5% difference) in the measured thermal conductivity values for each of the three different phantom types reported in Table 4.2 substantiates the uniformity of particle fillers in the PVA system using the reported 80 °C crosslinking method.

4.7 Transient heating for a single temperature boundary condition

One example application using a volume stable, PVA tissue phantom is determining the degree of tissue damage induced by increasing the temperature of a medical implant surface, *in situ*, in order to mitigate and treat bacterial biofilm infections. Chapter 3 demonstrated *Pseudomonas aeruginosa* biofilm populations are decreased by 4.5 orders of magnitude when held at 80 °C for 5 min. Since mammalian cells and tissue will be irreversibly damaged at temperatures above 43 to 47 °C, the relative tissue damage for various thermal protocols (*e.g.*, 80 °C for 5 min) may be estimated by determining the tissue thickness for which the temperature has exceeded 47 °C.[91] This was modeled using a 2.5 cm-thick PVA phantom in the heat transfer station by imposing a single temperature boundary condition at the heating element/tissue phantom interface.

The results are shown in Figure 4.11 which plots the 10 °C temperature increase isotherm for a surface heated to either 50 or 80 °C for 7 min; the initial temperature of the tissue phantom was at room temperature, approximately 23 °C. These isotherms show, for example, rapid heating of the nearest few millimeters regardless of surface temperature, with millimeters of additional heated tissue at longer times when at 80 °C, as expected. The maximum power delivered by the heating element to reach these temperatures at the tissue mimic interface was 4.5 W cm^{-2} as measured by multiplying the voltage and the current delivered to the heating element and dividing by its total surface area.

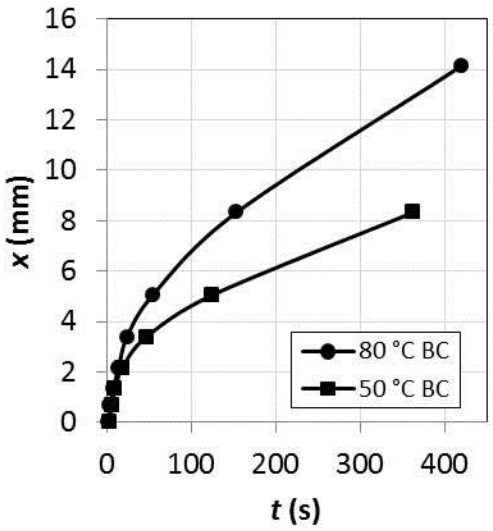

Figure 4.11. Experimental heat transfer study in PVA phantom. Conduction-only heat transfer in an approximately 2.5 cm-thick PVA tissue phantom cast in the experimental heat transfer station with a temperature boundary condition (BC) applied at the bottom of the phantom and insulating boundary conditions on all other sides. Curves represent the time, t, required for the temperature in the tissue phantom to rise 10 °C at a distance, *x*, away from the temperature boundary condition; irreversible tissue damage will occur at 43 to 47 °C.[91]

4.8 Conclusions

PVA crosslinked phantoms showed clear advantages over traditionally-used PAA mimics, whose swelling properties are much more difficult to control. By tuning the crosslinker concentration for an equilibrium swelling ratio that matched the initial water content of the solution, pourable, volume-stable PVA hydrogel tissue phantoms were demonstrated. Increasing the curing temperature of the PVA system narrowed the curing time and further minimized any particle settling of inert fillers, whereas the lower viscosity acrylamide system resulted in rapid, complete particle settling at identical filler concentrations and phantom thicknesses. By homogeneously dispersing property-modifying inert fillers, the thermal conductivity of the phantoms was tuned across a wide-range of physiologically relevant values, matching theoretical predictions to within 2% with less than 5% experimental variation. Additional scenarios and complications such as imposing a biofilm beneath the mimic, incorporating blood perfusion channels,

and complex device surface geometry may all be accommodated by the PVA tissue mimic developed and used here. This facile procedure for robust, versatile tissue phantoms is expected to greatly enhance *in vitro* thermal modeling across a wide range of biological applications.

CHAPTER 5: *IN VITRO* HEAT TRANSFER THROUGH COMBINED TISSUE MIMIC CONDUCTION/ FORCED CONVECTION OVER A HEATED PLATE

While the goal of the present work was to develop a robust experimental model—one that incorporates blood perfusion and heat generation due to metabolism—the foundation for implementing these mechanisms is established with the future goal of validating the terms used in the bioheat transfer equation, Equation 1.2, described in Chapter 1. Exact solutions exist for experimental heat transfer through a solid hydrogel tissue mimic and fluid mimic, separately, but an analytical solution that combines these two scenarios over the same boundary condition does not. In this chapter, a numerical model is validated against experimental temperature measurements by solving a three-dimensional energy equation for boundary conditions specific to heat transfer in the body from a heated, implanted surface. These models are used to guide design of the intended magnetic/polymer composite coating since different heat sinks will require different power loadings, perhaps along the same surface.

5.1 Heat transfer scenarios

Three scenarios are modeled both experimentally and computationally and span the minimum and maximum heat sink conditions that would be experienced in the body. Experimental measurements validate the numerical heat transfer model which is then used to predict power loadings required by a magnetic composite for scenarios which are not experimentally accessible. Heat transfer propagates the furthest through solid tissue in a conduction-dominated scenario with no convective heat losses as shown in Figure 5.1A. While actual tissue will have additional heat losses and generation due to blood perfusion and cellular metabolism, respectively, the hydrogel tissue phantom used experimentally

here largely mimics the thermal properties and heat sink of real tissue as was measured in Chapter 4. Power requirements to impose a temperature boundary condition under this scenario will be much smaller than a convection-dominated scenario shown in Figure 5.1B which represents the same boundary condition next to a fluid mimic such as blood flowing through a human aorta. Finally, in Figure 5.1C both scenarios are implemented over the same boundary condition (either constant heat flux or constant temperature) which cannot be solved analytically. This last scenario represents the case when the same magnetic coating must provide a power gradient across the coating to keep the entire surface at the same temperature despite different heat sinks. Otherwise, the same amount of energy will propagate through the solid tissue that is required to keep the fluid-exposed portion of the surface at temperature. Conversely, specifying a temperature on the tissue covered portion of the surface will result in the fluid side not reaching the target temperature.

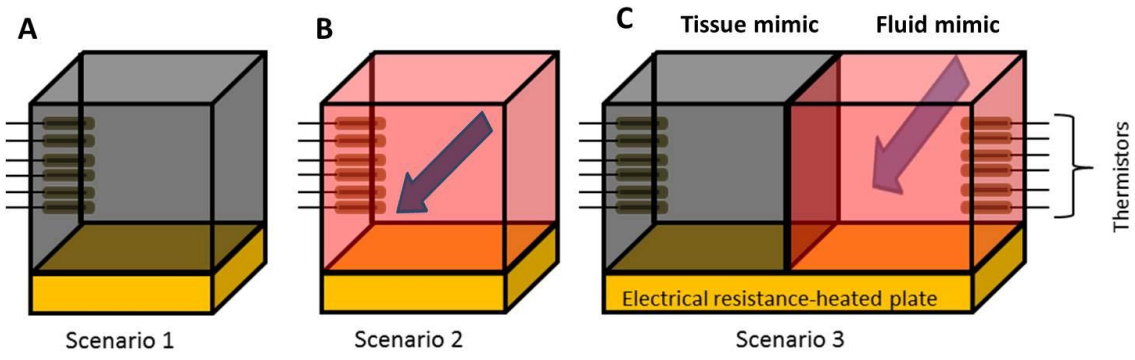

Figure 5.1. Modeled heat transfer scenarios. A) Conduction-only scenario through solid hydrogel tissue mimic (Scenario 1). B) Convection-only scenario through fluid mimic (Scenario 2); arrow indicates direction of fluid flow. C) Combined tissue mimic, fluid mimic scenario over the same boundary condition (scenario 3). Boundary condition applied with PID controlled, electrical resistance heated plate; heat transfer measured perpendicular to boundary condition by imbedded thermistor probes.

5.2 3D-printed heat transfer measurement station

5.2.1 Flow-cell design

A single flow cell was designed and 3D-printed that accommodates all three heat transfer scenarios investigated here and is shown in Figure 5.2. The entire chamber area is a 2.54 cm high (h) by 2.54 cm wide (w) square duct (y- and z-direction, respectively) that is 15.24 cm long (L) (x-direction). For the conduction only scenarios, poly(vinyl alcohol) (PVA) tissue mimics were poured and crosslinked in place throughout the entire chamber volume at room temperature per the methods presented in Chapter 4.1 with a crosslinking ratio, x_{CL} = 0.01 and with no fillers added. A water fluid mimic was pumped down the length of the duct for 5.08 cm to fully develop flow (*i.e.* no velocity gradients in the x-direction) at which point it flows over a 7.62 cm long by 2.54 cm wide heating element (the same shown in Figure 4.9 in Chapter 4). After the heating element, the fluid continues 2.54 cm down the duct and then exits the flow cell. The fluid mimic was pumped through the flow cell at 0.2 L min^{-1} (Re = 147 for 2.54 cm by 2.54 cm duct) and was maintained at room temperature, 24.0°C, by a temperature controlled water bath.

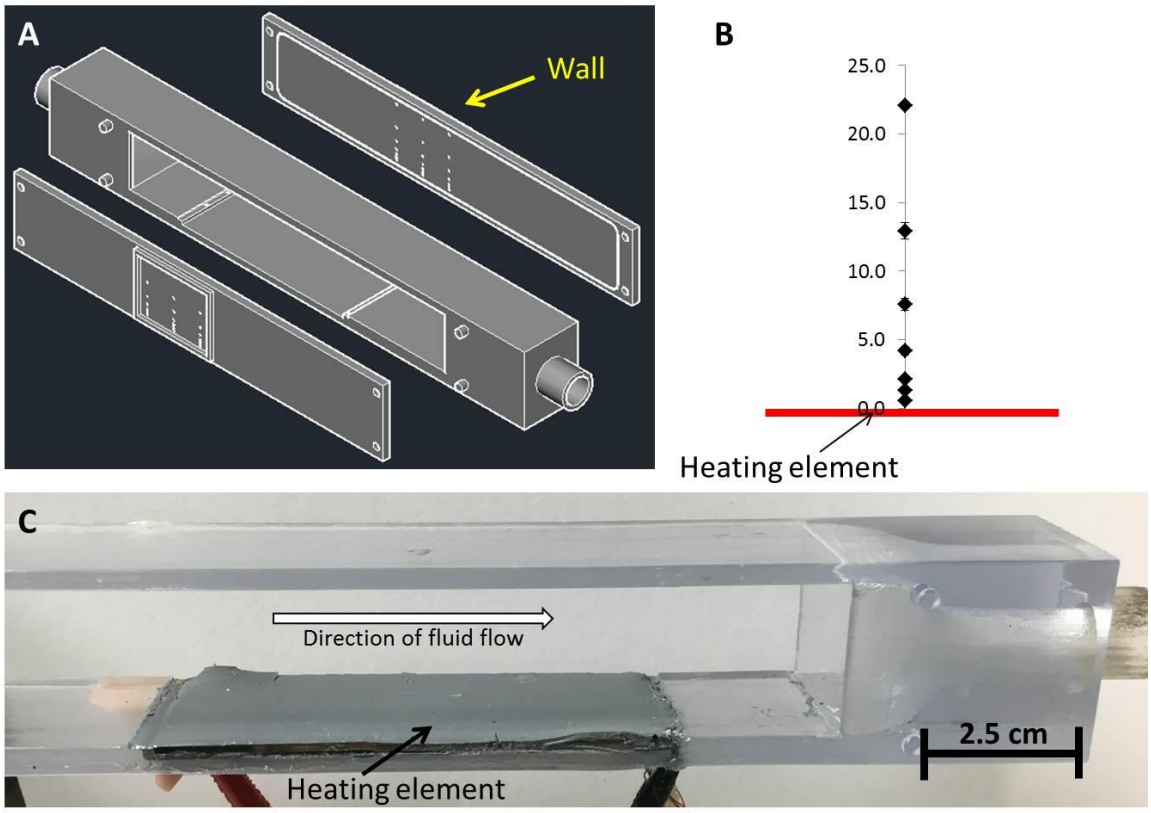

Figure 5.2. Heat transfer station schematics. A) AutoCAD drawing of flow cell chamber with removable walls on sides. B) These walls hold the thermistor probes which were spaced away from the heating element in three arrays on each wall with the middle array centered over the middle of the heat element for a total of 24 possible probe positions on each wall. C) Printed flow cell with PDMS/Silicon carbide coated heating element.

5.2.2 Flow-cell walls and temperature probe position

In addition to the main chamber of the flow cell, the flow cell walls were 3D printed using an Object260 Connex3 printer using VeroClear RGD810 PolyJet ink (Stratasys) and were fully removable to allow for full access to the main chamber. Thermistor temperature probes (550 µm-diameter, polyimide-insulated, Selco Products) were spaced laterally away from the heating element with spacing shown in Figure 5.2B. Up to three arrays of thermistors were embedded in each wall with the middle array positioned over the middle of the 7.62 cm long heating element and an upstream and downstream array offset 1.27 cm from this middle array for a total of 24 possible thermistor locations in each wall. These probes were embedded in the flow cell wall

using stainless steel hypodermic tubing and protruded 6 mm into the flow cell chamber. This protrusion depth was determined from a 2D numerical model (using ANSYS FLUENT) of the flow-cell cross section as shown in Figure 5.3. This model shows the temperature gradient through the wall where the embedded probe heads were located. Initially, the thermistor probe heads were embedded directly into the wall but temperature measurements from these probes demonstrated lower than expected values which is likely due to the temperature gradient observed in Figure 5.3. Thus, the probe heads were extended 6 mm into the flow chamber to measure a more accurate temperature field.

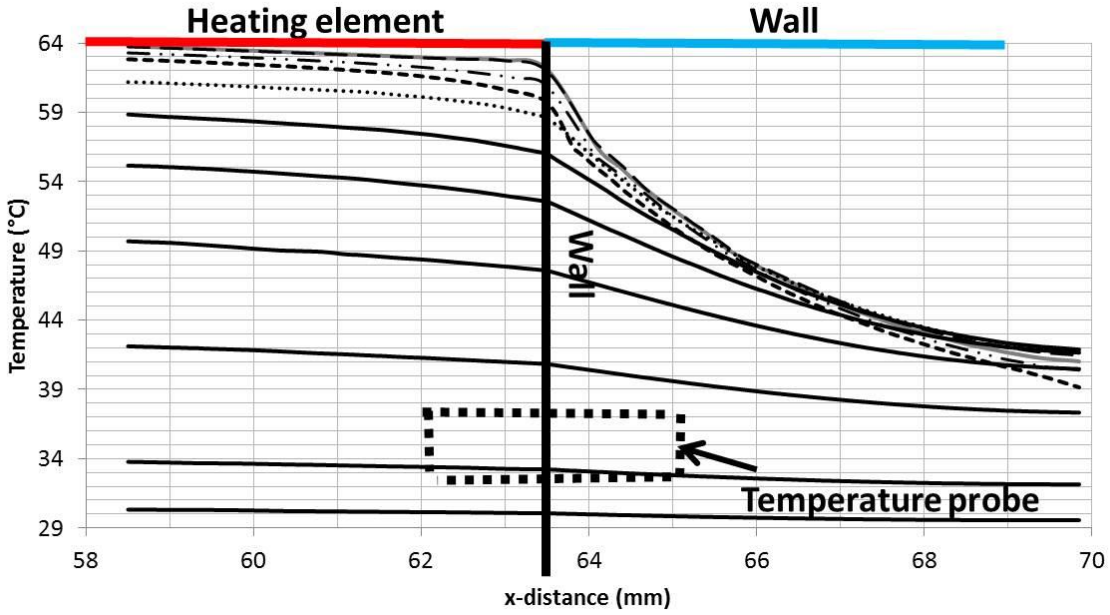

Figure 5.3. Model-guided placement of thermistors probes. Initially, the thermistor temperature probe heads used for heat transfer measurement were embedded into the flow cell wall (indicated by the dashed square). This 2D model of the flow chamber cross section shows large temperature gradients through the wall where the probe heads were located. Thus diminished temperatures were observed that did not represent the true temperature field in the flow cell chamber.

5.2.3 Heated plate design

The same heating element which was designed and discussed in Chapter 4.6 was used again in the 3D printed heat chamber but instead coated with a 50/50 composite mixture of poly(dimethyl siloxane) (PDMS) and inert silicon carbide to both protect the nichrome foil from corrosion and to create a uniform heat flux across the heating element surface. This heating element is shown installed in the 3D printed flow cell in Figure 5.2C. Temperature feedback control was implemented using the same PID feedback controller used in Chapter 4.6 to implement constant temperature boundary conditions underneath the mimics.

5.2.4 Data acquisition

Temperature measurements were collected every second using the same DAQ devices and LabVIEW program described in Chapter 4.6.

5.3 Computational model

5.3.1 Governing equations and finite differencing

Three-dimensional energy transfer was numerically modeled using Equation 5.1.

Equation 5.1

$$\frac{\partial T}{\partial t} = \alpha\left(\frac{\partial^2 T}{\partial x^2} + \frac{\partial^2 T}{\partial y^2} + \frac{\partial^2 T}{\partial z^2}\right) - \frac{\partial (uT)}{\partial x}$$

where T is the temperature (°C), t is time (s), α is the thermal diffusivity ($m^2\ s^{-1}$), x is the direction down the length of the heating chamber (the direction of fluid flow), y is the direction spanning the flow cell height and is perpendicular to the heating element, z is

the direction spanning the width of the flow cell and is parallel to the heating element, and u is the x-component velocity of the velocity field. This velocity field was obtained analytically from the x-momentum and continuity equations assuming an incompressible fluid (*i.e.* constant viscosity and density) given in Equation 5.2.

Equation 5.2

$$\rho\frac{\partial u}{\partial t} = -\frac{\partial P}{\partial x} + \mu\left(\frac{\partial^2 u}{\partial x^2} + \frac{\partial^2 u}{\partial y^2} + \frac{\partial^2 u}{\partial z^2}\right) - \left(\frac{\partial(\rho u^2)}{\partial x} + \frac{\partial(\rho uv)}{\partial y} + \frac{\partial(\rho uw)}{\partial z}\right)$$

where the y-component (v) and z-component (w) velocities are assumed to be zero, ρ is the density (kg m^{-3}), P is the pressure, and μ is viscosity (kg m^{-1} s^{-1}). An attempt was made to solve the flow field numerically using the continuity equation and all three momentum equations by using finite difference and the semi-implicit-pressure-linked-equations (SIMPLE) method (FORTRAN code given in Appendix E) but this effort was not fruitful for reasons likely due to improper implementation of the pressure boundary conditions. Instead, the exact solution for 2D flow in a rectangular duct with no slip boundary conditions at the walls was used to find values of u as a function of y and z, assuming no entrance effects, *i.e.* $(\partial u/\partial x) = 0$. The solution to Equation 5.2 with these assumptions, $u(y,z)$, is the classical Poisseuille flow problem and is given as Equation 5.3 with boundary conditions of $u(-h/2,-w/2) = u(-h/2,w/2) = u(h/2,-w/2) = u(h/2,w/2) = 0.0$ where h is the flow cell height in the y-direction and w is the flow cell width in the z-direction.

Equation 5.3

$$u(y,z) = \frac{\Delta P h^2}{8\mu L}\left(1 - \frac{4y^2}{h^2} - \sum_{n=0}^{\infty} \frac{32(-1)^n \cosh\left(\frac{(2n+1)\pi z}{h}\right)\cos\left(\frac{(2n+1)\pi y}{h}\right)}{(2n+1)^3\pi^3 \cosh\left(\frac{(2n+1)\pi w}{2h}\right)}\right)$$

ΔP was determined from the given volumetric flow rate, Q, (3.33×10^{-6} m^3 s^{-1}) which was calculated by integrating Equation 5.3 across the flow cell width and height and is given in Equation 5.4. The solution to Equation 5.3 is given in Figure 5.4.

Equation 5.4

$$Q = -\frac{\Delta P w h^3}{12\mu}\left(1 - \sum_{n=0}^{\infty} \frac{192}{\pi^5}\frac{h}{w}\frac{1}{(2n+1)^5}\tanh\left((2n+1)\pi\frac{w}{2h}\right)\right)$$

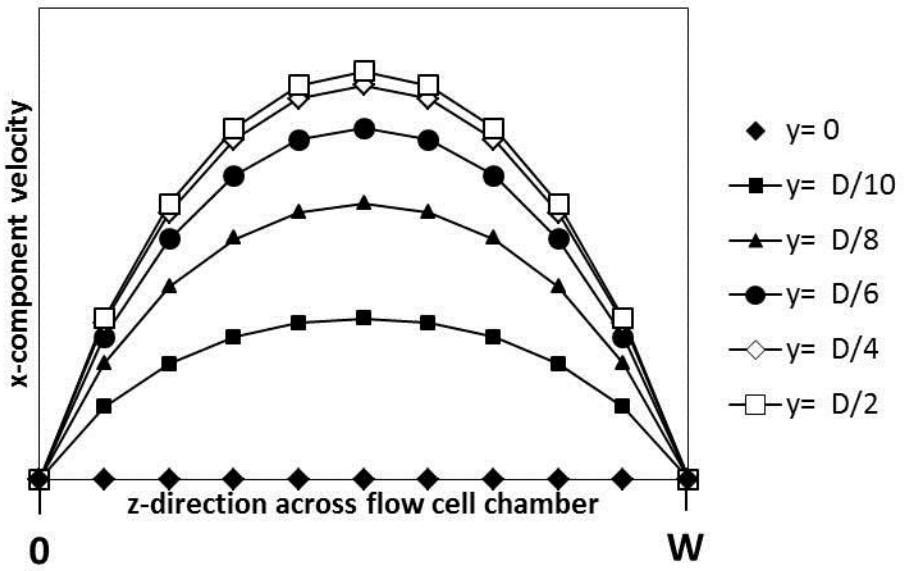

Figure 5.4. Two dimensional Poisseuille flow in a rectangular channel.

Since the fluid is assumed incompressible (constant density/viscosity) the flow field, $u(y,z)$ can be decoupled from the energy equation and solved separately; once

known, the velocity field does not change as a function of time and is fed directly to the energy equation at every time step during the numerical solution procedure.

To solve Equation 5.1 numerically, this equation was finite differenced and marched forward in time. The time derivative on the left hand side of Equation 5.1 was forward differenced with first order accuracy; the spatial derivatives on the right hand side were center differenced with second order accuracy as given in Equation 5.5. This equation was solved explicitly for T by marching forward in time where T^{n+1} is the temperature to be solved at the current time step using the T^n field from the previous time step.

Equation 5.5

$$T_{i,j,k}^{n+1} = T_{i,j,k}^{n} + \Delta t \left(\alpha_{i,j,k} \left(\frac{T_{i+1,j,k}^{n} - 2T_{i,j,k}^{n} + T_{i-1,j,k}^{n}}{(\Delta x)^2} + \frac{T_{i,j+1,k}^{n} - 2T_{i,j,k}^{n} + T_{i,j-1,k}^{n}}{(\Delta y)^2} + \frac{T_{i,j,k+1}^{n} - 2T_{i,j,k}^{n} + T_{ij,k-1}^{n}}{(\Delta z)^2} \right) - \left(\frac{T_{i+1,j,k}^{n} u_{i+1,j,k} - T_{i-1,j,k}^{n} u_{i-1,j,k}}{2\Delta x} \right) \right)$$

where $\alpha_{i,j,k}$ is the thermal diffusivity and varies spatially depending on the material represented at a particular node. The parameter values used here for a given material are tabulated in Table 5.1.

Table 5.1. Material properties used in model.

Material	density (kg m^{-3})	heat capacity (J kg^{-1} °C^{-1})	thermal conductivity (W m^{-1} °C^{-1})	thermal diffusivity (m^2 s^{-1})
Air	1.18	1007	0.03	2.17E-05
PMMA Wall	-	-	-	1.30E-08
PVA tissue mimic	1028	3970	0.58	1.42E-07
Water fluid mimic	998	4180	0.60	1.44E-07

5.3.2 Computational grid and boundary conditions

Equation 5.5 was solved on the computational grid shown in Figure 5.5 which includes the rectangular flow chamber surrounded by PMMA walls and insulating air. The length of the flow chamber in the model was 7.62 cm which is equal to the entire length of the heating element used in the experimental heat transfer measurements. The wall thickness was set to 0.318 cm with 1.27 cm of air surrounding the flow cell in the *y*- and *z*-directions. For all modeled scenarios, the boundary conditions at the air's edge (i=1, i=imax, j=1, j=jmax, k=1, k=kmax) was kept constant at the initial temperature value (typically room temperature or 37 °C). All other boundary conditions specific to the three modeled scenarios are described in their respective sections.

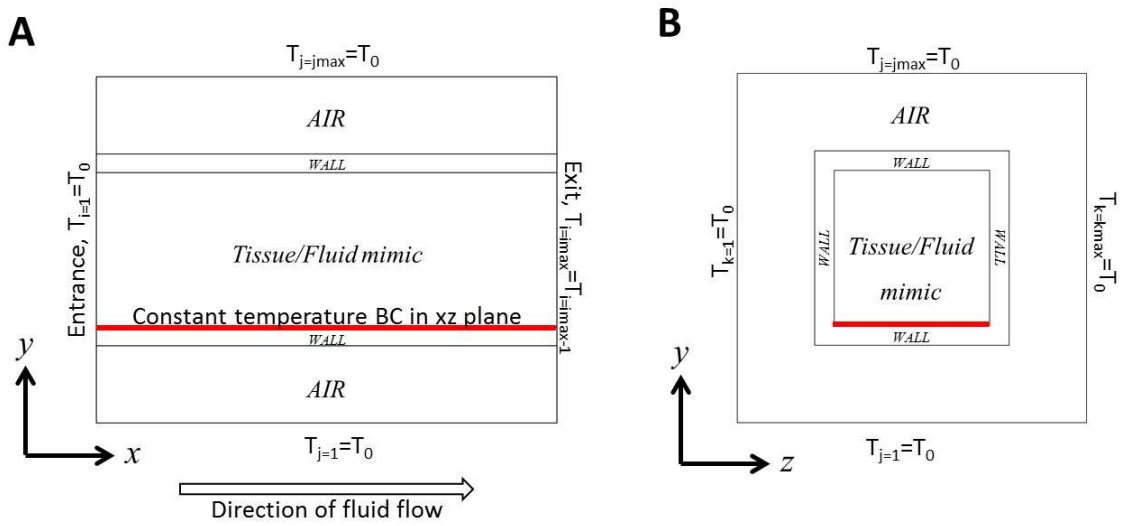

Figure 5.5. Computational grid and boundary conditions. A) Cross section of grid in *xy*-plane showing direction of fluid flow, temperature boundary condition located flow cell floor, and surrounded by air. B) Cross section of flow cell in *yz*-plane with same temperature boundary condition spanning at the *z*-direction at the flow cell floor.

5.3.3 Model consistency

Since the model uses an explicit scheme to solve the temperature field, the stability of the model is dictated by the time step, the flow rate, and the spacing between nodes (Δx, Δy, and Δz); too large of a time step or node size will cause the model to destabilize and compute a nonsensical temperature field. To check for model consistency, the time step and node size was decreased for both the conduction-only model and the convection-only model, separately. The largest Δt used was 0.01 and 0.005 s for the conduction scenario and convection scenario, respectively, further decreasing these values did not result in any change in the computed result as shown in Figure 5.6A and C. Likewise, reducing the node size beyond 0.000635 m did not result in any significant change to the computed result (shown in Figure 5.6B and D).

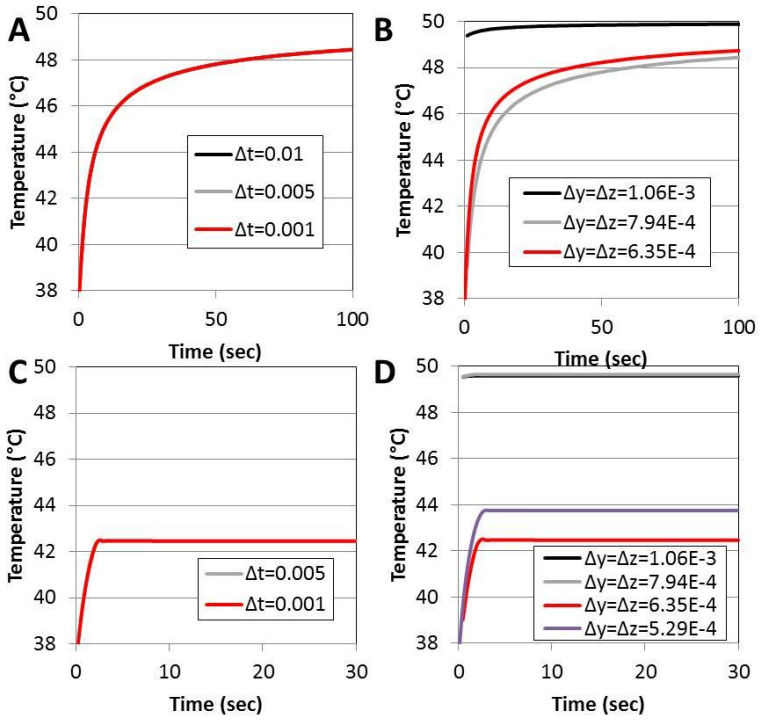

Figure 5.6. Model consistency. Model was checked for unstable conditions by decreasing Δt and the grid size, Δy, for the conduction only-model (A and B) and the convection only mode (C and D). Δt less than 0.01 s computed the same result as evidence that all curves lie on top of each other; Δy less than 6.35E-4 m did not compute any significant change in the modeled result.

5.4 One dimensional conduction

5.4.1 Experimental results

Experimental heat conduction through the PVA tissue mimic (Scenario 1) was performed by keeping the boundary condition at the bottom of the mimic/flow cell floor (*xz*-plane at red line shown in Figure 5.5 in the computational model) constant at the same temperature throughout the trial. Since this temperature boundary condition is implemented via a PID feedback-controlled heating element, this temperature cannot be applied instantaneously as in the computational model. An approximately 30 s time lag is needed to bring the boundary condition up to the specified temperature, with some overshoot initially as shown for a 50 °C boundary condition in Figure 5.7. The error bars in this figure are from averaging 6 temperature probes placed at the same distance, *y*, away from the heating element but at different locations, *x*, in the flow cell wall arrays as described in Section 5.2.2. This scenario was repeated for tissue mimics starting at T = 24 °C and boundary conditions equal to 37, 50, 60, 70, and 80 °C. The 37 °C boundary condition has no significance except that is shows the approximate resulting hyperthermia from a 13 °C temperature rise. A 37 °C boundary condition applied in the body would not produce any tissue damage since this is the normal *in vivo* body temperature.

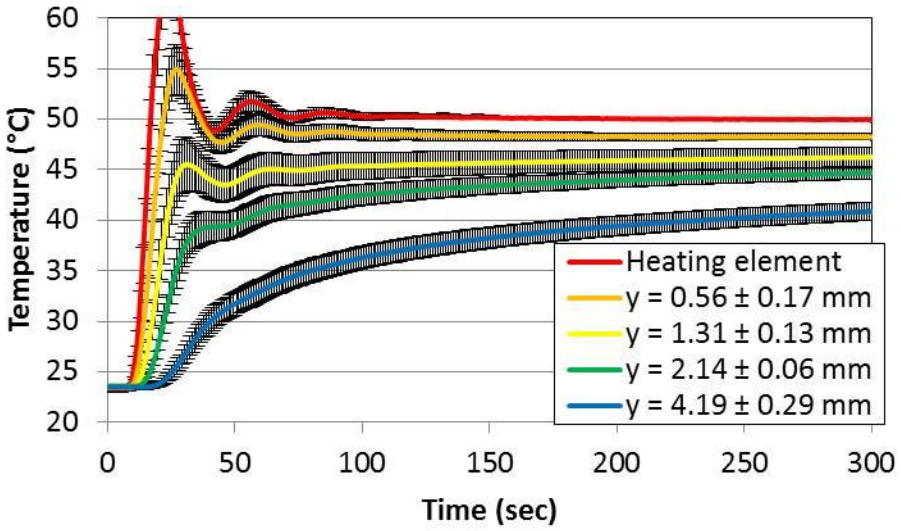

Figure 5.7. Conductive heat transfer in tissue mimic. Transient temperature measurements from probes spaced laterally away from the heating element; boundary condition at T = 50 °C. Error bars represent average from six probes placed at the same distance, y, but at different arrays in the flow cell walls.

5.4.2 Model prediction of isotherms

The experimental transient heat transfer data were used to produce 10 °C temperature-rise isotherms for each temperature boundary condition and are shown in Figure 5.8. This figure plots the amount of time (y-axis in Figure 5.8) a location at a specific distance away from the heating element (x-axis in Figure 5.8) took to increase 10 °C. This is a good indicator of when cell death in biological tissue maybe begin to occur since tissue necrosis is commonly reported at 44 to 47 °C.[91] For the 80 °C boundary condition, this means up to 4-5 mm of tissue will experience a temperature rise of 10 °C—and potentially be damaged—in less than 60 sec.

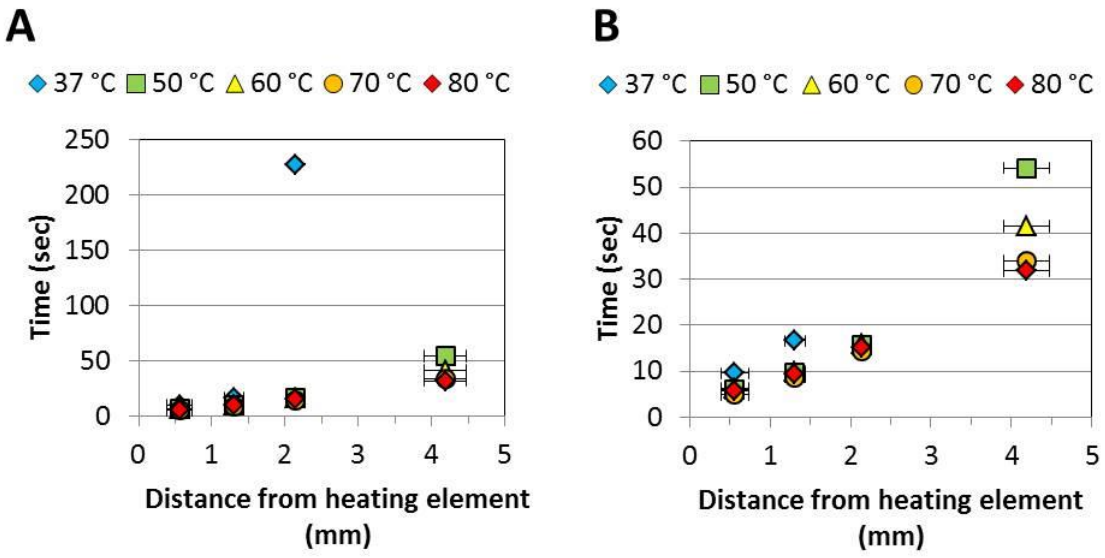

Figure 5.8. Experimental isotherms in tissue mimic representing the time it took each probe to rise 10 °C (*y*-axis) as a function of its distance away from the temperature boundary condition (*x*-axis); right plot is the left plot with *y*-axis scaled down.

Comparison of the transient experimental results from the flow cell/tissue mimic to the computational model is shown in Figure 5.9 for a 50 °C boundary condition. Distances in the *y*-direction for obtaining temperature profiles from the model were chosen that corresponded to the same probe locations in the flow-cell wall. The model was implemented using the FORTRAN code given in Appendix A. Periodic boundary conditions were implemented at $i = 1$ and $i = imax$ (the maximum number of nodes in the *x*-direction and the location at $x = L = 7.62$ cm). Initially, during the first minute of heating, the model and experimental results do not agree strongly. This is expected due to the large power dump provided by the heating element and the time required by the experimental conditions to reach the temperature boundary condition. These conditions more accurately reflect how a surface would actually be heated inside the body. As both the model and the experimental conditions reach an approximate steady state, they are within 1 °C of agreement.

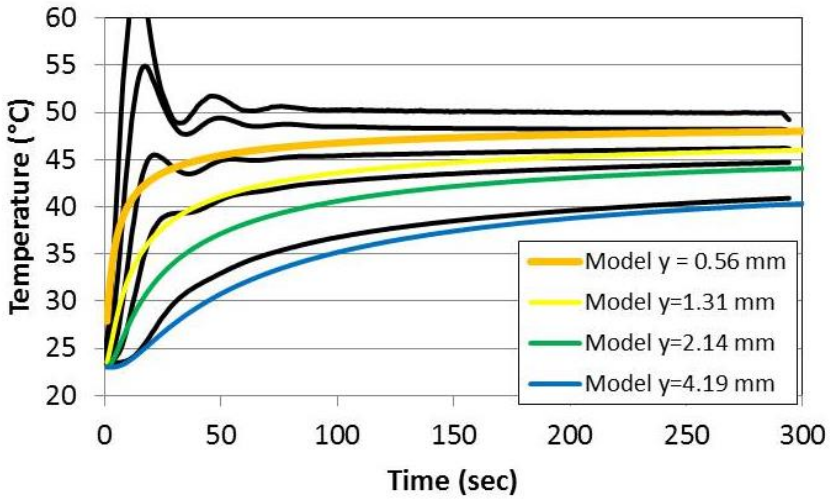

Figure 5.9. Conduction heat transfer model. Comparison of computed model result (represented by colored lines) to the experimental transient temperature profiles (black lines) at the same position away from the 50 ºC boundary condition; top black line is the curve for the probe placed at the heating element surface.

The results from the model were used to produce 10 °C isotherms and were compared with the experimental results as shown in Figure 5.10. The model predicts faster heat transfer for the more extreme 80 °C case; the 50 °C case is within the error of the experimental measurements. Deviations from the model are likely due to slight deviations of the thermistor probe heads from their presumed locations in the tissue mimic.

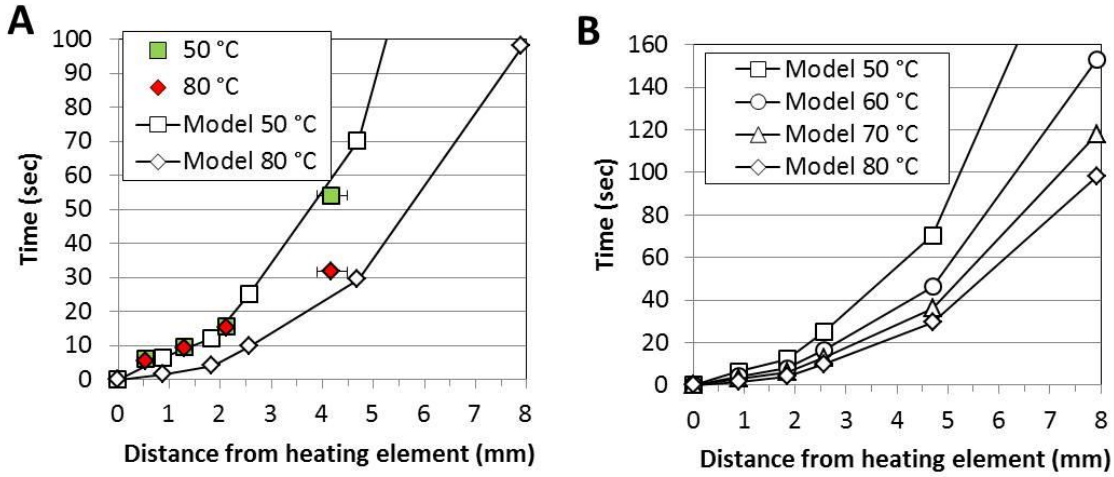

Figure 5.10. Predicted isotherms in tissue mimic. A) Comparison of experimental 10 °C isotherms from Figure 5.8 with computed isotherms at 50 and 80 °C. B) Computed isotherms spanning 50 to 80 °C boundary conditions.

5.5 Two dimensional forced convection

The same temperature boundary conditions used in Scenario 1 were also used in Scenario 2: energy transport through a water fluid mimic due to forced convection by the fluid moving at 0.2 L min^{-1}. The transient results from these experiments are given in Figure 5.11 for a 50 °C boundary condition which shows a steady state temperature profile is achieved in less than 30 sec due the large heat sink conditions, with temperatures only rising above their initial conditions within the first 2 mm of fluid.

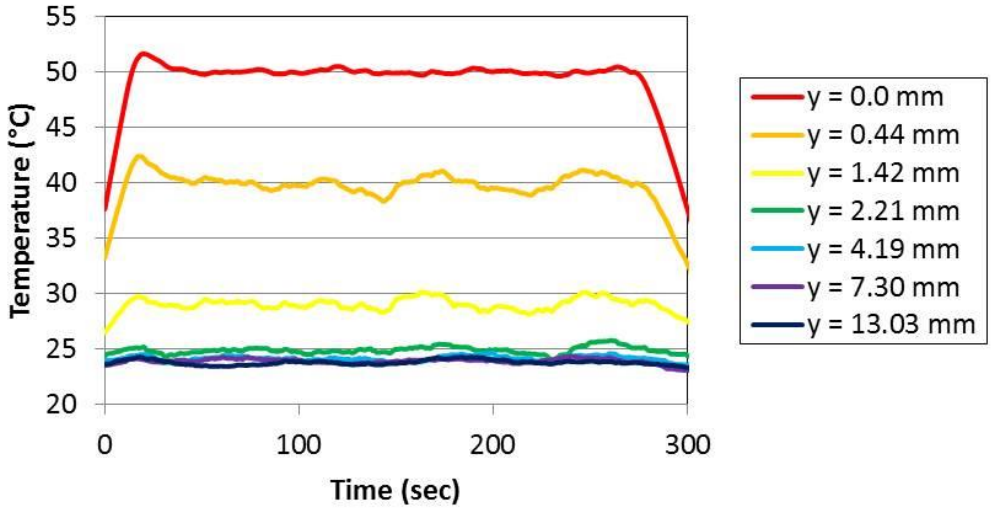

Figure 5.11. Convective heat transfer in fluid mimic. Experimental transient temperature profiles with water flowing over 50 °C boundary condition at 0.2 L min^{-1} showing steady temperature profiles and less than 2 mm of heating in the fluid mimic.

This scenario was repeated for boundary conditions equal to 37 and 60 °C. The temperature rise for the embedded thermistors is plotted in Figure 5.12 as a function of their distance away from the heating element/temperature boundary condition which shows large temperature gradients near the heating element's surface, as expected. This fact, combined with the slight error in the thermistor probes' placement in the *y*-direction (less than 0.5 mm) generates large errors for the measurement of this gradient near the heating element surface as indicated by the error bars in Figure 5.12. These error bars

represent averages taken from four thermistors positioned at the same distance away from the heating element but at different positions along the length of the heating element. Nonetheless, the temperature gradient near the wall/boundary condition is predicted by the energy equation and is compared with the computational model as shown in Figure 5.13 which also gives profiles for a 70 and 80 °C boundary condition; the modeled results are with the error of the experimental results. The FORTRAN code for the convective-dominated scenario is given in Appendix B.

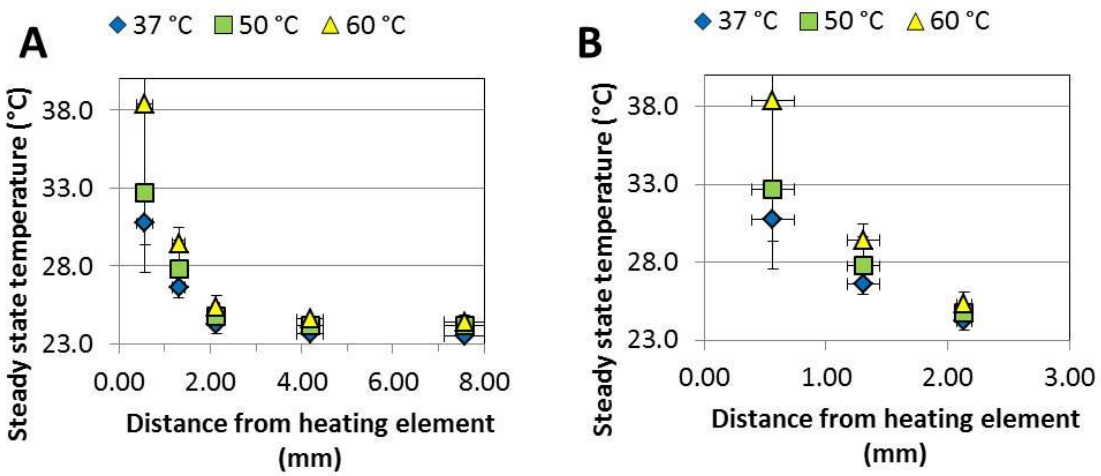

Figure 5.12. Convective heat transfer vs. boundary condition. Steady temperatures from experimental flow cell measurements with water at 0.2 L min^{-1} as a function of distance away from the heating element for temperature boundary conditions at 37, 50, and 60 °C. Right plot is same as left plot with scaled down *x*-axis.

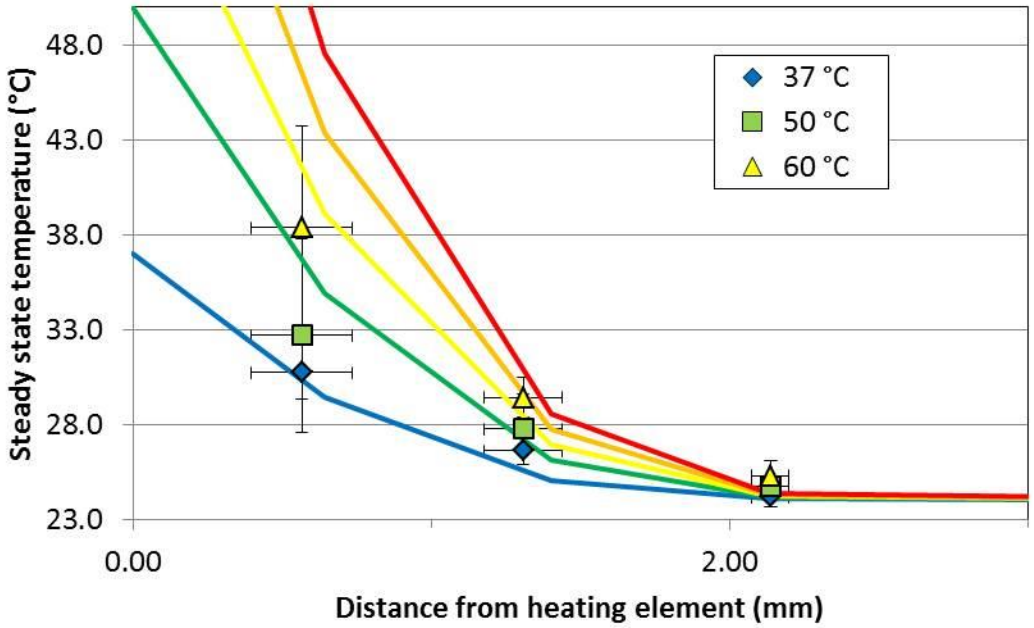

Figure 5.13. Predicted convective heat transfer. Experimental steady temperatures from Figure 5.12 compared with computed steady temperatures from model as a function of distance away from the boundary condition at 37 °C (blue line), 50 °C (green line), 60 °C (yellow line), 70 °C (orange line), and 80 °C (red line).

The experimental fluid flow conditions provided by the pump were only able to obtain a flow rate of 0.2 L min^{-1} which corresponds to a Reynolds number of 147 assuming a square duct (Re = $\rho \boldsymbol{u} D_h / \mu$ where u is the maximum velocity and D_h is the hydraulic radius which is equivalent to the flow cell width/height). Since the Re of blood flowing through the aorta can be as high as 10,000, the computational model was used to predict the power requirements to heat a surface for these flow conditions with Re = 147, 1000, 1465, and 10,000 for temperatures at 50, 60 and 70 °C; the results are given in Figure 5.14. The power, q, (in W cm^{-2}) was calculated from the modeled temperature field by applying Fourier's law of heat conduction at the boundary condition in the y-direction and using the second order one-sided difference given in Equation 5.6 where k is the thermal conductivity (W m^{-1} $°C^{-1}$)

Equation 5.6

$$q_{i,j,k} = -k_{i,j,k}\frac{-3T_{i,j,k} + 4T_{i,j+1,k} - T_{i,j+2,k}}{2\Delta y}$$

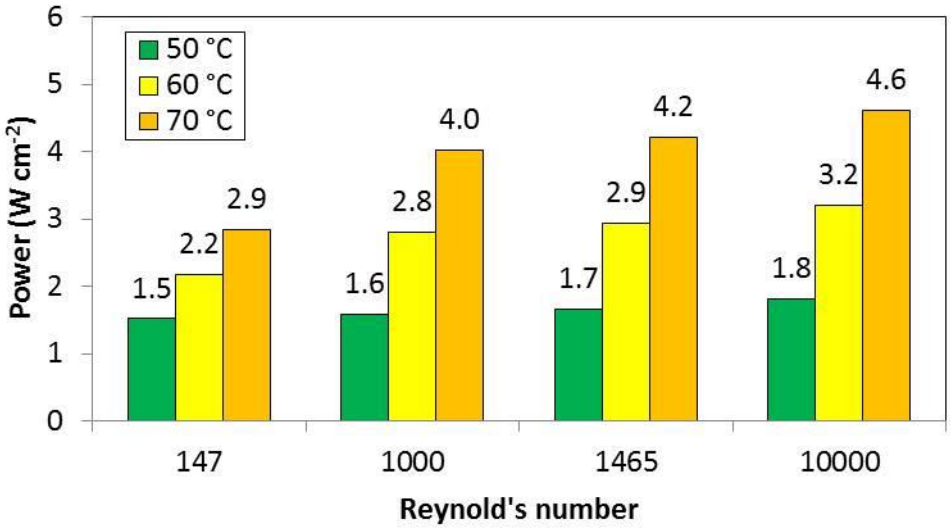

Figure 5.14. Power requirements vs. Reynold's number. Computed steady heat flux across boundary condition in *y*-direction for the convection-driven model as a function of Reynold's number and boundary temperature.

The power needed to heat the surface to the same temperature under flow conditions with Re = 10,000 compared to Re = 147 is nearly 1.2 times larger for the 50 °C boundary condition and 1.6 times larger for the 70 °C boundary condition. The results for Re = 10,000 should be taken lightly, however, since the fluid flow at this Re is likely turbulent and the model was built under the assumption of laminar flow. This analysis prompted a comparison between the power calculated from the model and the power delivered by the heating element (calculated by multiplying the current and voltage delivered to the heating element at steady state and dividing by the heating element's surface area). This comparison is given in Table 5.2 which shows the heating element's power and the power predicted by the model differ by a factor of 1.35 for the hotter temperature boundary conditions, which is expected since some of the energy provided

by the heating element is propagated through the flow cell floor. This ratio can be used to compare the power predicted by the model to the power delivered by the heating element to the SAR/power of the magnetic composite coatings in Chapter 2.

Table 5.2. Model vs. experimental power delivery. $P_{model} \times Ratio = P_{heating\ element}$

Temperature	Power from heating element (W cm^{-2})	Power from model (W cm^{-1})	Ratio
37 °C	0.89 ± 0.07	0.86	1.03
50 °C	2.05 ± 0.15	1.52	1.35
60 °C	2.91 ± 0.18	2.18	1.34

5.6 Three dimensional combined conduction/convection

Lastly, in Scenario 3, a PVA tissue mimic was poured and crosslinked over only half of the heating element in the flow cell with the remainder being subject to the fluid mimic heat sink. The actual portion of the heating element covered by the tissue mimic was 40% of the total flow cell width (1.02 cm) as measured post-trial with a micrometer. As discussed in Chapter 4, a thermistor temperature probe (termed the "driver" probe) is attached directly to the heating element's surface between the nichrome foil and the PDMS protective coating. This probe provides the temperature feedback used by the PID controller to adjust the power delivered by the heating element and, thus, the temperature. In Scenarios 1 and 2, the placement of this probe on the heating element surface was somewhat arbitrary since the entire surface is subject to the same heat sink. In Scenario 3, however, the heat sink varies as a function of *z*, the direction spanning the width of the flow cell/heating element. Since the heat flux delivered by the heating element is uniform, the temperature will rise faster in the tissue mimic side than the fluid mimic side; additionally, the temperature gradient in the *y*-direction will increase as the driver probe is moved closer to the fluid mimic heat sink side. Thus, the position of this driver

probe will dictate the resulting heat transfer measurements in the tissue mimic. For the experimental measurements, the driver probe was placed 0.9 cm from the flow cell wall, or 0.1 cm from the fluid mimic/tissue mimic interface. The resulting transient profile through the tissue mimic side measured by thermistors protruding 6 mm into the tissue mimic from the wall is shown in Figure 5.15A for a 37 °C boundary condition. The temperature rise in the fluid mimic side for this same trial is shown in Figure 5.15B.

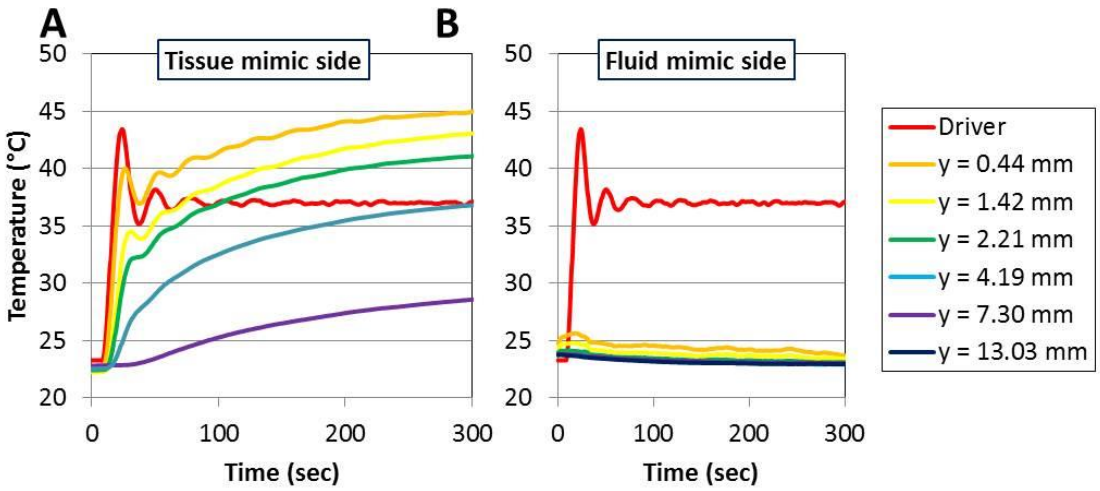

Figure 5.15. Side-by-side convective, conductive heat transfer. Transient, experimental temperature profiles for heat transfer through a PVA tissue mimic (A) and a water fluid mimic at 0.2 L min^{-1} (B) both side-by-side and over the same temperature boundary condition at 37 °C.

The model that was built for this scenario matched the placement of the driver probe relative to the distance away from the wall in the tissue mimic side. To implement this same, constant heat flux boundary condition in the model, the temperature for a single row of nodes in the x-direction at the *xz* heating element plane was specified. The heat flux for a node at the center of this row of nodes (i.e. at $x = imax/2 = L/2$) was calculated in the *y*-direction using Equation 5.6. This q was then used to calculate the temperature T at all other nodes in the same *xz* plane by rearranging Equation 5.6 for $T_{i,j,k,}$ thus imposing the same heat flux throughout the entire boundary condition. The

FORTRAN code for this scenario and constant heat flux boundary condition is given in Appendix C. The resulting transient temperature profile in the tissue mimic side is given in Figure 5.16A, next to the experimental results from Figure 5.15A for the same distances away from the heating element/boundary condition.

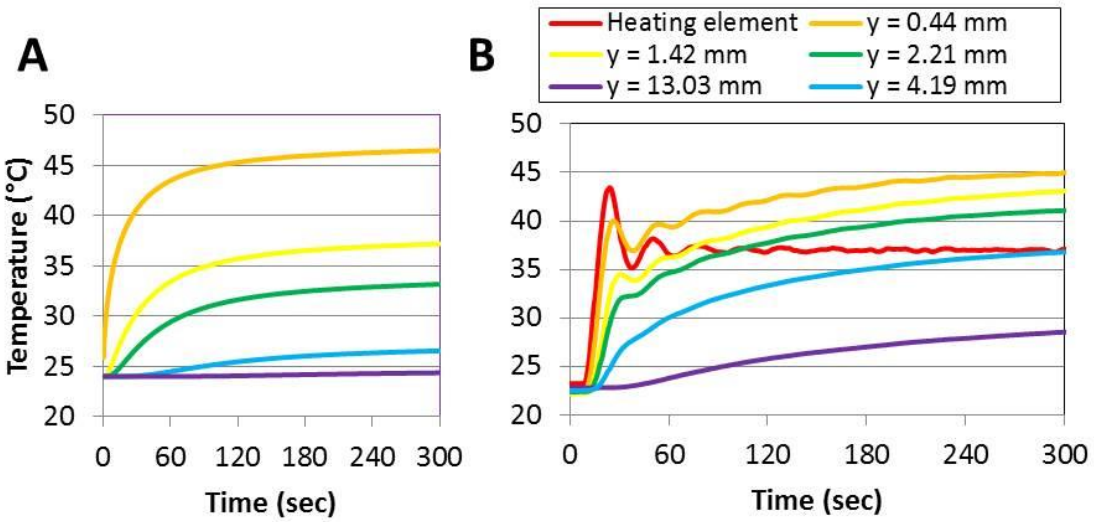

Figure 5.16. Predicted heat transfer in side-by-side scenario. Experimental temperature profiles through side-by-side tissue mimic in Figure 5.15 (right) compared with computed solution (left) for boundary condition at 37 °C.

It is immediately obvious that the temperature profiles predicted by the model are in strong disagreement with the experimental results. The shape of the temperature curves, however, is the same which instills confidence that the math and the boundary conditions were implemented correctly in the model. The discrepancy is likely due to the compounded error induced by having to specify more parameters in an additional dimension compared to the previous two scenarios. For example, the placement of the driver probe in the model relative to the fluid mimic/tissue mimic interface is a likely large source of error. To observe how the heat flux changes as a function of placement of the driver probe in the *z*-direction on the heating element surface—and thus the resulting heat transfer—temperature contour plots in the *yz* plane at $x = L/2$ were produced for five

different placements of this probe and are given in Figure 5.17 after 5 min of heating. The placement of the driver probe in this figure is represented by a white dot. The resulting power calculated at the boundary condition is also given in this figure which shows increasing power as the driver probe moves from the tissue mimic side of the model to the fluid mimic side. Most notably, however, are the temperature gradients that develop in the tissue mimic side as the driver probe is placed further into the fluid mimic side. When the driver is placed 8 mm into the fluid mimic side (Figure 5.17D), the excess power required to maintain this boundary condition causes temperatures to rise as high as 139 °C in the tissue mimic side. In practice, these extremes would not be tolerated— or feasible—but the outcome highlights the danger of not predicting how these hyperthermia scenarios will develop in the body for a given geometry of varying heat sinks.

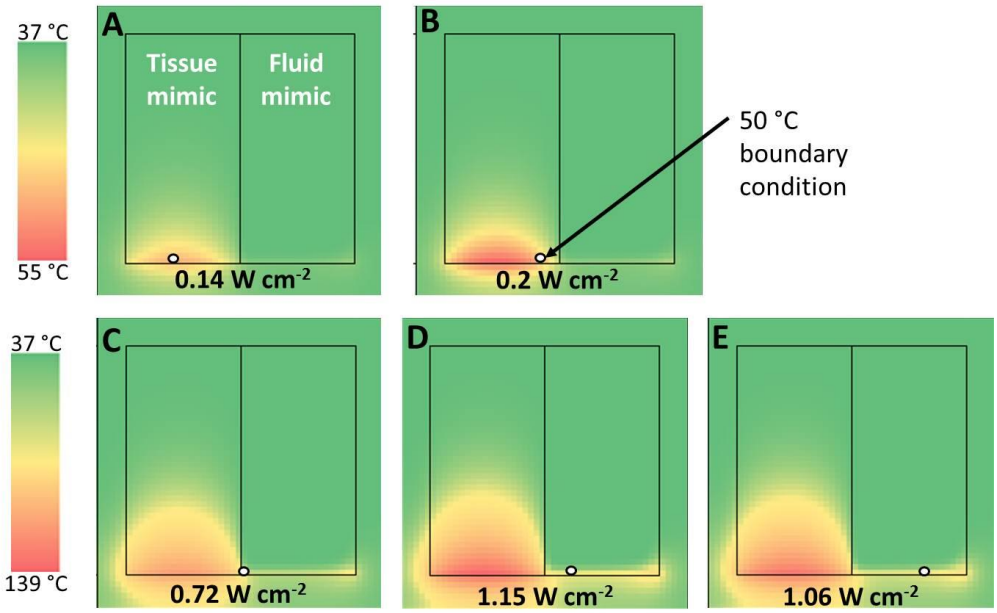

Figure 5.17. Moving boundary condition in side-by-side scenario. Computed temperature contour plots after 5 min of heating showing heat transfer through PVA tissue mimic next to water fluid mimic (fluid moving into the plane of the page) with constant, 50 °C boundary condition applied at different positions in the z-direction (represented by white dot and referred to as "driver" probe) showing decreased heat flux across boundary line as the driver probe moves from the more extreme, convective heat sink side to the tissue mimic heat sink side. Scale bar for A and B is on top and on bottom for C, D, and E.

5.7 Power requirements predicted by model

The data in Figure 5.17 suggest a power gradient across the heating element surface is necessary in order to deliver the same temperature boundary condition under both heat sinks. To quantify this gradient, the same model was used to specify a constant temperature boundary condition at the heating element plane (FORTRAN code given in Appendix D) and the resulting heat flux as a function of z was calculated using Equation 5.6. A contour plot of the resulting temperature field in the yz plane at $x = L/2$ is given in Figure 5.18.

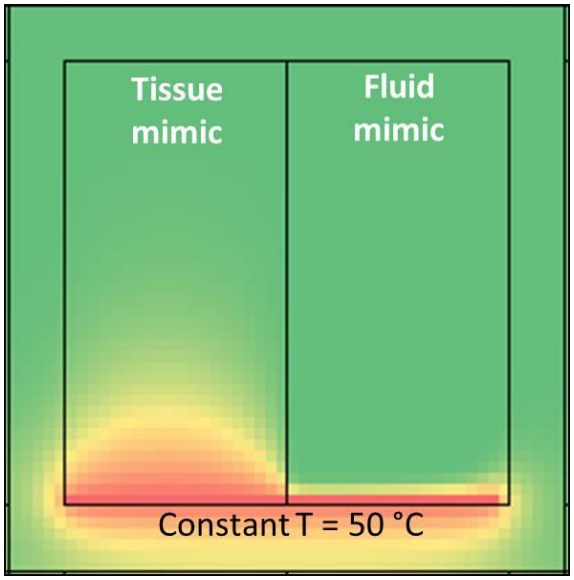

Figure 5.18. Side-by-side scenario: constant temperature boundary condition. Computed temperature contour plots showing heat transfer through PVA tissue mimic next to water fluid mimic (fluid moving into the plane of the page) with constant, 50 °C boundary condition across entire boundary.

This constant temperature boundary condition for scenario 3 was modeled for temperatures at 50 and 70 °C and for Re at 195 and 1953. Curves representing q as a function of z for all four of these scenarios are plotted in Figure 5.19. Under the most extreme conditions (Re = 1953), the fluid mimic side requires nearly 4.4 W cm^{-2} to keep the heated surface at 70 °C while the tissue mimic side on the same surface requires less than 0.3 W cm^{-2}. Thus, when designing a magnetite composite to implement this power

gradient on a surface to be heated inside the body, the power would need to decrease by almost a factor of 15 over a distance of less than 1 to 2 mm.

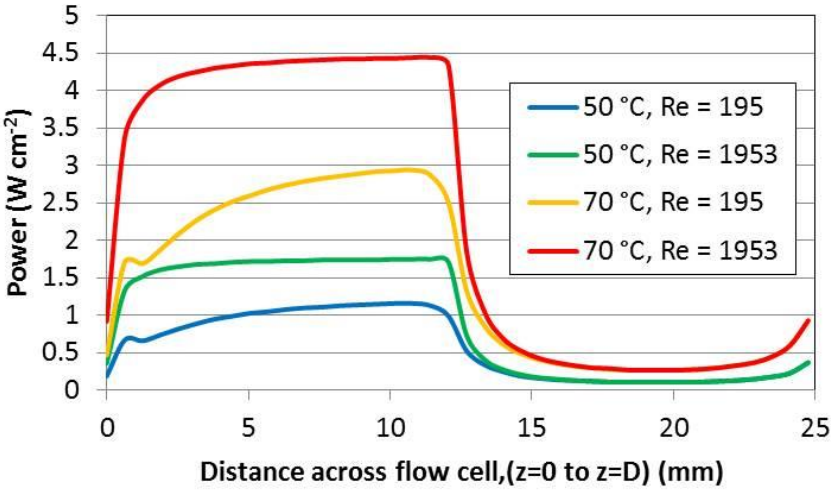

Figure 5.19. Power profiles across a constant temperature boundary condition. Computed heat flux at constant temperature boundary condition as a function of the distance across the flow cell in the *z*-direction for 50 and 70 °C boundary conditions for fluid side flowing at Re = 195 and 1953 showing up to a factor of 15 decrease in heat flux on the tissue mimic side compared to the fluid mimic side.

5.8 Conclusions

A numerical model was built that computed the heat transfer across a boundary condition covered by two different heat sinks. This model demonstrated how dramatically different power loadings will be required on the same surface in order to avoid heating solid tissue to dangerous temperatures while ensuring surfaces exposed to extreme blood flow maintain their target temperature. These findings were validated with temperature measurements in tissue phantoms using the hydrogels developed in Chapter 4 and a 3D-printed heat transfer station. The computational code developed here can be expanded to accommodate complex geometries and other source terms that would affect the transfer of energy in biological tissues such as cellular metabolism and blood perfusion.

CHAPTER 6: CONCLUSIONS AND FUTURE WORK

6.1 Iron oxide nanoparticle composites

Magnetite suspensions have been administered for decades to ablate tumors in cancer patients, prompting a substantial body of research on biocompatibility and SAR optimization in fluid systems where large particle loadings *in situ* are challenging. The power density for the remote biofilm mitigation application proposed here requires loading magnetite/polymer coatings with particle concentrations orders of magnitude greater than in most previous studies. While such loadings are easily accessible in the proposed composite coating, the increased potential for particle-particle interactions and aggregation within a solid heterogeneous composite of defined geometry makes the design of such coatings much less straightforward. This dissertation has demonstrated the orientation of the coating with regard to the field lines of the AMF has a strong impact on the observed SAR. This finding is particularly important as it implies that simply coating a three-dimensional device with a uniform film will not result in uniform heat generation, let alone uniform temperature, even within a uniform AMF. Each coating surface must be designed based not only on the adjacent heat-sink conditions, but also on any adjacent magnetically-susceptible material and its position relative to the applied AMF. Increasing the power density at any specific location, however, requires only that the total iron loading be scaled proportionally. The composite matrix, though not itself magnetically susceptible, still influences the observed SAR, due primarily to its degree of swelling and the degree to which particles can be evenly distributed at large (2-10% v/v) concentrations. Subsequent improvements in theoretical design of these coatings will

require more extensive experimental investigation on the dispersion of MNPs at large concentrations in polymers approved for medical use.

6.1.1 Magnetic shielding effect

Additional experiments can be designed that could test the magnetic shielding hypothesis observed here for the parallel verses perpendicularly placed composites. For example, placing the composites at a 45° angle in the magnetic field should produce heating rates that fall somewhere between their perpendicular and parallel value. Alternatively, intentionally placing a layer of magnetic material between the field source and the composite sample should induce magnetic shielding, and thus decrease SAR, though the thickness of this material would presumably have to be quite large to produce any effect which could result in significant heat conduction into the sample chamber that would drown out any attempted measurement.

The slight trend in decreasing SAR as a function of iron concentration—though not statistically significant—suggests increasing concentration would increase the amount of magnetic shielding potential, particularly in the perpendicular position. A wider range of iron concentration (beyond 40 wt% Fe) should be investigated to see if this trend actually exists as a function of iron concentration, which would further support the shielding hypothesis.

6.1.2 Iron oxide longevity

In Chapter 2, a larger SAR was observed for the composite films produced and tested at the beginning of the study compared to their SAR measured 18 months later. This result could be due to particle oxidation and subsequent reduction in their magnetic

susceptibility. Future oxidation measurements that can more accurately measure the iron stoichiometry (mol of Fe^{2+} to Fe^{3+}) in the aged polymer composite than the spectrophotometric or x-ray diffraction methods used here could quantitatively support this correlation; Mössbauer spectroscopy is an example approach. However, the difference in magnetization saturation (84 emu g^{-1} for magnetite and 74 emu g^{-1} for maghemite) between Fe_3O_4 and Fe_2O_3 alone does not fully account for the 60% drop in SAR for the PS composites. SEM analysis of the aged composites would reveal if the particle size and shape has changed over time which would suggest further oxidation to another form of iron oxide—such as goethite which is an iron oxyhydroxide and not superparamagnetic. Another possibility for the decrease in SAR is loss of iron content during storage, though this seems unlikely since the samples were stored in protective zip-top bags; a measure in the total iron content of the aged samples would prove any loss in iron mass.

6.1.3 SAR measurement

On a final note, the author would like to highlight the degree of rigor that was used to achieve the SAR measurements reported in this dissertation. At the beginning of this thesis work, a review of the subject revealed very poor repeatability—and consequently large variability—between SAR measurements for iron oxide nanoparticle systems reported throughout the literature. Many publications use experimental apparatus that are inherently bad at acquiring repeatable data. These systems seldom included the variability of the alternating magnetic field strength used for heating the magnetic material; were not designed to reduce heat transfer out of or in to the system; or did not

use more than one temperature probe for measuring the temperature rise of the heated medium.

The system used here for acquiring SAR data not only quantified the magnetic field strength with an independent instrument, but demonstrated this field did not vary to any large degree throughout the volume used for heating the sample. Custom designed foam containers were used to reduce heat loss/gain into the heating chamber in addition to using measurements from iron-free controls that were subtracted from all temperature rise data to correct for heat gains from the induction coil. Multiple temperature probes placed throughout the entire sample chamber volume showed the temperature rise of the heated solvent was uniform and constant. The redundancy provided by the multiple probes combined with a weighted heat capacity and stringent iron concentration measurements of the heated samples all resulted in more reliable and repeatable SAR values.

6.2 Wireless, thermal biofilm deactivation

Prior to the heat shock studies of *P. aeruginosa* biofilms using a temperature controlled water bath reported by work in the same laboratory (Ref. 27), cell death in biofilms (which are more resilient than their planktonic phenotype) had not been reported as a function of exposure temperature and time at medically accessible temperatures below 100 °C. The work reported here and by Ricker *et al.* in Ref. 81 demonstrated for the first time the degree of cell death for these same biofilms but treated instead with heat delivered wirelessly using an iron oxide nanoparticle/polymer composite. The most obvious challenge that resulted from this study was obtaining a uniform temperature gradient across the entire 2.5 by 3.75 cm composite surface used for heating the biofilm.

These temperature gradients were attributed to variations in the strength of the alternating magnetic field. Once the non-uniform magnetic field was accounted for, biofilm cell death as a function of time and temperature demonstrated the same degree of deactivation as in the water bath heat shock trials. Biofilms colonies did not demonstrate any degree of cell death greater than one order of magnitude for heat shock temperatures less than 60 °C at times less than 5 min. This finding suggests large temperature rises on the implant surface may be needed to incorporate this wireless hyperthermia treatment strategy effectively. Future work will demonstrate the effect of multiple pulses of low temperature gradients on biofilm viability and compare them to the more extreme, sustained heat shocks.

6.2.1 Biofilm heat shock with shear stress

Once a biofilm has been established on a surface, some of the bacteria will revert to their planktonic phenotype and begin to detach and expand to other surfaces as depicted in Figure 1.1. Cell detachment may be enhanced under stresses such as heat shock suggesting bacteria may begin to "flee' from the biofilm environment to seek a more favorable, lower temperature environment. This effect could be studied by heat shocking biofilms grown under the constant shear stress of a fluid flowing over their surface. Thus, future biofilm thermal deactivation studies will include experiments that expose the biofilms to shear stress via culture media flowing over the top of the biofilm. The amount of shear stress (flow rate) will be controlled to determine the maximum amount of shear the biofilms can withstand without cells detaching under normal growing conditions at 37 °C. Cell detachment will be quantified by enumerating the amount of bacteria in the effluent. The effluent sample rate will need to be controlled in order to

enumerate the bacteria in a quantifiable range (*i.e.* too large of a sample volume will dilute the bacteria concentration below quantifiable levels). Once a shear rate has been established that does not cause cultured biofilms to delaminate of flee, the biofilms will undergo heat shock at the same time and temperatures explored in the previous heat shock studies, though shorter time lengths may be required to conserve on the total volume of medium needed for a complete trial. These heat shock trials with shear can be accommodated with the heat transfer station used in Chapter 5 in which the thermal shock will be implanted with the electrical resistance heating element and feedback control. After heat shock, the amount of bacteria quantified in the effluent samples will be compared with the amount of living bacteria remaining on the heat shocked microscope slide. Results that indicate a difference will suggest biofilm bacteria can respond to thermal stress by fleeing their biofilm environment which may complicate future design of an effective wireless thermal treatment for infections occurring on devices next to blood flow.

6.2.2 In vivo, wireless thermal shock

Studies that would re-incubate the biofilms after they have been thermally deactivated on microscope slides would provide some context into the resilience of these colonies to heat shock. However, more appropriate results would be obtained from trials using mice as this would more directly mimic the biofilm growth conditions inside a human. This study would likely require biofilms to be grown on composite coupons roughly 12 mm in diameter that would then be subcutaneously implanted near the back of the mouse. Initial trials would explant the coupon without any heat shock to first quantify the degree to which biofilms will grow when subject to an *in vivo* growth environment,

which is largely unknown. Second, these explanted biofilms/coupons will be heat shocked *ex vivo* to see if this same growth environment affects the biofilm's thermal susceptibility. Next, wireless heating of the coupons *in* vivo would require a temperature probe to be inserted into the mouse near the coupon's surface to implement PID feedback control, all while positioning the mouse and implanted coupon parallel to magnetic field lines in a uniform AMF large enough to accommodate the rodent subject and temperature probe. Coupons that were heat shocked *in vivo* would be explanted and bacteria viability would be enumerated. Future experiments would leave the coupon in the mouse post heat shock to see if the animal recovered from the infection. These trials would use both wild-type mice and neutropenic (immune compromised) mice to observe the effect of the immune system on biofilm mitigation and animal recovery. In all scenarios, histology on the tissue surrounding the coupon tissue would be performed to determine the degree of tissue damage.

6.3 Tissue phantoms

A variety of materials are currently used as tissue phantoms, each with an overlapping set of shortcomings such as rapid degradation, poor volume control, poor thermal stability, and inability to mimic physiological thermal properties. By carefully tuning the crosslinker ratio, curing temperature, curing time, and property modifiers, this dissertation demonstrated a synthetic hydrogel tissue phantom which can be poured into any shape, gels in seconds, maintains its original volume for weeks across a large temperature range, and whose thermal properties can be tuned across a wide physiologically-relevant range.

Crosslinker ratio, curing temperature, curing time, and property modifiers were investigated for their effects on the transient and equilibrium swelling ratios of poly(vinyl alcohol) (PVA) monoliths for use as tissue phantoms. The gelation time of PVA solutions mixed with glutaraldehyde at pH 2 decreased logarithmically with temperature, consistent with Arrhenius reaction kinetics. At 22 °C, phantom curing required approximately 3 hours to complete, as indicated by equilibrium swelling ratios for phantoms at a variety of curing times. At 80 °C, phantom curing was complete in less than half a minute, with an equilibrium swelling ratio 10% less than a fully cured 22 °C phantom with the same glutaraldehyde concentration, and with greater temperature-stability. Phantoms prepared at 80 °C shrank by only 5% upon heating from room temperature to 80 °C for 5 hr, while phantoms prepared at 22 °C shrank by 10%. Equilibrium swelling ratios for phantoms at several glutaraldehyde concentrations demonstrated a strong relationship between swelling ratio and crosslinker concentration—consistent with literature reports.

6.3.1 Incorporating blood perfusion

While the PVA hydrogel phantom fabricated here can accommodate a variety of experimental needs and can be tuned to precisely match a wide range of thermal properties, an important feature missing from this phantom is its ability to mimic blood perfusion. Physiologically, heat loss in solid tissue is attributed to blood perfusion arising from blood flow through capillaries (5 to 10 μm) and small blood vessels (50 to 100 μm). Mimicking the size of these small channels is challenging experimentally but not impossible. Three dimensional microfluidic channels have been produced using the "cotton candy method" which creates networks from pH-sensitive, sacrificial shellac

fibers fabricated by melt-spinning the shellac in a cotton candy machine.[92-93] Hydrophilic gelatin solutions are then poured around the spun fiber and gelled in place. Upon submersion in an ammonia bath, the fibers are dissolved and the micro channels created by the fibers are retained. The resulting network has channels with a mean diameter of 17 ± 19 μm and demonstrated fluid diffusion throughout the tissue phantom once connected to a pump.

Interstitial fluid space has also been achieved experimentally with 30 μm, interconnected pores using what is termed the "6S" method. First, polymer beads (typically poly(methyl methacrylate) (PMMA)) are *sieved* to produce a batch of micron scale spheres of uniform size which are *shaken* then *sintered* to produce a closely packed network of thermally fused micro spheres.[94] Monomer solution of 2-hydroxyethyl methacrylate (HEMA) is then poured into the highly organized network to *surround* the spheres which is polymerized and crosslinked in place, thus *solidifying* the aqueous network to form poly(HEMA). Next, the pHEMA/PMMA sphere composite system is submerged in a solvent bath to *solubilize* the PMMA spheres and leave behind a porous network of channels. This process has been performed using both sacrificial spheres and cylinders to mimic the blood perfused nature of tissue.

These methods are intended to design useful artificial tissues which can then be implanted and used for organ replacement and drug delivery, which raises biocompatibility concerns. Using these types of sacrificial systems for the *in vitro* applications explored here for heat transfer, however, may better suit their novelty. Future work will explore these methods to produce volume stable PVA tissue phantoms with micron scale, interconnected channels that mimic blood perfusion. Adding this

convective heat loss to the energy balance will better model how heat is transferred in biological systems.

6.4 Bioheat transfer model

The capstone of this thesis was to predict the power requirements for a remotely heated magnetic material given the range of heat sinks that may surround the implant coating in the body. While Chapter 2 demonstrated how this coating will heat differently for a given set of design parameters—most noticeably its orientation to the applied magnetic field—Chapter 5 demonstrated how different heat sinks across the same surface will impose a substantial power gradient, further complicating the design of the composite coating and its placement in the magnetic field.

A custom built heat transfer station demonstrated experimental heat transfer measurements could be obtained through tissue and fluid mimics using precisely positioned, sub millimeter temperature probes and a carefully controlled heating element. The experimental measurements were used to validate a 3D computational model of the energy equation applied to the same geometry, material properties, and boundary conditions. Using this computational model, it was shown that large heat sinks due to convective forces resulting from fluid flow at physiologically relevant Reynold's numbers (approaching Re = 2000) require up to 15 times more power than parts of the same surface that are also exposed to a conduction-only heat sink to impose the same temperature boundary condition across the entire surface.

Predictable heat transfer through biological tissue has been approached with several modifications to the original bioheat equation given in Ref. 51, though rarely do

these modified models include experimental validation. The experimental measurements obtained here use phantoms that do not mimic all phenomena that contribute to heat transfer in living tissue. Despite this, some insight was gained for how the proposed magnetic hyperthermia will impact surrounding tissue. For example, in the conduction dominated case, temperature rise as a function of position away from the heated surface demonstrated irreversible cell death (indicated by a 10 °C temperature rise) will occur in 4-5 mm of tissue in as little as 60 sec for an extreme 80 °C surface temperature.

6.4.1 Reducing error associated with experimental measurements

One shortcoming of the 3D-printed heat transfer station used in Chapter 5 was the glass transition temperature (T_g) of the printed material. With a T_g near 55 to 60 °C, excessive heat supplied by the heating element would cause the floor of the heat transfer station to deform under the weight of the tissue mimic, thus moving the heating element and boundary condition. While attempts were made to keep the floor of the heat transfer station in place, future work will look to printing heat transfer stations with materials that have higher T_g's such as autoclavable poly(phenyl sulfone) (PPSF/PPSU, Stratasys). Additionally, a camera lens built into the flow cell wall will enable better image capturing of the thermistor probe spacing and distance away from the heating element. These two changes will produce future temperature measurement acquired at more accurately known locations.

6.4.2 Expanding the computational model

The rectangular duct implemented here for modeling fluid flow was used out of convenience resulting from the existence of the exact solution for the flow field,

assuming Poisseuille flow. Initial construction of the computational model intended to solve the flow fluid using a numerical approach via the SIMPLE algorithm which uses a pressure correction technique based on pressure differences (*i.e.* not absolute values) and thus could accommodate different geometries whose exact solution to the flow field does not exist. The code that was developed for this algorithm (given in Appendix E) would run and converge for 2D problems at low Reynolds numbers; the 3D version would not converge in a timely manner. Although this computational technique was abandoned for the exact solution, future work will require its use for more complicated geometries and for scenarios that do not assume constant viscosity and require the momentum equations be solved simultaneously with the energy equation. The mostly likely error in this code was improper execution of the pressure boundary conditions. For an incompressible fluid, the pressure gradient in the directions perpendicular to the primary direction of flow should be zero; thus, $\partial P/\partial y = \partial P/\partial z = 0$ was applied at the walls of the computational domain. Since the SIMPLE technique relies on changes in pressure to properly converge, an absolute pressure value should not need to be specified at the entrance and exit boundary conditions. Pressure boundary conditions that were attempted using the code in Appendix E were: periodic pressure conditions at the entrance and exit, pressure corrections, *p'*, equal to zero, and calculating a pressure drop assuming Poisseuille flow given the channel length in the flow direction and specifying this value at the exit with *p* = 0 specified at the entrance. None of these conditions resulted in a working code that was reliably executable for the range of flow conditions required here.

The current model essentially assumes an infinite direction in the *y*-direction (direction perpendicular to and away from the heating element) since temperature

gradients become negligible at large distances; temperature gradients are also negligible in the *x*-direction. Both of these parameters are convenient for validating the model with experimental data but do not accurately reflect the range of geometries and scenarios that would occur in the body. Using a more powerful computational model, future work will be used to quantify downstream temperature rises in the case of fluid flow through blood vessels of various sizes. Further, a model could be used to implement more appropriate boundary conditions when the implanted, heated surface is, for example, near the skin surface as opposed to being deeply embedded in tissue. In this case, boundary conditions could be imposed that reflect use of fan to implement forced convection over the skin (or even ice) in order to help cool the heated tissue so as to impose a more extreme temperature at the implanted surface/biofilm interface while reducing temperature gradients in the bulk tissue.

6.5 Closing remarks

Tissue hyperthermia is a side effect of the proposed application to wirelessly heat implanted medical devices in the body in an effort to mitigate biofilm infections that form on their surfaces. Implementation of this treatment was achieved through design of an iron oxide nanoparticle composite coating fabricated from polymer resins used in FDA approved devices. By localizing the magnetic material to a surface, power loadings were achieved that deactivated *Pseudomonas aeruginosa* biofilms—a common hospital acquired infection—below quantifiable cell viability levels. The 80 °C temperature used to achieve this degree of cell death, while extreme, is accessible with 30 wt% iron coatings placed parallel to magnetic field lines generated by a 2.3 kA m^{-1}, 302 kHz alternating magnetic field. Comparison of the types of heat sinks that may surround this

coating was observed using experimental and computational models and physiologically relevant tissue and fluid mimics. The amount of power required for different heat sinks for a given deactivation temperature and Reynolds number was explored computationally. The tissue phantom developed for this purpose demonstrated volume stability under thermal stress (up to 80 °C) with tunable thermal properties that can match specific tissues and organs. The results from this work will guide future *in vivo* applications of magnetic hyperthermia.

REFERENCES

1. Darouiche, R. O., Treatment of Infections Associated with Surgical Implants. *N.Engl.J.Med.* **2004,** *350* (14), 1422.

2. Scott, D. R. *The Direct Medical Costs of Healthcare-Associated Infections in U.S. Hospitals and the Benefits of Prevention*; Center for Diseases Control and Prevention: 2009.

3. Magill, S. S.; Edwards, J. R.; Bamberg, W.; Beldavs, Z. G.; Dumyati, G.; Kainer, M. A.; Lynfield, R.; Maloney, M.; McAllister-Hollod, L.; Nadle, J.; Ray, S. M.; Thompson, D. L.; Wilson, L. E.; Fridkin, S. K., Multistate point-prevalence survey of health care-associated infections. *N.Engl.J.Med.* **2014,** *370* (13), 1198.

4. Nickel, J. C.; Ruseska, I.; Wright, J. B.; Costerton, J. W., Tobramycin resistance of Pseudomonas aeruginosa cells growing as a biofilm on urinary catheter material. *Antimicrobial Agents and Chemotherapy* **1985,** *27* (4), 619.

5. Ratner, B. D.; Hoffman, A. S.; Schoen, F. J.; Lemons, J. E., Biofilms, Biomaterials, and Device-related Infections. In *Biomaterials Science: An Introduction to Materials in Medicine* 3rd ed.; Eds. Stoodley, P.; Hall-Stoodley, L.; Costerton, B.; Demeo, P.; Shirtliff, M.; Gawalt, E.; Kathju, S., Academic Press: Waltham, MA, USA, 2013; p 565.

6. Stoodley, P.; Sauer, K.; Davies, D. G.; Costerton, J. W., Biofilms as Complex Differentiated Communities. *Annual Review of Microbiology* **2002,** *56* (1), 187.

7. Leid, J. G.; Shirtliff, M. E.; Costerton, J. W.; Stoodley; Paul, Human Leukocytes Adhere to, Penetrate, and Respond to Staphylococcus aureus Biofilms. *Infection and Immunity* **2002,** *70* (11), 6339-6345.

8. Marrie, T. J.; Nelligan, J.; Costerton, J. W., A scanning and transmission electron microscopic study of an infected endocardial pacemaker lead. *Circulation* **1982,** *66* (6), 1339-41.

9. Sottile, F. D.; Marrie, T. J.; Prough, D. S.; Hobgood, C. D.; Gower, D. J.; Webb, L. X.; Costerton, J. W.; Gristina, A. G., Nosocomial pulmonary infection: possible etiologic significance of bacterial adhesion to endotracheal tubes. *Critical Care Medicine* **1986,** *14* (4), 265-70.

10. Sauer, K.; Camper, A. K., Characterization of Phenotypic Changes inPseudomonas putida in Response to Surface-Associated Growth. *Journal of Bacteriology* **2001,** *183* (22), 6579-6589.

11. Davies, D. G.; Geesey, G. G., Regulation of the alginate biosynthesis gene algC in Pseudomonas aeruginosa during biofilm development in continuous culture. *Applied and Environmental Microbiology* **1995,** *61* (3), 860-7.

12. Klapper, I.; Gilbert, P.; Ayati, B. P.; Dockery, J.; Stewart, P. S., Senescence can explain microbial persistence. *Microbiology* **2007,** *153* (11), 3623-3630.

13. Bagge, N.; Schuster, M.; Hentzer, M.; Ciofu, O.; Givskov, M.; Greenberg, E. P.; Høiby, N., Pseudomonas aeruginosa Biofilms Exposed to Imipenem Exhibit Changes in Global Gene Expression and β-Lactamase and Alginate Production. *Antimicrobial Agents and Chemotherapy* **2004,** *48* (4), 1175-1187.

14. O'Grady, N. P.; Alexander, M.; Burns, L. A.; Dellinger, E. P.; Garland, J.; Heard, S. O.; Lipsett, P. A.; Masur, H.; Mermel, L. A.; Pearson, M. L.; Raad, I. I.; Randolph, A. G.; Rupp, M. E.; Saint, S., Guidelines for the prevention of intravascular catheter-related infections. *American Journal of Infection Control* **2011,** *39* (4, Supplement), S1-S34.

15. Rolighed Thomsen, T.; Hall-Stoodley, L.; Moser, C.; Stoodley, P., The Role of Bacterial Biofilms in Infections of Catheters and Shunts. In *Biofilm Infections*, Springer New York: New York, NY, 2011; pp 91-109.

16. Gould, C. V.; Umscheid, C. A.; Agarwal, R. K.; Kuntz, G.; Pegues, D. A., Guideline for Prevention of Catheter-Associated Urinary Tract Infections 2009. *Infection Control & Hospital Epidemiology* **2010,** *31* (04), 319-326.

17. Wong, E. S., Guideline for prevention of catheter-associated urinary tract infections. *American Journal of Infection Control* **1983,** *11* (1), 28-33.

18. Feely, T.; Copley, A.; Bleyer, A. J., Catheter Lock Solutions to Prevent Bloodstream Infections in High-Risk Hemodialysis Patients. *American Journal of Nephrology* **2007,** *27* (1), 24-29.

19. Hetrick, E. M.; Schoenfisch, M. H., Reducing implant-related infections: active release strategies. *Chem.Soc.Rev.* **2006,** *35* (9), 780-789.

20. Campoccia, D.; Montanaro, L.; Arciola, C. R., The significance of infection related to orthopedic devices and issues of antibiotic resistance. *Biomaterials* **2006,** *27* (11), 2331-2339.

21. Carlson, R. P.; Taffs, R.; Davison, W. M.; Stewart, P. S., Anti-biofilm properties of chitosan-coated surfaces. *Journal of Biomaterials Science* **2008,** *19*, 1035-1046.

22. Gao, G.; Lange, D.; Hilpert, K.; Kindrachuk, J.; Zou, Y.; Cheng, J. T. J.; Kazemzadeh-Narbat, M.; Yu, K.; Wang, R.; Straus, S. K.; Brooks, D. E.; Chew, B. H.; Hancock, R. E. W.; Kizhakkedathu, J. N., The biocompatibility and biofilm resistance of implant coatings based on hydrophilic polymer brushes conjugated with antimicrobial peptides. *Biomaterials* **2011,** *32* (16), 3899.

23. Stoodley, P.; Nistico, L.; Johnson, S.; Lasko, L.-A.; Baratz, M.; Gahlot, V.; Ehrlich, G. D.; Kathju, S., Direct Demonstration of Viable Staphylococcus aureus Biofilms in an Infected Total Joint Arthroplasty. *The Journal of Bone and Joint Surgery* **2008,** *os-90* (8), 1751-1758.

24. Anonymous Milk, Cheese, and Dairy Products. http://www.foodsafety.gov/keep/types/milk/index.html (accessed May).

25. Hassani, M.; Álvarez, I.; Raso, J.; Condón, S.; Pagán, R., Comparing predicting models for heat inactivation of Listeria monocytogenes and Pseudomonas aeruginosa at different pH. *Int.J.Food Microbiol.* **2005,** *100* (1–3), 213.

26. Hassani, M.; Mañas, P.; Pagán, R.; Condón, S., Effect of a previous heat shock on the thermal resistance of Listeria monocytogenes and Pseudomonas aeruginosa at different pHs. *Int.J.Food Microbiol.* **2007,** *116* (2), 228.

27. O'Toole, A.; Ricker, E. B.; Nuxoll, E., Thermal mitigation of Pseudomonas aeruginosa biofilms. *Biofouling* **2015,** *31* (8), 665-675.

28. Ficko, B. W.; Nadar, P. M.; Hoopes, P. J.; Diamond, S. G., Development of a magnetic nanoparticle susceptibility magnitude imaging array. *Phys.Med.Biol.* **2014,** *59* (4), 1047.

29. Mornet, S.; Vasseur, S.; Grasset, F.; Duguet, E., Magnetic nanoparticle design for medical diagnosis and therapy. *Journal of Materials Chemistry* **2004,** *14* (14), 2161.

30. Pankhurst, Q. A.; Connolly, J.; Jones, S. K.; Dobson, J., Applications of magnetic nanoparticles in biomedicine. *Journal of Physics D: Applied Physics* **2003,** *36*, R167.

31. Reddy, L. H.; Arias, J. L.; Nicolas, J.; Couvreur, P., Magnetic Nanoparticles: Design and Characterization, Toxicity and Biocompatibility, Pharmaceutical and Biomedical Applications. *Chemical Reviews* **2012,** *112* (11), 5818-5878.

32. Li, C. H.; Hodgins, P.; Peterson, G. P., Experimental study of fundamental mechanisms in inductive heating of ferromagnetic nanoparticles suspension (Fe3O4 Iron Oxide Ferrofluid). *J.Appl.Phys.* **2011,** *110* (5), 054303.

33. Rosensweig, R. E., Heating magnetic fluid with alternating magnetic field. *J Magn Magn Mater* **2002,** *252* (1-3 SPEC. ISS.), 370.

34. O'Handley, R. C., *Modern Magnetic Materials: Principles and Applications*. John Wiley & Sons, Inc.: New York, NY, USA, 2000.

35. Gilchrist, R. K.; Medal, R.; Shorey, W. D.; Hanselman, R. C.; Parrott, J. C.; Taylor, C. B., Selective Inductive Heating of Lymph Nodes. *Annals of Surgery* **1957,** *146* (4), 596.

36. Wust, P.; Gneveckow, U.; Johannsen, M.; Böhmer, D.; Henkel, T.; Kahmann, F.; Sehouli, J.; Felix, R.; Ricke, J.; Jordan, A., Magnetic nanoparticles for interstitial thermotherapy - Feasibility, tolerance and achieved temperatures. *International Journal of Hyperthermia* **2006,** *22* (8), 673.

37. Etheridge, M. L.; Bischof, J. C., Optimizing magnetic nanoparticle based thermal therapies within the physical limits of heating. *Ann.Biomed.Eng.* **2013,** *41* (1), 78.

38. Hergt, R.; Dutz, S., Magnetic particle hyperthermia-biophysical limitations of a visionary tumour therapy. *J Magn Magn Mater* **2007,** *311* (1 SPEC. ISS.), 187.

39. Park, H.; Park, H.-J.; Kim, J. A.; Lee, S. H.; Kim, J. H.; Yoon, J.; Park, T. H., Inactivation of Pseudomonas aeruginosa PA01 biofilms by hyperthermia using superparamagnetic nanoparticles. *J.Microbiol.Methods* **2011,** *84* (1), 41.

40. Shete, P. B.; Patil, R. M.; Thorat, N. D.; Prasad, A.; Ningthoujam, R. S.; Ghosh, S. J.; Pawar, S. H., Magnetic chitosan nanocomposite for hyperthermia therapy application: Preparation, characterization and in vitro experiments. *Applied Surface Science* **2014,** *288* (0), 149-157.

41. Kallumadil, M.; Tada, M.; Nakagawa, T.; Abe, M.; Southern, P.; Pankhurst, Q. A., Suitability of commercial colloids for magnetic hyperthermia. *J Magn Magn Mater* **2009,** *321* (10), 1509.

42. Liu, X. L.; Yang, Y.; Ng, C. T.; Zhao, L. Y.; Zhang, Y.; Bay, B. H.; Fan, H. M.; Ding, J., Magnetic Vortex Nanorings: A New Class of Hyperthermia Agent for Highly Efficient In Vivo Regression of Tumors. *Advanced Materials* **2015,** *27* (11), 1939.

43. Bertoglio, P.; Jacobo, S. E.; Daraio, M. E., Preparation and characterization of PVA films with magnetic nanoparticles: The effect of particle loading on drug release behavior. *J Appl Polym Sci* **2010,** *115* (3), 1859.

44. Satarkar, N. S.; Hilt, J. Z., Magnetic hydrogel nanocomposites for remote controlled pulsatile drug release. *J.Controlled Release* **2008,** *130* (3), 246.

45. Satarkar, N. S.; Meenach, S. A.; Anderson, K. W.; Hilt, J. Z., Remote actuation of hydrogel nanocomposites: Heating analysis, modeling, and simulations. *AIChE Journal* **2011,** *57* (4), 852-860.

46. Starodubtsev, S. G.; Saenko, E. V.; Dokukin, M. E.; Aksenov, V. L.; Klechkovskaya, V. V.; Zanaveskina, I. S.; Khokhlov, A. R., Formation of magnetite nanoparticles in poly(acrylamide) gels. *Journal of Physics: Condensed Matter* **2005,** *17* (10), 1471.

47. Cressman, E. N. K.; Geeslin, M. G.; Shenoi, M. M.; Hennings, L. J.; Zhang, Y.; Iaizzo, P. A.; Bischof, J. C., Concentration and volume effects in thermochemical ablation in vivo: Results in a porcine model. *Int. J. Hyperther.* **2012,** *28* (2), 113-121.

48. Staruch, R. M.; Ganguly, M.; Tannock, I. F.; Hynynen, K.; Chopra, R., Enhanced drug delivery in rabbit VX2 tumours using thermosensitive liposomes and MRI-controlled focused ultrasound hyperthermia. *Int. J. Hyperther.* **2012,** *28* (8), 776-787.

49. Arkin, H.; Xu, L. X.; Holmes, K. R., Recent developments in modeling heat transfer in blood perfused tissues. *IEEE Trans. Biomed. Eng.* **1994,** *41* (2), 97.

50. Bagaria, H. G.; Johnson, D. T., Transient solution to the bioheat equation and optimization for magnetic fluid hyperthermia treatment. *Int. J. Hyperther.* **2005,** *21* (1), 57.

51. Pennes, H. H., Analysis of tissue and arterial blood temperatures in resting forearm. *J. Appl. Physiol.* **1948,** *1*, 93-122.

52. Lazebnik, M.; Madsen, E. L.; Frank, G. R.; Hagness, S. C., Tissue-mimicking phantom materials for narrowband and ultrawideband microwave applications. *Phy. Med. Biol.* **2005,** *50* (18), 4245-4258.

53. Surry, K. J. M.; Austin, H. J. B.; Fenster, A.; Peters, T. M., Poly(vinyl alcohol) cryogel phantoms for use in ultrasound and MR imaging. *Phy. Med. Biol.* **2004,** *49* (24), 5529.

54. Yella, A.; Li, B. Q.; Mohanty, P.; Liu, C., Measurement of temperature distribution and evolution during surface plasma resonance heating of gold nanoshells-embedded phantom tissue. *Exp. Therm. Fluid Sci.* **2013,** *47* (0), 34-39.

55. Divkovic, G. W.; Liebler, M.; Braun, K.; Dreyer, T.; Huber, P. E.; Jenne, J. W., Thermal Properties and Changes of Acoustic Parameters in an Egg White Phantom During Heating and Coagulation by High Intensity Focused Ultrasound. *Ultrasound Med. Biol.* **2007,** *33* (6), 981-986.

56. Pogue, B. W.; Patterson, M. S., Review of tissue simulating phantoms for optical spectroscopy, imaging and dosimetry. *J. Biomed. Opt.* **2006,** *11* (4), 041102-041116.

57. Davidson, S. R. H.; James, D. F., Measurement of thermal conductivity of bovine cortical bone. *Med. Eng. Phys.* **2000,** *22* (10), 741-747.

58. Valvano, J. W.; Cochran, J. R.; Diller, K. R., Thermal conductivity and diffusivity of biomaterials measured with self-heated thermistors. *Int. J. Thermophys.* **1985,** *6* (3), 301-311.

59. Cohen, M., L, Measurement of the Thermal Properties of Human Skin. A Review. *J. Invet. Dermatol.* **1977,** *69* (3), 333.

60. Davidson, S. R. H.; Sherar, M. D., Measurement of the thermal conductivity of polyacrylamide tissue-equivalent material. *Int. J. Hyperther.* **2003,** *19* (5), 551.

61. Mazzara, G. P.; Briggs, R. W.; Wu, Z.; Steinbach, B. G., Use of a modified polysaccharide gel in developing a realistic breast phantom for MRI. *Magn. Reson. Imaging* **1996,** *14* (6), 639-648.

62. Dabbagh, A.; Abdullah, B. J. J.; Ramasindarum, C.; Abu Kasim, N. H., Tissue-mimicking gel phantoms for thermal therapy studies. *Ultrasonic Imaging* **2014,** *36* (4), 291-316.

63. Hellerbach, A.; Schuster, V.; Jansen, A.; Sommer, J., MRI Phantoms – Are There Alternatives to Agar? *PLoS ONE* **2013,** *8* (8), e70343.

64. Pritchard, J. G., *Poly(vinyl alcohol) basic properties and uses*. Gordon and Breach: New York, NY, 1970.

65. Giménez, V.; Mantecón, A.; Cádiz, V., Modification of poly(vinyl alcohol) with acid chlorides and crosslinking with difunctional hardeners. *J. Polym. Sci. Pol. Chem.* **1996,** *34* (6), 925-934.

66. Hassan, C. M.; Peppas, N. A., Structure and Applications of Poly(vinyl alcohol) Hydrogels Produced by Conventional Crosslinking or by Freezing/Thawing Methods. *Adv. Pol. Sci.* **2000,** *153*, 37-65.

67. Jayakrishnan, A.; Jameela, S. R., Glutaraldehyde as a fixative in bioprostheses and drug delivery matrices. *Biomaterials* **1996,** *17* (5), 471.

68. Mansur, H. S.; Sadahira, C. M.; Souza, A. N.; Mansur, A. A. P., FTIR spectroscopy characterization of poly (vinyl alcohol) hydrogel with different hydrolysis degree and chemically crosslinked with glutaraldehyde. *Materials Science and Engineering: C* **2008,** *28* (4), 539-548.

69. Canal, T.; Peppas, N. A., Correlation between mesh size and equilibrium degree of swelling of polymeric networks. *J. Biomed. Mater. Res.* **1989,** *23* (10), 1183-1193.

70. Hickey, A. S.; Peppas, N. A., Mesh size and diffusive characteristics of semicrystalline poly(vinyl alcohol) membranes prepared by freezing/thawing techniques. *J. Membrane Sci.* **1995,** *107* (3), 229-237.

71. Chu, K. C.; Rutt, B. K., Polyvinyl alcohol cryogel: An ideal phantom material for MR studies of arterial flow and elasticity. *Magnetic Resonance in Medicine* **1997,** *37* (2), 314-319.

72. Mano, I.; Goshima, H.; Nambu, M.; Iio, M., New polyvinyl alcohol gel material for MRI phantoms. *Magnetic Resonance in Medicine* **1986,** *3* (6), 921-926.

73. Zrínyi, M.; Barsi, L.; Büki, A., Ferrogel: a new magneto-controlled elastic medium. *Polym.Gels Networks* **1997,** *5* (5), 415.

74. Schwertmann, U.; Cornell, R. M., *Iron oxides in the laboratory: preparation and characterization*. 2nd completely rev. and extended ed.. ed.; Wiley-VCH: Weinheim, NY, USA, 2000.

75. Hergt, R.; Dutz, S.; Müller, R.; Zeisberger, M., Magnetic particle hyperthermia: nanoparticle magnetism and materials development for cancer therapy. *Journal of Physics: Condensed Matter* **2006,** *18* (38), S2919.

76. Teja, A. S.; Koh, P. Y., Synthesis, properties, and applications of magnetic iron oxide nanoparticles. *Progress in Crystal Growth and Characterization of Materials* **2009,** *55* (1-2), 22.

77. Tamura, H.; Goto, K.; Yotsuyanagi, T.; Nagayama, M., Spectrophotometric determination of iron(II) with 1,10-phenanthroline in the presence of large amounts of iron(III). *Talanta* **1974,** *21* (4), 314.

78. Gorski, C. A.; Scherer, M. M., Determination of nanoparticulate magnetite stoichiometry by Mossbauer spectroscopy, acidic dissolution, and powder X-ray diffraction: A critical review. *American Mineralogist* **2010,** *95* (7), 1017.

79. Riani, P.; Napoletano, M.; Canepa, F., Synthesis, characterization and a.c. magnetic analysis of magnetite nanoparticles. *Journal of Nanoparticle Research* **2011,** *13* (12), 7013.

80. Mark, H. F., Vinyl Alcohol Polymers. In *Encyclopedia of polymer science and engineering*, 2nd ed.; Eds. Mark, H. F.; Kroschwitz, J. I., New York : Wiley: New York, 1985; Vol. 8, pp 405-409.

81. Ricker, E. B.; Bader, T. M.; Hundley, B. S.; Nuxoll, E., Evaluation of Thermal Shock Susceptibility of *Pseudomonas aeruginosa* Biofilms. *Biotechnology Journal* **2016,** *Submitted*.

82. Bini, M. G.; Ignesti, A.; Millanta, L.; Olmi, R.; Rubino, N.; Vanni, R., The Polyacrylamide as a Phantom Material for Electromagnetic Hyperthermia Studies. *Biomedical Engineering, IEEE Transactions on* **1984,** *BME-31* (3), 317-322.

83. Bolto, B.; Tran, T.; Hoang, M.; Xie, Z., Crosslinked poly(vinyl alcohol) membranes. *Prog. Polym. Sci.* **2009,** *34* (9), 969-981.

84. Vidal, M. M. B.; Gil, M. H.; Delgadillo, I.; Chamarro, J. A., Swelling and Thermal Properties of Poly(Vinyl Alcohol) Containing Hemoglobin Membranes. *J. Bioact. Compat. Pol.* **1999,** *14* (3), 243-257.

85. Hirokawa, Y.; Tanaka, T., Volume phase transition in a nonionic gel. *The Journal of Chemical Physics* **1984,** *81* (12), 6379-6380.

86. Bird, R. B.; Stewart, W. E.; Lightfoot, E. N., *Transport Phenomena*. Wiley: New York, 1960.

87. Carslaw, H. S.; Jaeger, J. C., *Conduction of heat in solids*. 2nd ed. ed.; Clarendon Press: Oxford, 1959.

88. Gaur, U.; Wunderlich, B. B.; Wunderlich, B., Heat Capacity and Other Thermodynamic Properties of Linear Macromolecules. VII. Other Carbon Backbone Polymers. *J. Phys. Chem. Ref. Data* **1983,** *12* (1), 29-63.

89. Chang, S.-S., Heat Capacity and Thermodynamic Properties of Poly(Vinyl Chloride). Institute for Materials Research, N. B. o. S., Ed. Washington, D.C., 1977; Vol. 82, pp 9-18.

90. Rashed, A. H. Properties and Characteristics of Silicon Carbide. http://www.poco.com/Portals/0/Properties.and.Characteristics.of.Silicon.Carbide.pdf (accessed August 6).

91. Dewhirst, M. W.; Viglianti, B. L.; Lora-Michiels, M.; Hanson, M.; Hoopes, P. J., Basic principles of thermal dosimetry and thermal thresholds for tissue damage from hyperthermia. *Int. J. Hyperther.* **2003,** *19* (3), 267.

92. Bellan, L. M.; Pearsall, M.; Cropek, D. M.; Langer, R., A 3D Interconnected Microchannel Network Formed in Gelatin by Sacrificial Shellac Microfibers. *Advanced Materials* **2012,** *24* (38), 5187-5191.

93. Bellan, L. M.; Singh, S. P.; Henderson, P. W.; Porri, T. J.; Craighead, H. G.; Spector, J. A., Fabrication of an artificial 3-dimensional vascular network using sacrificial sugar structures. *Soft Matter* **2009,** *5* (7), 1354-1357.

94. Terasaki, D.; Sobel, M.; Irvin, C.; Wijelath, E.; Ratner, B. D., Biomaterial-Induced Angiogenesis To Address Peripheral Vascular Disease: The Application of Sphere Templated Hydrogels. In *Tailored Polymer Architectures for Pharmaceutical and Biomedical Applications*, American Chemical Society: 2013; Vol. 1135, pp 245-257.

APPENDIX A: FORTRAN CODE FOR THREE DIMENSIONAL, CONDUCTION ONLY HEAT TRANSFER

```
      Program main

!This program solves 3D, transient heat transfer in a solid tissue
mimic
!on top of a constant temperature boundary condition. This scenario
!assumes constant material properties
!(i.e. heat capacity, thermal conductivity, density, and viscosity).
!Solid tissue is assumed to have the thermal properties of
!~8% poly(vinyl alcohol) tissue mimic
!
!VARIABLES and PARAMETERS:
!xlen=length of channel [=] m
!ydist=height of channel, direction perpendicular to temp BC [=] m
!zdep=depth of channel, direction parallel to temp BC [=] m
!alphati = thermal diffusivity of tissue mimic [=] m^2*s^-1
!ktis = tissue mimic thermal conductivity [=] W m^-1 °C^-1
!t=time [=] s
!T=temperature [=] °C
!T0=initial temperature (at time, t=0)of entire system [=] °C
!Tbc =temperature boundary condition (t>0) [=] °C

!PHYSICAL GEOMETRY
!mimic(s) are modeled in a 2.54 by 2.54 cm cross-section flow cell
of
!length = 7.62 cm. This void is surrounded by a 0.3175 cm-thick wall
!assumed to have physical properties of acrylic (PMMA), the model
also
!includes a 1.27 layer of air completely surrounding the flow cell

!BOUNDARY CONDITIONS:
!T is constant at 23 °C at all air boundaries
!Constant temperature boundary condition is applied from i=1 to
i=imax
!and in the xz plan at the flow cell floor
!periodic temperature boundary condition at i=1 and i=imax

!BEGIN CODE:

      Real*8Rwmax
      Integer wmax,imax,jmax,kmax

!wmax is number of nodes spanning y and z directions in the flow
cell !void (not including walls and air), jmax and kmax
!are the total number of nodes in the y and z direction including
!wmax, and the number of nodes across the walls and air surrounding
!the flow cell. Number of nodes in wall is equal to 1/8 of wmax
!and number of nodes in air is 1/2 wmax. Thus, wmax should be a
!multiple of 8
```

```
      Rwmax= 32
      wmax=int(Rwmax)
      imax=int(1.5*Rwmax)
      jmax=int(2.25*Rwmax)
      kmax=jmax

      Call Energy (wmax,imax,jmax,kmax)

      End

      Subroutine Energy (wmax,imax,jmax,kmax)
        Integer i,j,k,wmax,imax,jmax,kmax,maxits,kmaxbl
        Integer y1,y2,y3,y4,z1,z2,z3,z4
        Integer ittotal,time
        Logical tolex
        Parameter (solved=0,limit=1)
        Real*8 xlen,ydist,zdep,delt,ttotal,delx,dely,delz,ktis,qz
        Real*8 alphaair,alphawall,alphatis,,tol,Ti,Tbc
        Real*8 T(imax,jmax,kmax),u(imax,jmax,kmax)
        Real*8 alpha(imax,jmax,kmax),Tprobe(7),yT(7)

!Read parameter values
      y1=wmax/2   !end of air boundary
      y2=y1+wmax/8   !end of wall boundary
      y3=y2+wmax   !end of mimic boundary
      y4=y3+wmax/8  !end of second wall boundary
      z1=y1
      z2=y2
      z3=y3
      z4=y4
      xlen=0.0762
      ydist=0.05715
      zdep=0.05715
      delx=xlen/imax
      dely=ydist/jmax
      delz=zdep/kmax
      delt=0.01   !size of time step
      ttotal=300.0   !total time length of model in seconds
      ittotal=int(ttotal/delt)  !total number of iterations
      alphaair=2.16e-5
      alphawall=1.3e-8
      alphatis=1.41e-7
      ktis=0.578
      Ti=37.0
      Tbc=50.0   !constant temp BC fro all i and from j=y2+1 to y3
and
                 !k=z2+1 to z3

!Initial conditions:
      T=Ti

!y distance of flow cell probes used for data output
      Do i=1,7
        yT(i)=(y2+1)*dely+0.00045
```

```
      End Do
      yT(1)=yT(1)+0.00044
      yT(2)=yT(2)+0.00140
      yT(3)=yT(3)+0.00213
      yT(4)=yT(4)+0.00425
      yT(5)=yT(5)+0.00747
      yT(6)=yT(6)+0.01334
      yT(7)=yT(7)+0.02191

!Temperature boundary conditions:
!T(i,y2+1,k)=Tbc
      Do i=1,imax
        Do k=z2+1,z3
          T(i,y2+1,k)=Tbc
        End Do
      End Do

!Assign thermal diffusivity to grid
      Do i=1,imax
        Do j=1,y1
          Do k=1,kmax
            alpha(i,j,k)=alphaair
          End Do
        End Do
        Do j=y1+1,y2
          Do k=1,z1
            alpha(i,j,k)=alphaair
          End Do
          Do k=z1+1,z4
            alpha(i,j,k)=alphawall
          End Do
          Do k=z4+1,kmax
            alpha(i,j,k)=alphaair
          End Do
        End Do
        Do j=y2+1,y3
          Do k=1,z1
            alpha(i,j,k)=alphaair
          End Do
          Do k=z1+1,z2
            alpha(i,j,k)=alphawall
          End Do
          Do k=z2,z3
            alpha(i,j,k)=alphatis
          End Do
          Do k=z3+1,z4
            alpha(i,j,k)=alphawall
          End Do
          Do k=z4+1,kmax
            alpha(i,j,k)=alphaair
          End Do
        End Do
        Do j=y3+1,y4
          Do k=1,z1
```

```
            alpha(i,j,k)=alphaair
          End Do
          Do k=z1+1,z4
            alpha(i,j,k)=alphawall
          End Do
          Do k=z4+1,kmax
            alpha(i,j,k)=alphaair
          End Do
        End Do
        Do j=y4+1,jmax
          Do k=1,kmax
            alpha(i,j,k)=alphaair
          End Do
        End Do
      End Do


!Begin time marching, calculate temp field at each time step
      Do time=1,ittotal
        print *, time*delt
        Do i=2,imax-1
          Do j=2,jmax-1
            Do k=2,kmax-1
              If (j.eq.y2+1.and.k.gt.z2+1.and.k.lt.z3+1) Then
                T(i,j,k)=T(i,j,k)
              Else
                 T(i,j,k)=T(i,j,k)+delt*(alpha(i,j,k)*((T(i+1,j,k)-
     &          2.0*T(i,j,k)+T(i-1,j,k))/delx**2+(T(i,j+1,k)-
2.0*T(i,j,k)
     &          +T(i,j-1,k))/dely**2+(T(i,j,k+1)-2.0*T(i,j,k)
     &          +T(i,j,k-1))/delz**2)-(T(i+1,j,k)*u(i+1,j,k)-T(i-
1,j,k)*
     &           u(i-1,j,k))/(2.0*delx))
              End If
            End Do
          End Do
        End Do

!update boundary conditions
!Boundary conditions at air boundaries are constant
!Boundary conditions at flow cell ends (i=1 and i=imax) are periodic
      Do j=1,jmax
        Do k=1,kmax
          T(imax,j,k)=T(imax-1,j,k)
          T(1,j,k)=T(imax,j,k)
        End Do
      End Do

!Export temp field to .csv file evey 5000 iterations
      If (mod(time,5000).eq.0.or.time.eq.1) Then
        Call logdata(imax,jmax,kmax,T,delt,time)
      End If
```

```
!Export transient temp profiles at probe locations every 100 time
steps
      If (mod(time,100).eq.0.) Then
        Open (3,File='transprobetemp022.csv')
   30   Format(9(F6.2,','))
        Do i=1,7
          Do j=1,jmax
            If(j*dely.lt.yT(i).and.(j+1)*dely.gt.yT(i)) Then
            Tprobe(i)=(T(imax/2,j+1,kmax/2)-
T(imax/2,j,kmax/2))/j/dely
     &       *(yT(i)-j*dely)+T(imax/2,j,kmax/2)
            End If
          End Do
        End Do
!calculate heat flux in middle of flow cell at BC, q reported in
!units of W*cm^-2
          qz=(3.0*T(imax/2,y2+1,kmax/2)-4.0* T(imax/2,y2+2,kmax/2)
     &       +T(imax/2,y2+3,kmax/2))*kbl/2.0/dely/10000.0



write(3,30)delt*time,Tprobe(1),Tprobe(2),Tprobe(3),Tprobe(4),
     &             Tprobe(5),Tprobe(6),Tprobe(7),qz
      End If



      End Do
      End

!Data output for temp field subroutine

      Subroutine logdata(imax,jmax,kmax,T,delt,time)

      Real*8 T(imax,jmax,kmax)
      Real*8 delt
      Integer imax,jmax,kmax,time

        Open (1,File='2D_Tfieldxy022.csv')
        Open (2,File='2D_Tfieldyz022.csv')
   10   Format(48(E12.4,','))
   20   Format(72(E12.4,','))
      write(1,*)delt*time
      Do j=1,jmax
      write(1,10)T(1,j,36),T(2,j,36),T(3,j,36),T(4,j,36),
     $     T(5,j,36),T(6,j,36),T(7,j,36),
     &     T(8,j,36),T(9,j,36),T(10,j,36),T(11,j,36),
     &     T(12,j,36),T(13,j,36),
     &     T(14,j,36),T(15,j,36),T(16,j,36),T(17,j,36),T(18,j,36),
     &     T(19,j,36),T(20,j,36),
     &     T(21,j,36),T(22,j,36),T(23,j,36),T(24,j,36),T(25,j,36),
     &     T(26,j,36),T(27,j,36),
     &     T(28,j,36),T(29,j,36),T(30,j,36),T(31,j,36),T(32,j,36),
     &     T(33,j,36),
```

```
     &     T(34,j,36),T(35,j,36),T(36,j,36),T(37,j,36),T(38,j,36),
     &     T(39,j,36),
     &     T(40,j,36),T(41,j,36),T(42,j,36),T(43,j,36),T(44,j,36),
     &     T(45,j,36),
     &     T(46,j,36),T(47,j,36),T(48,j,36)!,T(49,j,36),T(50,j,36),
!     &     T(51,j,36),
!     &     T(52,j,36),T(53,j,36),T(54,j,36),T(55,j,36),T(56,j,36),
!     &     T(57,j,36)
      End Do
      write(2,*)delt*time
      Do j=1,jmax
      write(2,20)T(21,J,1),T(21,J,2),T(21,J,3),T(21,J,4),
     $     T(21,J,5),T(21,J,6),T(21,J,7),
     &     T(21,J,8),T(21,J,9),T(21,J,10),T(21,J,11),
     &     T(21,J,12),T(21,J,13),
     &     T(21,J,14),T(21,J,15),T(21,J,16),T(21,J,17),T(21,J,18),
     &     T(21,J,19),T(21,J,20),
     &     T(21,J,21),T(21,J,22),T(21,J,23),T(21,J,24),T(21,J,25),
     &     T(21,J,26),T(21,J,27),
     &     T(21,J,28),T(21,J,29),T(21,J,30),T(21,J,31),T(21,J,32),
     &     T(21,J,33),
     &     T(21,J,34),T(21,J,35),T(21,J,36),T(21,J,37),T(21,J,38),
     &     T(21,J,39),
     &     T(21,J,40),T(21,J,41),T(21,J,42),T(21,J,43),T(21,J,44),
     &     T(21,J,45),
     &     T(21,J,46),T(21,J,47),T(21,J,48),T(21,J,49),T(21,J,50),
     &     T(21,J,51),
     &     T(21,J,52),T(21,J,53),T(21,J,54),T(21,J,55),T(21,J,56),
     &     T(21,J,57),
     &     T(21,J,58),T(21,J,59),T(21,J,60),T(21,J,61),T(21,J,62),
     &     T(21,J,63),
     &     T(21,J,64),T(21,J,65),T(21,J,66),T(21,J,67),T(21,J,68),
     &     T(21,J,69),T(21,j,70),T(21,j,71),T(21,j,72)

      End Do
!        Close(1)
!        Close(2)
      End
```

APPENDIX B: FORTRAN CODE FOR THREE DIMENSIONAL, CONVECTION ONLY HEAT TRANSFER

```
      Program main

!This program solves 3D, transient heat transfer in a blood flow
mimic on !top of a constant temperature boundary condition. This
scenario assumes !constant material properties
!(i.e. heat capacity, thermal conductivity, density, and viscosity).
!Thus, the momentum and continuity equations can be decoupled from
the
!energy equation and solved separately. The exact velocity field is
!supplied to the energy equation by assuming Poiseuille flow in 2D
!(y and z), i.e. du/dx=0.
!Blood is assumed to have the thermal properties of water
!
!VARIABLES and PARAMETERS:
!xlen=length of channel and direction of fluid flow [=] m
!ydist=height of channel, direction perpendicular to temp BC [=] m
!zdep=depth of channel, direction parallel to temp BC [=]= m
!mu = viscosity of bloodm mimic [=] kg*m^-1*s^-1
!alphati = thermal diffusivity of blood mimic [=] m^2*s^-1
!ktis = fluid mimic thermal conductivity [=] W m^-1 °C^-1
!t=time [=] s
!T=temperature [=] °C
!u = x-component velocity [=] m*s^-1
!Q = x-component volumetric flow rate [=] m^3*s^-1
!T0=initial temperature (at time, t=0)of entire system [=] °C
!Tbc =temperature boundary condition (t>0) [=] °C

!PHYSICAL GEOMETRY
!Fluid mimic is modeled in a 2.54 by 2.54 cm cross-section flow cell
of
!length = 7.62 cm. This void is surrounded by a 0.3175 cm-thick wall
!assumed to have physical properties of acrylic (PMMA), the model
also
!includes a 1.27 layer of air completely surrounding the flow cell

!BOUNDARY CONDITIONS:
!no slip at all walls
!For fluid flow, T is constant at i=1 and allowed to float at i=imax
!T is constant at 23 °C at all air boundaries
!Constant temperature boundary condition is applied from i=1 to
i=imax
!and in the xz plan at the flow cell floor

!BEGIN CODE:

      Real*8Rwmax
      Integer wmax,imax,jmax,kmax
```

```
!wmax is number of nodes spanning y and z directions in the flow
cell !void (not including walls and air), jmax and kmax
!are the total number of nodes in the y and z direction including
!wmax, and the number of nodes across the walls and air surrounding
!the flow cell. Number of nodes in wall is equal to 1/8 of wmax
!and number of nodes in air is 1/2 wmax. Thus, wmax should be a
!multiple of 8

      Rwmax= 40
      wmax=int(Rwmax)
      imax=int(1.5*Rwmax)
      jmax=int(2.25*Rwmax)
      kmax=jmax

      Call Energy (wmax,imax,jmax,kmax)

      End

      Subroutine Energy (wmax,imax,jmax,kmax)
        Integer i,j,k,n,wmax,imax,jmax,kmax,maxits,kmaxbl
        Integer y1,y2,y3,y4,z1,z2,z3,z4
        Integer ittotal,time
        Logical tolex
        Parameter (solved=0,limit=1)
        Real*8 xlen,ydist,zdep,delt,ttotal,delx,dely,delz
        Real*8 alphaair,alphawall,alphatis,alphabl,mu,ue,tol,Ti,Tbc
        Real*8 h,L,w,y,z,sum,Q,delP,pi,qz,kbl
        Real*8 T(imax,jmax,kmax),u(imax,jmax,kmax)
        Real*8 alpha(imax,jmax,kmax),Tprobe(7),yT(7)

!Read parameter values
      y1=wmax/2   !end of air boundary
      y2=y1+wmax/8   !end of wall boundary
      y3=y2+wmax   !end of mimic boundary
      y4=y3+wmax/8  !end of second wall boundary
      z1=y1
      z2=y2
      z3=y3
      z4=y4
      xlen=0.0762
      ydist=0.05715
      zdep=0.05715
      delx=xlen/imax
      dely=ydist/jmax
      delz=zdep/kmax
      delt=0.005   !size of time step
      ttotal=300.0   !total time length of model in seconds
      ittotal=int(ttotal/delt)  !total number of iterations
      alphaair=2.16e-5
      alphawall=1.3e-8
      alphabl=1.44e-7
      kbl=0.6
      mu=0.000894
      Q=0.20/1000.0/60.0  ! volumetric flow rate [=] m^3*s^-1
```

```
      Ti=37.0
      Tbc=50.0
      pi=4.0*atan(1.0)

!Initial conditions:
      u=0.0
      T=Ti

!y distance of flow cell probes
      Do i=1,7
        yT(i)=(y2+1)*dely
      End Do
      yT(1)=yT(1)+0.00044+0.0002
      yT(2)=yT(2)+0.00140
      yT(3)=yT(3)+0.00213
      yT(4)=yT(4)+0.00425
      yT(5)=yT(5)+0.00747
      yT(6)=yT(6)+0.01334
      yT(7)=yT(7)+0.02191


!Define flow field
      h=wmax*dely
      L=xlen
      w=h
      sum=0.0
      Do n=0,100
        sum=sum+192.0*h/(pi)**5.0/w/(2.0*n+1.0)**5
     &       *tanh((2.0*n+1.0)*pi*w/2.0/h)
      End Do
      delP=Q*12*mu/w/h**3/(1-sum)
      Do i=1,imax
        Do j=y2+1,y3
            y=h/(float(y3-y2)-1.0)*float(j-y3)+h/2.0
          Do k=z2+1,z3
            z=w/(float(z3-z2)-1.0)*float(k-z3)+w/2.0
            sum=0.0
            Do n=0,100
              sum=sum+32.0*(-1.0)**n*cosh((2.0*n+1.0)*pi*z/h)
     &             *cos((2*n+1.0)*pi*y/h)/(2.0*n+1.0)**3/(pi)**3
     &             /cosh((2.0*n+1.0)*pi*w/2.0/h)
!       print *,sum
            End Do
            u(i,j,k)=delP*h**2/8/mu/L*(1-4.0*y**2/h**2-sum)
          End Do
        End Do
      End Do

!Temperature boundary conditions:
!T(i,y2+1,k)=Tbc
      Do i=1,imax
        Do k=z2+1,z3
          T(i,y2+1,k)=Tbc
        End Do
```

```
      End Do

!Assign thermal diffusivity to grid
      Do i=1,imax
        Do j=1,y1
          Do k=1,kmax
            alpha(i,j,k)=alphaair
          End Do
        End Do
        Do j=y1+1,y2
          Do k=1,z1
            alpha(i,j,k)=alphaair
          End Do
          Do k=z1+1,z4
            alpha(i,j,k)=alphawall
          End Do
          Do k=z4+1,kmax
            alpha(i,j,k)=alphaair
          End Do
        End Do
        Do j=y2+1,y3
          Do k=1,z1
            alpha(i,j,k)=alphaair
          End Do
          Do k=z1+1,z2
            alpha(i,j,k)=alphawall
          End Do
          Do k=z2,z3
            alpha(i,j,k)=alphabl
          End Do
          Do k=z3+1,z4
            alpha(i,j,k)=alphawall
          End Do
          Do k=z4+1,kmax
            alpha(i,j,k)=alphaair
          End Do
        End Do
        Do j=y3+1,y4
          Do k=1,z1
            alpha(i,j,k)=alphaair
          End Do
          Do k=z1+1,z4
            alpha(i,j,k)=alphawall
          End Do
          Do k=z4+1,kmax
            alpha(i,j,k)=alphaair
          End Do
        End Do
        Do j=y4+1,jmax
          Do k=1,kmax
            alpha(i,j,k)=alphaair
          End Do
        End Do
      End Do
```

```
!Begin time marching, calculate temp field at each time step
      Do time=1,ittotal
        print *, time*delt
        Do i=2,imax-1
          Do j=2,jmax-1
            Do k=2,kmax-1
              If (j.eq.y2+1.and.k.gt.z2+1.and.k.lt.z3+1) Then
                T(i,j,k)=T(i,j,k)
              Else
                 T(i,j,k)=T(i,j,k)+delt*(alpha(i,j,k)*((T(i+1,j,k)-
     &          2.0*T(i,j,k)+T(i-1,j,k))/delx**2+(T(i,j+1,k)-
2.0*T(i,j,k)
     &          +T(i,j-1,k))/dely**2+(T(i,j,k+1)-2.0*T(i,j,k)
     &          +T(i,j,k-1))/delz**2)-(T(i+1,j,k)*u(i+1,j,k)-T(i-
1,j,k)*
     &           u(i-1,j,k))/(2.0*delx))
              End If
            End Do
          End Do
        End Do

!update boundary conditions
!Temperature boundary conditions at air boundaries are constant
!Boundary conditions at flow cell ends (i=1 and i=imax) are periodic
for
!the conduction only scenario. For convection, T=constant at i=1 and
!T(imax,j,k)=T(imax-1,j,k)
      Do j=1,jmax
        Do k=1,kmax
          T(imax,j,k)=T(imax-1,j,k)
!          T(1,j,k)=T(imax,j,k)
        End Do
      End Do

!Export temp field to .csv file evey 5000 iterations
      If (mod(time,5000).eq.0.or.time.eq.1) Then
        Call logdata(imax,jmax,kmax,T,delt,time)
      End If

!Export transient temp profiles at probe locations every 100 time
steps
      If (mod(time,100).eq.0.) Then
        Open (3,File='transprobetemp025.csv')
   30   Format(9(F6.2,','))
        Do i=1,7
          Do j=1,jmax
            If(j*dely.lt.yT(i).and.(j+1)*dely.gt.yT(i)) Then
            Tprobe(i)=(T(imax/2,j+1,kmax/2)-
T(imax/2,j,kmax/2))/j/dely
     &      *(yT(i)-j*dely)+T(imax/2,j,kmax/2)
            End If
          End Do
```

```
        End Do
!calculate heat flux in middle of flow cell at BC, q reported in
!units of W*cm^-2
          qz=(3.0*T(imax/2,y2+1,kmax/2)-4.0* T(imax/2,y2+2,kmax/2)
     &       +T(imax/2,y2+3,kmax/2))*kbl/2.0/dely/10000.0


write(3,30)delt*time,Tprobe(1),Tprobe(2),Tprobe(3),Tprobe(4),
     &             Tprobe(5),Tprobe(6),Tprobe(7),qz
      End If



      End Do
      End

!Data output for temp field subroutine

      Subroutine logdata(imax,jmax,kmax,T,delt,time)

      Real*8 T(imax,jmax,kmax)
      Real*8 delt
      Integer imax,jmax,kmax,time

        Open (1,File='2D_Tfieldxy025.csv')
        Open (2,File='2D_Tfieldyz025.csv')
   10   Format(48(E12.4,','))
   20   Format(72(E12.4,','))
      write(1,*)delt*time
      Do j=1,jmax
      write(1,10)T(1,j,45),T(2,j,45),T(3,j,45),T(4,j,45),
     $     T(5,j,45),T(6,j,45),T(7,j,45),
     &     T(8,j,45),T(9,j,45),T(10,j,45),T(11,j,45),
     &     T(12,j,45),T(13,j,45),
     &     T(14,j,45),T(15,j,45),T(16,j,45),T(17,j,45),T(18,j,45),
     &     T(19,j,45),T(20,j,45),
     &     T(21,j,45),T(22,j,45),T(23,j,45),T(24,j,45),T(25,j,45),
     &     T(26,j,45),T(27,j,45),
     &     T(28,j,45),T(29,j,45),T(30,j,45),T(31,j,45),T(32,j,45),
     &     T(33,j,45),
     &     T(34,j,45),T(35,j,45),T(36,j,45),T(37,j,45),T(38,j,45),
     &     T(39,j,45),
     &     T(40,j,45),T(41,j,45),T(42,j,45),T(43,j,45),T(44,j,45),
     &     T(45,j,45),
     &     T(46,j,45),T(47,j,45),T(48,j,45)!,T(49,j,45),T(50,j,45),
!     &      T(51,j,45),
!     &      T(52,j,45),T(53,j,45),T(54,j,45),T(55,j,45),T(56,j,45),
!     &      T(57,j,45)
      End Do
      write(2,*)delt*time
      Do j=1,jmax
      write(2,20)T(21,J,1),T(21,J,2),T(21,J,3),T(21,J,4),
     $     T(21,J,5),T(21,J,6),T(21,J,7),
     &     T(21,J,8),T(21,J,9),T(21,J,10),T(21,J,11),
```

```
     &     T(21,J,12),T(21,J,13),
     &     T(21,J,14),T(21,J,15),T(21,J,16),T(21,J,17),T(21,J,18),
     &     T(21,J,19),T(21,J,20),
     &     T(21,J,21),T(21,J,22),T(21,J,23),T(21,J,24),T(21,J,25),
     &     T(21,J,26),T(21,J,27),
     &     T(21,J,28),T(21,J,29),T(21,J,30),T(21,J,31),T(21,J,32),
     &     T(21,J,33),
     &     T(21,J,34),T(21,J,35),T(21,J,36),T(21,J,37),T(21,J,38),
     &     T(21,J,39),
     &     T(21,J,40),T(21,J,41),T(21,J,42),T(21,J,43),T(21,J,44),
     &     T(21,J,45),
     &     T(21,J,46),T(21,J,47),T(21,J,48),T(21,J,49),T(21,J,50),
     &     T(21,J,51),
     &     T(21,J,52),T(21,J,53),T(21,J,54),T(21,J,55),T(21,J,56),
     &     T(21,J,57),
     &     T(21,J,58),T(21,J,59),T(21,J,60),T(21,J,61),T(21,J,62),
     &     T(21,J,63),
     &     T(21,J,64),T(21,J,65),T(21,J,66),T(21,J,67),T(21,J,68),
     &     T(21,J,69),T(21,j,70),T(21,j,71),T(21,j,72)

      End Do
!        Close(1)
!        Close(2)
      End
```

APPENDIX C: FORTRAN CODE FOR THREE DIMENSIONAL, COMBINED CONVECTION, CONDCTION OVER SAME, CONSTANT HEAT TRANSFER BOUNDARY CONDITION

```
      Program main

!This program solves 3D, transient heat transfer in a solid tissue
mimic
!next to a blood flow mimic with both on top of the same temperature
!boundary condition. This scenario assumes constant material
properties
!(i.e. heat capacity, thermal conductivity, density, and viscosity).
!Thus, the momentum and continuity equations can be decoupled from
the
!energy equation and solved separately. The exact velocity field is
!supplied to the energy equation by assuming Poiseuille flow in 2D
!(y and z), i.e. du/dx=0.
!Blood is assumed to have the thermal properties of water
!Solid tissue is assumed to have the thermal properties of
!~8% poly(vinyl alcohol) tissue mimic
!
!VARIABLES and PARAMETERS:
!xlen=length of channel and direction of fluid flow [=] m
!ydist=height of channel, direction perpendicular to temp BC [=] m
!zdep=depth of channel, direction parallel to temp BC [=]= m
!mu = viscosity of bloodm mimic [=] kg*m^-1*s^-1
!alphati = thermal diffusivity of tissue mimic [=] m^2*s^-1
!alphati = thermal diffusivity of blood mimic [=] m^2*s^-1
!kcon = tissue mimic thermal conductivity [=] W m^-1 °C^-1
!ktis = fluid mimic thermal conductivity [=] W m^-1 °C^-1
!t=time [=] s
!T=temperature [=] °C
!u = x-component velocity [=] m*s^-1
!Q = x-component volumetric flow rate [=] m^3*s^-1
!T0=initial temperature (at time, t=0)of entire system [=] °C
!Tbc =temperature boundary condition (t>0) [=] °C

!PHYSICAL GEOMETRY
!mimic(s) are modeled in a 2.54 by 2.54 cm cross-section flow cell
of
!length = 7.62 cm. This void is surrounded by a 0.3175 cm-thick wall
!assumed to have physical properties of acrylic (PMMA), the model
also
!includes a 1.27 layer of air completely surrounding the flow cell

!BOUNDARY CONDITIONS:
!no slip at all walls
!For fluid flow, T is constant at i=1 and allowed to float at i=imax
!T is constant at 23 °C at all air boundaries
!Constant temperature boundary condition is applied from i=1 to
i=imax
```

```
!and in the xz plan at the flow cell floor

!BEGIN CODE:

      Real*8Rwmax
      Integer wmax,imax,jmax,kmax

!wmax is number of nodes spanning y and z directions in the flow
cell !void (not including walls and air), jmax and kmax
!are the total number of nodes in the y and z direction including
!wmax, and the number of nodes across the walls and air surrounding
!the flow cell. Number of nodes in wall is equal to 1/8 of wmax
!and number of nodes in air is 1/2 wmax. Thus, wmax should be a
!multiple of 8

      Rwmax= 40
      wmax=int(Rwmax)
      imax=int(1.5*Rwmax)
      jmax=int(2.25*Rwmax)
      kmax=jmax

      Call Energy (wmax,imax,jmax,kmax)

      End

      Subroutine Energy (wmax,imax,jmax,kmax)
        Integer i,j,k,n,wmax,imax,jmax,kmax,maxits,kmaxbl
        Integer y1,y2,y3,y4,z1,z2,z3,z4,zprobe,zbound,Tk1,Tk2
        Integer ittotal,time
        Logical tolex
        Parameter (solved=0,limit=1)
        Real*8 xlen,ydist,zdep,delt,ttotal,delx,dely,delz
        Real*8 alphaair,alphawall,alphatis,alphabl,mu,ue,tol,Ti,Tbc
        Real*8 h,L,w,y,z,sum,Q,delP,pi,ktis,kbl,qprobe
        Real*8
T(imax,jmax,kmax),u(imax,jmax,kmax),kcon(imax,jmax,kmax)
        Real*8 alpha(imax,jmax,kmax),Tprobe(14),yT(14)

!Read parameter values
      y1=wmax/2   !end of air boundary
      y2=y1+wmax/8   !end of wall boundary
      y3=y2+wmax   !end of mimic boundary
      y4=y3+wmax/8  !end of second wall boundary
      z1=y1
      z2=y2
      z3=y3
      z4=y4
      zbound=z2+1+int(0.6*wmax)  !this is the node in the z-
direction
                     !that corresponds to the blood/tissue
interface
      xlen=0.0762
      ydist=0.05715
      zdep=0.05715
```

```
      delx=xlen/imax
      dely=ydist/jmax
      delz=zdep/kmax
      delt=0.005   !size of time step
      ttotal=300.0   !total time length of model in seconds
      ittotal=int(ttotal/delt)  !total number of iterations
      alphaair=2.16e-5
      alphawall=1.3e-8
      alphatis=1.41e-7
      ktis=0.578
      kbl=0.600
      kcon=0.0
      alphabl=1.44e-7
      mu=0.000894
      Q=0.20/1000.0/60.0  ! volumetric flow rate [=] m^3*s^-1
      Ti=24.0
      Tbc=37.0
      pi=4.0*atan(1.0)

!Initial conditions:
      u=0.0
      T=Ti

!y distance of flow cell probes
      Do i=1,7
        yT(i)=(y2+1)*dely-0.00005
      End Do
      yT(1)=yT(1)+0.00044+0.00005
      yT(2)=yT(2)+0.00140
      yT(3)=yT(3)+0.00213
      yT(4)=yT(4)+0.00425
      yT(5)=yT(5)+0.00747
      yT(6)=yT(6)+0.01334
      yT(7)=yT(7)+0.02191
      yT(8)=yT(1)+0.00044+0.0002
      yT(9)=yT(2)+0.00140
      yT(10)=yT(3)+0.00213
      yT(11)=yT(4)+0.00425
      yT(12)=yT(5)+0.00747
      yT(13)=yT(6)+0.01334
      yT(14)=yT(7)+0.02191



!Define flow field
      h=wmax*dely
      L=xlen
      w=wmax*0.6*dely
      sum=0.0
      Do n=0,100
        sum=sum+192.0*h/(pi)**5.0/w/(2.0*n+1.0)**5
     &      *tanh((2.0*n+1.0)*pi*w/2.0/h)
      End Do
      delP=Q*12*mu/w/h**3/(1-sum)
```

```
      Do i=1,imax
        Do j=y2+1,y3
            y=h/(float(y3-y2)-1.0)*float(j-y3)+h/2.0
          Do k=z2+1,zbound
            z=w/(float(z3-z2)-1.0)*float(k-z3)+w/2.0
            sum=0.0
            Do n=0,100
              sum=sum+32.0*(-1.0)**n*cosh((2.0*n+1.0)*pi*z/h)
     &            *cos((2*n+1.0)*pi*y/h)/(2.0*n+1.0)**3/(pi)**3
     &            /cosh((2.0*n+1.0)*pi*w/2.0/h)
            End Do
            u(i,j,k)=delP*h**2/8/mu/L*(1-4.0*y**2/h**2-sum)
          End Do
        End Do
      End Do

!Temperature boundary condition is underneath tissue mimic, thus the
!BC will be applied at T(i,y2+1,zbound+depth into tissue mimic in
!z-direction (designated as zprobe) in which driving probe in
!experimental setup is underneathmimic. The BC at all other k will
be !equal to the heat flux at this same point.

      zprobe=z2+1+int(0.015748/delz)+1
      Do i=1,imax
          T(i,y2+1,zprobe)=Tbc
      End Do

!Assign thermal diffusivity to grid
      Do i=1,imax
        Do j=1,y1
          Do k=1,kmax
            alpha(i,j,k)=alphaair
          End Do
        End Do
        Do j=y1+1,y2
          Do k=1,z1
            alpha(i,j,k)=alphaair
          End Do
          Do k=z1+1,z4
            alpha(i,j,k)=alphawall
          End Do
          Do k=z4+1,kmax
            alpha(i,j,k)=alphaair
          End Do
        End Do
        Do j=y2+1,y3
          Do k=1,z1
            alpha(i,j,k)=alphaair
          End Do
          Do k=z1+1,z2
            alpha(i,j,k)=alphawall
          End Do
          Do k=z2+1,zbound
            alpha(i,j,k)=alphabl
```

```
              kcon(i,j,k)=kbl
            End Do
            Do k=zbound+1,z3
              alpha(i,j,k)=alphatis
              kcon(i,j,k)=ktis
            End Do
            Do k=z3+1,z4
              alpha(i,j,k)=alphawall
            End Do
            Do k=z4+1,kmax
              alpha(i,j,k)=alphaair
            End Do
          End Do
          Do j=y3+1,y4
            Do k=1,z1
              alpha(i,j,k)=alphaair
            End Do
            Do k=z1+1,z4
              alpha(i,j,k)=alphawall
            End Do
            Do k=z4+1,kmax
              alpha(i,j,k)=alphaair
            End Do
          End Do
          Do j=y4+1,jmax
            Do k=1,kmax
              alpha(i,j,k)=alphaair
            End Do
          End Do
        End Do

!additional heat transfer boundary condition
        qprobe=(3.0*T(imax/2,y2+1,zprobe)-4.0* T(imax/2,y2+2,zprobe)
     &       +T(imax/2,y2+3,zprobe))*ktis/2.0/dely
        print*,qprobe
        Do i=2,imax-1
          Do k=z2+1,z3
            If (k.eq.zprobe) Then
              T(i,y2+1,k)=T(i,y2+1,k)
            Else
              T(i,y2+1,k)=(4.0*T(i,y2+2,k)-T(i,y2+3,k)+2.0*dely*qprobe
     &                    /kcon(i,y2+1,k))/3.0
            End If
          End Do
        End Do

!Begin time marching, calculate temp field at each time step
        Do time=1,ittotal
          print *, time*delt
          Do i=2,imax-1
            Do j=2,jmax-1
              Do k=2,kmax-1
                If (j.eq.y2+1.and.k.gt.z2+1.and.k.lt.z3+1) Then
                  T(i,j,k)=T(i,j,k)
```

```
               Else
                  T(i,j,k)=T(i,j,k)+delt*(alpha(i,j,k)*((T(i+1,j,k)-
     &          2.0*T(i,j,k)+T(i-1,j,k))/delx**2+(T(i,j+1,k)-
2.0*T(i,j,k)
     &          +T(i,j-1,k))/dely**2+(T(i,j,k+1)-2.0*T(i,j,k)
     &          +T(i,j,k-1))/delz**2)-(T(i+1,j,k)*u(i+1,j,k)-T(i-
1,j,k)*
     &           u(i-1,j,k))/(2.0*delx))
               End If
             End Do
           End Do
         End Do
         print *,T(13,3,28),T(13,22,28),T(13,28,28),T(13,jmax-1,28)
!         print *,T(13,16,15),T(13,16,28),T(13,16,41),T(13,16,kmax-1)

!update boundary conditions
!Temperature boundary conditions at air boundaries are constant
!T(imax,j,k)=T(imax-1,j,k)
       Do j=1,jmax
         Do k=1,kmax
           T(imax,j,k)=T(imax-1,j,k)
         End Do
       End Do

!Boundary condition at zprobe is Tbc, from this BC, q at zbound is
!calculated using one sided difference. From this q, T is calculated
at
!y2+1 in xz plane using one sided difference.

       qprobe=(3.0*T(imax/2,y2+1,zprobe)-4.0* T(imax/2,y2+2,zprobe)
     &        +T(imax/2,y2+3,zprobe))*ktis/2.0/dely
       Do i=2,imax
         Do k=z2+1,z3
           If (k.eq.zprobe) Then
             T(i,y2+1,k)=T(i,y2+1,k)
           Else
             T(i,y2+1,k)=(4.0*T(i,y2+2,k)-T(i,y2+3,k)+2.0*dely*qprobe
     &                   /kcon(i,y2+1,k))/3.0
           End If
         End Do
       End Do

!Export temp field to .csv file evey 5000 iterations
       If (mod(time,5000).eq.0.or.time.eq.1) Then
         Call logdata(imax,jmax,kmax,T,delt,time)
       End If

!Export transient temp profiles at probe locations every 100 time
steps
       If (mod(time,100).eq.0.) Then
         Open (3,File='transprobetemp56.csv')
   30    Format(15(F6.2,','))
         Tk1=int(z2+1+0.00691/delz)
         Tk2=int(z2+1+0.01849/delz)
```

```
         Do i=1,7
           Do j=1,jmax
             If(j*dely.lt.yT(i).and.(j+1)*dely.gt.yT(i)) Then
             Tprobe(i)=(T(imax/2,j+1,Tk1)-T(imax/2,j,Tk1))/j/dely
     &       *(yT(i)-j*dely)+T(imax/2,j,Tk1)
             End If
           End Do
         End Do
         Do i=8,14
           Do j=1,jmax
             If(j*dely.lt.yT(i).and.(j+1)*dely.gt.yT(i)) Then
             Tprobe(i)=(T(imax/2,j+1,Tk2)-T(imax/2,j,Tk2))/j/dely
     &       *(yT(i)-j*dely)+T(imax/2,j,Tk2)
             End If
           End Do
         End Do


write(3,30)delt*time,Tprobe(1),Tprobe(2),Tprobe(3),Tprobe(4),
     &
Tprobe(5),Tprobe(6),Tprobe(7),Tprobe(8),Tprobe(9),
     &             Tprobe(10),Tprobe(11),Tprobe(12),Tprobe(13),
     &             Tprobe(14)

      End If



      End Do
      End

!Data output subroutine

      Subroutine logdata(imax,jmax,kmax,T,delt,time)

      Real*8 T(imax,jmax,kmax)
      Real*8 delt
      Integer imax,jmax,kmax,time

        Open (1,File='2D_Tfieldxycomb56.csv')
        Open (2,File='2D_Tfieldyzcomb56.csv')
   10   Format(60(E12.4,','))
   20   Format(72(E12.4,','))
        write(1,*)delt*time
        Do j=1,jmax
        write(1,10)T(1,j,45),T(2,j,45),T(3,j,45),T(4,j,45),
     $     T(5,j,45),T(6,j,45),T(7,j,45),
     &     T(8,j,45),T(9,j,45),T(10,j,45),T(11,j,45),
     &     T(12,j,45),T(13,j,45),
     &     T(14,j,45),T(15,j,45),T(16,j,45),T(17,j,45),T(18,j,45),
     &     T(19,j,45),T(20,j,45),
     &     T(21,j,45),T(22,j,45),T(23,j,45),T(24,j,45),T(25,j,45),
     &     T(26,j,45),T(27,j,45),
     &     T(28,j,45),T(29,j,45),T(30,j,45),T(31,j,45),T(32,j,45),
```

```
     &     T(33,j,45),
     &     T(34,j,45),T(35,j,45),T(36,j,45),T(37,j,45),T(38,j,45),
     &     T(39,j,45),
     &     T(40,j,45),T(41,j,45),T(42,j,45),T(43,j,45),T(44,j,45),
     &     T(45,j,45),
     &     T(46,j,45),T(47,j,45),T(48,j,45),T(49,j,45),T(50,j,45),
     &     T(51,j,45),
     &     T(52,j,45),T(53,j,45),T(54,j,45),T(55,j,45),T(56,j,45),
     &     T(57,j,45), T(58,j,45), T(59,j,45), T(60,j,45)
      End Do
      write(2,*)delt*time
      Do j=1,jmax
      write(2,20)T(30,J,1),T(30,J,2),T(30,J,3),T(30,J,4),
     $     T(30,J,5),T(30,J,6),T(30,J,7),
     &     T(30,J,8),T(30,J,9),T(30,J,10),T(30,J,11),
     &     T(30,J,12),T(30,J,13),
     &     T(30,J,14),T(30,J,15),T(30,J,16),T(30,J,17),T(30,J,18),
     &     T(30,J,19),T(30,J,20),
     &     T(30,J,21),T(30,J,22),T(30,J,23),T(30,J,24),T(30,J,25),
     &     T(30,J,26),T(30,J,27),
     &     T(30,J,28),T(30,J,29),T(30,J,30),T(30,J,31),T(30,J,32),
     &     T(30,J,33),
     &     T(30,J,34),T(30,J,35),T(30,J,36),T(30,J,37),T(30,J,38),
     &     T(30,J,39),
     &     T(30,J,40),T(30,J,41),T(30,J,42),T(30,J,43),T(30,J,44),
     &     T(30,J,45),
     &     T(30,J,46),T(30,J,47),T(30,J,48),T(30,J,49),T(30,J,50),
     &     T(30,J,51),
     &     T(30,J,52),T(30,J,53),T(30,J,54),T(30,J,55),T(30,J,56),
     &     T(30,J,57),
     &     T(30,J,58),T(30,J,59),T(30,J,60),T(30,J,61),T(30,J,62),
     &     T(30,J,63),
     &     T(30,J,64),T(30,J,65),T(30,J,66),T(30,J,67),T(30,J,68),
     &     T(30,J,69),T(30,j,70),T(30,j,71),T(30,j,72)

      End Do
!        Close(1)
!        Close(2)
      End
```

APPENDIX D: FORTRAN CODE FOR THREE DIMENSIONAL, COMBINED CONVECTION, CONDCTION OVER SAME, CONSTANT TEMPERATURE BOUNDARY CONDITION

```
      Program main

!This program solves 3D, transient heat transfer in a solid tissue
mimic
!next to a blood flow mimic with both on top of the same temperature
!boundary condition. This scenario assumes constant material
properties
!(i.e. heat capacity, thermal conductivity, density, and viscosity).
!Thus, the momentum and continuity equations can be decoupled from
the
!energy equation and solved separately. The exact velocity field is
!supplied to the energy equation by assuming Poiseuille flow in 2D
!(y and z), i.e. du/dx=0.
!Blood is assumed to have the thermal properties of water
!Solid tissue is assumed to have the thermal properties of
!~8% poly(vinyl alcohol) tissue mimic
!
!VARIABLES and PARAMETERS:
!xlen=length of channel and direction of fluid flow [=] m
!ydist=height of channel, direction perpendicular to temp BC [=] m
!zdep=depth of channel, direction parallel to temp BC [=]= m
!mu = viscosity of bloodm mimic [=] kg*m^-1*s^-1
!alphati = thermal diffusivity of tissue mimic [=] m^2*s^-1
!alphati = thermal diffusivity of blood mimic [=] m^2*s^-1
!kcon = tissue mimic thermal conductivity [=] W m^-1 °C^-1
!ktis = fluid mimic thermal conductivity [=] W m^-1 °C^-1
!t=time [=] s
!T=temperature [=] °C
!u = x-component velocity [=] m*s^-1
!Q = x-component volumetric flow rate [=] m^3*s^-1
!T0=initial temperature (at time, t=0)of entire system [=] °C
!Tbc =temperature boundary condition (t>0) [=] °C

!PHYSICAL GEOMETRY
!mimic(s) are modeled in a 2.54 by 2.54 cm cross-section flow cell
of
!length = 7.62 cm. This void is surrounded by a 0.3175 cm-thick wall
!assumed to have physical properties of acrylic (PMMA), the model
also
!includes a 1.27 layer of air completely surrounding the flow cell

!BOUNDARY CONDITIONS:
!no slip at all walls
!For fluid flow, T is constant at i=1 and allowed to float at i=imax
!T is constant at 23 °C at all air boundaries
!Constant temperature boundary condition is applied from i=1 to
i=imax
```

```
!and in the xz plan at the flow cell floor

!BEGIN CODE:

      Real*8Rwmax
      Integer wmax,imax,jmax,kmax

!wmax is number of nodes spanning y and z directions in the flow
cell !void (not including walls and air), jmax and kmax
!are the total number of nodes in the y and z direction including
!wmax, and the number of nodes across the walls and air surrounding
!the flow cell. Number of nodes in wall is equal to 1/8 of wmax
!and number of nodes in air is 1/2 wmax. Thus, wmax should be a
!multiple of 8

      Rwmax= 40
      wmax=int(Rwmax)
      imax=int(1.5*Rwmax)
      jmax=int(2.25*Rwmax)
      kmax=jmax

      Call Energy (wmax,imax,jmax,kmax)

      End

      Subroutine Energy (wmax,imax,jmax,kmax)
        Integer i,j,k,n,wmax,imax,jmax,kmax,maxits,kmaxbl
        Integer y1,y2,y3,y4,z1,z2,z3,z4,zprobe,zbound,Tk1,Tk2
        Integer ittotal,time
        Logical tolex
        Parameter (solved=0,limit=1)
        Real*8 xlen,ydist,zdep,delt,ttotal,delx,dely,delz
        Real*8 alphaair,alphawall,alphatis,alphabl,mu,ue,tol,Ti,Tbc
        Real*8 h,L,w,y,z,sum,Q,delP,pi,ktis,kbl,qprobe
        Real*8
T(imax,jmax,kmax),u(imax,jmax,kmax),kcon(imax,jmax,kmax)
        Real*8 alpha(imax,jmax,kmax),Tprobe(14),yT(14),qz(kmax)

        Open (3,File='transprobetemp046.csv')
   30   Format(15(F6.2,','))
        Open (4,File='transqz046.csv')
   40   Format(41(F6.2,','))



!Read parameter values
      y1=wmax/2   !end of air boundary
      y2=y1+wmax/8   !end of wall boundary
      y3=y2+wmax   !end of mimic boundary
      y4=y3+wmax/8  !end of second wall boundary
      z1=y1
      z2=y2
      z3=y3
      z4=y4
```

```
      zbound=45  !this is the node in the z-direction
                        !that corresponds to the blood/tissue
interface
      xlen=0.0762
      ydist=0.05715
      zdep=0.05715
      delx=xlen/imax
      dely=ydist/jmax
      delz=zdep/kmax
      delt=0.005   !size of time step
      ttotal=300.0   !total time length of model in seconds
      ittotal=int(ttotal/delt)  !total number of iterations
      alphaair=2.16e-5
      alphawall=1.3e-8
      alphatis=1.41e-7
      ktis=0.578
      kbl=0.600
      kcon=0.0
      alphabl=1.44e-7
      mu=0.000894
      Q=0.20/1000.0/60.0  ! volumetric flow rate [=] m^3*s^-1
      Ti=37.0
      Tbc=50.0
      pi=4.0*atan(1.0)

!Initial conditions:
      u=0.0
      T=Ti
      Do k=z2+1,z3
        qz(k-z2)=float(k)
      End Do
        write(4,40)0.0,qz(1), qz(2), qz(3), qz(4), qz(5),
     &             qz(6), qz(7), qz(8), qz(9), qz(10),
     &             qz(11), qz(12), qz(13), qz(14),qz(15),
     &             qz(16), qz(17), qz(18), qz(19),qz(20),
     &             qz(21), qz(22), qz(23), qz(24),qz(25),
     &             qz(26), qz(27), qz(28), qz(29),qz(30),
     &             qz(31), qz(32), qz(33), qz(34),qz(35),
     &             qz(36), qz(37), qz(38), qz(39),qz(40)


!y distance of flow cell probes
      Do i=1,7
        yT(i)=(y2+1)*dely
      End Do
      yT(1)=yT(1)+0.00044+0.0002
      yT(2)=yT(2)+0.00140
      yT(3)=yT(3)+0.00213
      yT(4)=yT(4)+0.00425
      yT(5)=yT(5)+0.00747
      yT(6)=yT(6)+0.01334
      yT(7)=yT(7)+0.02191
      yT(8)=yT(1)+0.00044+0.0002
      yT(9)=yT(2)+0.00140
```

```
      yT(10)=yT(3)+0.00213
      yT(11)=yT(4)+0.00425
      yT(12)=yT(5)+0.00747
      yT(13)=yT(6)+0.01334
      yT(14)=yT(7)+0.02191



!Define flow field
      h=wmax*dely
      L=xlen
      w=wmax*0.6*dely
      sum=0.0
      Do n=0,100
        sum=sum+192.0*h/(pi)**5.0/w/(2.0*n+1.0)**5
     &       *tanh((2.0*n+1.0)*pi*w/2.0/h)
      End Do
      delP=Q*12*mu/w/h**3/(1-sum)
      Do i=1,imax
        Do j=y2+1,y3
            y=h/(float(y3-y2)-1.0)*float(j-y3)+h/2.0
          Do k=z2+1,zbound
            z=w/(float(z3-z2)-1.0)*float(k-z3)+w/2.0
            sum=0.0
            Do n=0,100
              sum=sum+32.0*(-1.0)**n*cosh((2.0*n+1.0)*pi*z/h)
     &            *cos((2*n+1.0)*pi*y/h)/(2.0*n+1.0)**3/(pi)**3
     &            /cosh((2.0*n+1.0)*pi*w/2.0/h)
            End Do
            u(i,j,k)=delP*h**2/8/mu/L*(1-4.0*y**2/h**2-sum)
          End Do
        End Do
      End Do

!Temperature boundary condition is underneath tissue mimic, thus the
!BC will be applied at T(i,y2+1,zbound+depth into tissue mimic in
!z-direction (designated as zprobe) in which driving probe in
!experimental setup is underneathmimic. The BC at all other k will
be !equal to the heat flux at this same point.

!      zprobe=45
      Do i=1,imax
        Do k=z2+1,z3
          T(i,y2+1,k)=Tbc
        End Do
      End Do

!Assign thermal diffusivity to grid
      Do i=1,imax
        Do j=1,y1
          Do k=1,kmax
            alpha(i,j,k)=alphaair
          End Do
        End Do
```

```
          Do j=y1+1,y2
            Do k=1,z1
              alpha(i,j,k)=alphaair
            End Do
            Do k=z1+1,z4
              alpha(i,j,k)=alphawall
            End Do
            Do k=z4+1,kmax
              alpha(i,j,k)=alphaair
            End Do
          End Do
          Do j=y2+1,y3
            Do k=1,z1
              alpha(i,j,k)=alphaair
            End Do
            Do k=z1+1,z2
              alpha(i,j,k)=alphawall
            End Do
            Do k=z2+1,zbound
              alpha(i,j,k)=alphabl
              kcon(i,j,k)=kbl
            End Do
            Do k=zbound+1,z3
              alpha(i,j,k)=alphatis
              kcon(i,j,k)=ktis
            End Do
            Do k=z3+1,z4
              alpha(i,j,k)=alphawall
            End Do
            Do k=z4+1,kmax
              alpha(i,j,k)=alphaair
            End Do
          End Do
          Do j=y3+1,y4
            Do k=1,z1
              alpha(i,j,k)=alphaair
            End Do
            Do k=z1+1,z4
              alpha(i,j,k)=alphawall
            End Do
            Do k=z4+1,kmax
              alpha(i,j,k)=alphaair
            End Do
          End Do
          Do j=y4+1,jmax
            Do k=1,kmax
              alpha(i,j,k)=alphaair
            End Do
          End Do
        End Do


!       qprobe=(3.0*T(imax/2,y2+1,zprobe)-4.0* T(imax/2,y2+2,zprobe)
!      &       +T(imax/2,y2+3,zprobe))*ktis/2.0/dely
```

```
!      print*,qprobe
!      Do i=2,imax-1
!        Do k=z2+1,z3
!          If (k.eq.zprobe) Then
!            T(i,y2+1,k)=T(i,y2+1,k)
!          Else
!            T(i,y2+1,k)=(4.0*T(i,y2+2,k)-
T(i,y2+3,k)+2.0*dely*qprobe
!     &                  /kcon(i,y2+1,k))/3.0
!          End If
!        End Do
!      End Do

!Begin time marching, calculate temp field at each time step
      Do time=1,ittotal
        print *, time*delt
        Do i=2,imax-1
          Do j=2,jmax-1
            Do k=2,kmax-1
              If (j.eq.y2+1.and.k.gt.z2+1.and.k.lt.z3+1) Then
                T(i,j,k)=T(i,j,k)
              Else
                 T(i,j,k)=T(i,j,k)+delt*(alpha(i,j,k)*((T(i+1,j,k)-
     &          2.0*T(i,j,k)+T(i-1,j,k))/delx**2+(T(i,j+1,k)-
2.0*T(i,j,k)
     &          +T(i,j-1,k))/dely**2+(T(i,j,k+1)-2.0*T(i,j,k)
     &          +T(i,j,k-1))/delz**2)-(T(i+1,j,k)*u(i+1,j,k)-T(i-
1,j,k)*
     &           u(i-1,j,k))/(2.0*delx))
              End If
            End Do
          End Do
        End Do
!        print *,T(13,3,28),T(13,22,28),T(13,28,28),T(13,jmax-1,28)
!        print *,T(13,16,15),T(13,16,28),T(13,16,41),T(13,16,kmax-1)

!update boundary conditions
!Temperature boundary conditions at air boundaries are constant
!Boundary conditions at flow cell ends (i=1 and i=imax) are periodic
for
!the conduction only scenario. For convection, T=constant at i=1 and
!T(imax,j,k)=T(imax-1,j,k)
      Do j=1,jmax
        Do k=1,kmax
          T(imax,j,k)=T(imax-1,j,k)
        End Do
      End Do

!Boundary condition at zprobe is Tbc, from this BC, q at zbound is
!calculated using one sided difference. From this q, T is calculated
at
!y2+1 in xz plane using one sided difference.

!      qprobe=(3.0*T(imax/2,y2+1,zprobe)-4.0* T(imax/2,y2+2,zprobe)
```

```
!     &       +T(imax/2,y2+3,zprobe))*ktis/2.0/dely
!      Do i=2,imax
!        Do k=z2+1,z3
!          If (k.eq.zprobe) Then
!            T(i,y2+1,k)=T(i,y2+1,k)
!          Else
!            T(i,y2+1,k)=(4.0*T(i,y2+2,k)-
T(i,y2+3,k)+2.0*dely*qprobe
!     &                  /kcon(i,y2+1,k))/3.0
!          End If
!        End Do
!      End Do

!Export temp field to .csv file evey 5000 iterations      If
(mod(time,5000).eq.0.or.time.eq.1) Then
        Call logdata(imax,jmax,kmax,T,delt,time)
      End If

!Export transient temp profiles at probe locations every 100 time
steps
      If (mod(time,100).eq.0.) Then
        Tk1=int(z2+1+0.00691/delz)
        Tk2=int(z2+1+0.01849/delz)
        Do i=1,7
          Do j=1,jmax
            If(j*dely.lt.yT(i).and.(j+1)*dely.gt.yT(i)) Then
            Tprobe(i)=(T(imax/2,j+1,Tk1)-T(imax/2,j,Tk1))/j/dely
     &      *(yT(i)-j*dely)+T(imax/2,j,Tk1)
            End If
          End Do
        End Do
        Do i=8,14
          Do j=1,jmax
            If(j*dely.lt.yT(i).and.(j+1)*dely.gt.yT(i)) Then
            Tprobe(i)=(T(imax/2,j+1,Tk2)-T(imax/2,j,Tk2))/j/dely
     &      *(yT(i)-j*dely)+T(imax/2,j,Tk2)
            End If
          End Do
        End Do


write(3,30)delt*time,Tprobe(1),Tprobe(2),Tprobe(3),Tprobe(4),
     &
Tprobe(5),Tprobe(6),Tprobe(7),Tprobe(8),Tprobe(9),
     &             Tprobe(10),Tprobe(11),Tprobe(12),Tprobe(13),
     &             Tprobe(14)

      End If

!output q as a function of z from z=z2+1 to z=z3 at x=imax/2,y=y2+1.
!q will have units of W*cm-2.

      If (time.eq.1.or.mod(time,int((ttotal/60/delt))).eq.0) Then
        Do k=z2+1,z3
```

```
          qz(k-z2)=(3.0*T(imax/2,y2+1,k)-4.0* T(imax/2,y2+2,k)
     &       +T(imax/2,y2+3,k))*kcon(imax/2,y2+1,k)/2.0/dely/10000.0
        End Do
        write(4,40)time*delt,qz(1), qz(2), qz(3), qz(4), qz(5),
     &             qz(6), qz(7), qz(8), qz(9), qz(10),
     &             qz(11), qz(12), qz(13), qz(14),qz(15),
     &             qz(16), qz(17), qz(18), qz(19),qz(20),
     &             qz(21), qz(22), qz(23), qz(24),qz(25),
     &             qz(26), qz(27), qz(28), qz(29),qz(30),
     &             qz(31), qz(32), qz(33), qz(34),qz(35),
     &             qz(36), qz(37), qz(38), qz(39),qz(40)
      End If



      End Do
      End

!Data output subroutine

      Subroutine logdata(imax,jmax,kmax,T,delt,time)

      Real*8 T(imax,jmax,kmax)
      Real*8 delt
      Integer imax,jmax,kmax,time

        Open (1,File='2D_Tfieldxy046.csv')
        Open (2,File='2D_Tfieldyz046.csv')
   10   Format(60(E12.4,','))
   20   Format(72(E12.4,','))
      write(1,*)delt*time
      Do j=1,jmax
      write(1,10)T(1,j,45),T(2,j,45),T(3,j,45),T(4,j,45),
     $     T(5,j,45),T(6,j,45),T(7,j,45),
     &     T(8,j,45),T(9,j,45),T(10,j,45),T(11,j,45),
     &     T(12,j,45),T(13,j,45),
     &     T(14,j,45),T(15,j,45),T(16,j,45),T(17,j,45),T(18,j,45),
     &     T(19,j,45),T(20,j,45),
     &     T(21,j,45),T(22,j,45),T(23,j,45),T(24,j,45),T(25,j,45),
     &     T(26,j,45),T(27,j,45),
     &     T(28,j,45),T(29,j,45),T(30,j,45),T(31,j,45),T(32,j,45),
     &     T(33,j,45),
     &     T(34,j,45),T(35,j,45),T(36,j,45),T(37,j,45),T(38,j,45),
     &     T(39,j,45),
     &     T(40,j,45),T(41,j,45),T(42,j,45),T(43,j,45),T(44,j,45),
     &     T(45,j,45),
     &     T(46,j,45),T(47,j,45),T(48,j,45),T(49,j,45),T(50,j,45),
     &     T(51,j,45),
     &     T(52,j,45),T(53,j,45),T(54,j,45),T(55,j,45),T(56,j,45),
     &     T(57,j,45), T(58,j,45), T(59,j,45), T(60,j,45)
      End Do
      write(2,*)delt*time
      Do j=1,jmax
      write(2,20)T(30,J,1),T(30,J,2),T(30,J,3),T(30,J,4),
```

```
     $     T(30,J,5),T(30,J,6),T(30,J,7),
     &     T(30,J,8),T(30,J,9),T(30,J,10),T(30,J,11),
     &     T(30,J,12),T(30,J,13),
     &     T(30,J,14),T(30,J,15),T(30,J,16),T(30,J,17),T(30,J,18),
     &     T(30,J,19),T(30,J,20),
     &     T(30,J,21),T(30,J,22),T(30,J,23),T(30,J,24),T(30,J,25),
     &     T(30,J,26),T(30,J,27),
     &     T(30,J,28),T(30,J,29),T(30,J,30),T(30,J,31),T(30,J,32),
     &     T(30,J,33),
     &     T(30,J,34),T(30,J,35),T(30,J,36),T(30,J,37),T(30,J,38),
     &     T(30,J,39),
     &     T(30,J,40),T(30,J,41),T(30,J,42),T(30,J,43),T(30,J,44),
     &     T(30,J,45),
     &     T(30,J,46),T(30,J,47),T(30,J,48),T(30,J,49),T(30,J,50),
     &     T(30,J,51),
     &     T(30,J,52),T(30,J,53),T(30,J,54),T(30,J,55),T(30,J,56),
     &     T(30,J,57),
     &     T(30,J,58),T(30,J,59),T(30,J,60),T(30,J,61),T(30,J,62),
     &     T(30,J,63),
     &     T(30,J,64),T(30,J,65),T(30,J,66),T(30,J,67),T(30,J,68),
     &     T(30,J,69),T(30,j,70),T(30,j,71),T(30,j,72)

      End Do
!        Close(1)
!        Close(2)
      End
```

APPENDIX E: FORTRAN CODE FOR SEMI-IMPLICIT PRESSURE LINKED EQUATIONS (SIMPLE) ALGORITHM FOR SOLVING FLUID FLOW IN INCOMPRESSIBLE FLUIDS

```
      Program SIMPLE

!This program uses the pressure correction technique to solve 3D
!incompressible flow on a rectangular grid
!Boundary conditions: v=u=w=pp=0 at (1,j), pp=0 at outflow (imax,j)
!exit, moving plate at (i,jmax) with x-direction velocity: u = ue
!no-slip boundary condition at (i,1)

!xlen=length of plate (upper and lower walls) [=] ft
!ydist=distance between plates [=] ft
!zdep=depth of channel [=]= ft
!rho = constant density [=]slug*ft^-3
!mu = viscosity [=] slug*ft^-1*s^-1
!ue = velocity of moving upper wall [=] ft*s^-1
!u = x-component velocity [=] ft*s^-1
!v = y-component velocity [=] ft*s^-1
!w = z-component velocity [=] ft*s^-1
!p = pressure
!pstar is the guessed value of p
!pp is the corrected pressure (p=pstar+pp)
!using a staggered grid with each dependent variable having its own
!indexing system. i.e.:
!           |        x          |          y          |          z
!u runs from i=2,imax-1 (even) | j=2,jmax-1 (even) | k=3,kmax-2
(odd)
!v runs from i=1,imax   (odd)  | j=1,jmax   (odd)  | k=1,kmax
(odd)
!w runs from i=3,imax-2 (odd)  | j=2,jmax-1 (even) | k=2,kmax-1
(even)
!p runs from i=3,imax-2 (odd)  | j=2,jmax-1 (even) | k=3,kmax-2
(odd)

! Declare Variables
        Integer i,j,k,imax,jmax,kmax,maxits,maxitssor,statussor
        Integer count,status,noofit,noofitsor
        Logical tolex
        Parameter (solved=0,limit=1)
        Real*8 rho,xlen,ydist,zdep,delt,mu,delx,dely,delz
        Real*8 vbar,vdbar,ubar,udbar,wbar,wdbar
        Real*8 astar,bstar,cstar,tol,tolsor,alphap,ue
        Real*8 jj,bb,cc,x,xx
        Real*8 u(35,23,79),v(35,23,79),w(35,23,79)
        Real*8
rhoustar(35,23,79),rhovstar(35,23,79),rhowstar(35,23,79)
        Real*8 p(35,23,79),pp(35,23,79),pstar(35,23,79)
        Real*8 ppsolved(35,23,79),e(35,23,79)
        Real*8 chcon(35,23,79)
```

```
! Read parameter values
      rho=998.0 ![=] kg*m^-3
      xlen=0.127 ![=] m
      ydist=0.0254 ![=] m
      zdep=0.0254 ![=] m
      delt=0.00001
      mu=0.000894 ![=] kg*m^-1*s^-1
      imax=35
      jmax=23
      kmax=79
      delx=xlen/((float(imax)-1.0)/2.0)
      dely=ydist/((float(jmax)-1.0)/2.0)
      delz=zdep/((float(kmax)-1.0)/2.0)
      ue=0.01030 ![=] m*s^-1
      maxits=100000 !max number of iterations
      tol=5.0e-10 !error when reached will stop the computation
      alphap=0.8

! Initiate grid
      u=0.0
      rhoustar=0.0
      v=0.0
      rhovstar=0.0
      w=0.0
      rhowstar=0.0
      p=0.0
      pstar=0.0
      pp=0.0
      e=0.0

!Apply boundary conditions
!boundary conditions on u
!no slip bc at walls, allowed to float at inflow and outflow bc
      Do i=2,imax-1,2
        Do j=4,jmax-3,2
          Do k=5,kmax-4,2
            jj=float(j)
            bb=(float(jmax-1)+2.0)
            cc=2.0*(float(jmax-1)+2.0)
            x=float(jmax)/2.0+0.5
            xx=(x**2.0-bb*x+cc)
            u(i,j,k)=ue*(jj**2.0-bb*jj+cc)/xx
          End Do
        End Do
      End Do
      Do i=2,imax-1,2
       Do j=2,jmax-1,2
         Do k=3,kmax-2,2
           rhoustar(i,j,k)=u(i,j,k)*rho
         End Do
       End Do
      End Do
```

```
!boundary conditions on v and w: no slip bc at all walls, allowed to
!float at outflow, v=w=0 at inflow (i=1)
!boundary conditions on pp are zero around entire volume,
!since all dependent variable matrices are initiated with values of
0.0,
!do not need to write any code, floating bcs will be updated at each
!iteration

!Pressure boundary condition at outlet is constant and smaller than
!inlet due to pressure drop
      Do j=2, jmax-1,2
       Do k=3, kmax-2,2
        p(imax-2,j,k)=p(3,j,k)-8.0*mu*ue/ydist**2.0*xlen
        pstar(imax-2,j,k)=pstar(3,j,k)-8.0*mu*ue/ydist**2.0*xlen
       End Do
      End Do

!start iteration
      Do count=1,maxits
        print *,count
        tolex=.false.
        print *, u(2,12,11),u(4,12,11),u(20,12,11)
        print *, e(3,12,11),e(5,12,11),e(21,12,11)


!solve for rhoustar, rhovstar, and rhowstar for all interior grid
points

!rhoustar:
        Do i=4,imax-3,2
          Do j=4,jmax-3,2
            Do k=5,kmax-4,2
              vbar=0.5*(v(i+1,j+1,k)+v(i-1,j+1,k))
              vdbar=0.5*(v(i+1,j-1,k)+v(i-1,j-1,k))
              wbar=0.5*(w(i+1,j,k+1)+w(i-1,j,k+1))
              wdbar=0.5*(w(i+1,j,k-1)+w(i-1,j,k-1))
              astar=-rho*((u(i+2,j,k)**2.0-u(i-
2,j,k)**2.0)/(2.0*delx)
     &                   +(u(i,j+2,k)*vbar-u(i,j-
2,k)*vdbar)/(2.0*dely)
     &                   +(u(i,j,k+2)*wbar-u(i,j,k-
2)*wdbar)/(2.0*delz))
     &              +mu*((u(i+2,j,k)-2.0*u(i,j,k)+u(i-
2,j,k))/delx**2.0
     &                   +(u(i,j+2,k)-2.0*u(i,j,k)+u(i,j-
2,k))/dely**2.0
     &                   +(u(i,j,k+2)-2.0*u(i,j,k)+u(i,j,k-
2))/delz**2.0)
              rhoustar(i,j,k)=rho*u(i,j,k)+astar*delt-delt/delx*
     &                    (pstar(i+1,j,k)-pstar(i-1,j,k))
            End Do
          End Do
        End Do
```

```
!rhovstar:
        Do i=3,imax-2,2
          Do j=3,jmax-2,2
            Do k=3,kmax-2,2
              ubar=0.5*(u(i+1,j+1,k)+u(i+1,j-1,k))
              udbar=0.5*(u(i-1,j+1,k)+u(i-1,j-1,k))
              wbar=0.5*(w(i,j+1,k+1)+w(i,j-1,k+1))
              wdbar=0.5*(w(i,j+1,k-1)+w(i,j-1,k-1))
              bstar=-rho*((v(i+2,j,k)*ubar-v(i-
2,j,k)*udbar)/(2.0*delx)
     &                  +(v(i,j+2,k)**2.0-v(i,j-
2,k)**2.0)/(2.0*dely)
     &                  +(v(i,j,k+2)*wbar-v(i,j,k-
2)*wdbar)/(2.0*delz))
     &              +mu*((v(i+2,j,k)-2.0*v(i,j,k)+v(i-
2,j,k))/delx**2.0
     &                  +(v(i,j+2,k)-2.0*v(i,j,k)+v(i,j-
2,k))/dely**2.0
     &                  +(v(i,j,k+2)-2.0*v(i,j,k)+v(i,j,k-
2))/delz**2.0)
              rhovstar(i,j,k)=rho*v(i,j,k)+bstar*delt-delt/dely*
     &                   (pstar(i,j+1,k)-pstar(i,j-1,k))
            End Do
          End Do
        End Do

!rhowstar:
        Do i=5,imax-4,2
          Do j=4,jmax-3,2
            Do k=4,kmax-3,2
              ubar=0.5*(u(i+1,j,k+1)+u(i+1,j,k-1))
              udbar=0.5*(u(i-1,j,k+1)+u(i-1,j,k-1))
              vbar=0.5*(w(i,j+1,k+1)+w(i,j+1,k-1))
              vdbar=0.5*(w(i,j-1,k+1)+w(i,j-1,k-1))
              cstar=-rho*((w(i+2,j,k)*ubar-w(i-
2,j,k)*udbar)/(2.0*delx)
     &                  +(w(i,j+2,k)*vbar-w(i,j-
2,k)*vdbar)/(2.0*dely)
     &                  +(w(i,j,k+2)**2.0-w(i,j,k-
2)**2.0)/(2.0*delz))
     &              +mu*((w(i+2,j,k)-2.0*w(i,j,k)+w(i-
2,j,k))/delx**2.0
     &                  +(w(i,j+2,k)-2.0*w(i,j,k)+w(i,j-
2,k))/dely**2.0
     &                  +(w(i,j,k+2)-2.0*w(i,j,k)+w(i,j,k-
2))/delz**2.0)
              rhowstar(i,j,k)=rho*w(i,j,k)+cstar*delt-delt/delz*
     &                   (pstar(i,j,k+1)-pstar(i,j,k-1))
            End Do
          End Do
        End Do

!update inflow and outflow boundary conditions for u, v, and w
        Do j=4,jmax-3,2
```

```
          Do k=5,kmax-4,2
            rhoustar(imax-1,j,k)=rhoustar(imax-3,j,k)
          End Do
        End Do
        Do j=3,jmax-2,2
          Do k=3,kmax-2,2
            rhovstar(imax,j,k)=rhovstar(imax-2,j,k)
          End Do
        End Do
        Do j=4,jmax-3,2
          Do k=4,kmax-3,2
            rhowstar(imax-1,j,k)=rhowstar(imax-3,j,k)
          End Do
        End Do

!using rhoustar, rhovstar, rhowstar, solve for the corrected
pressure
!(denoted as pp)using the pressure correction formula which is
solved
!using the successive overrelaxation subroutine (sor)

!prepare e matrix for sor subroutine
!e can be thought of as a mass source term and represents how far
the
!continuity equation deviates from the converged answer. Thus, e
will
!approach zero as the continuity equations converges.

        Do i=5,imax-4,2
          Do j=4,jmax-3,2
            Do k=5,kmax-4,2
              chcon(i,j,k)=e(i,j,k)
              e(i,j,k)=(rhoustar(i+1,j,k)-rhoustar(i-1,j,k))/delx
     &                +(rhovstar(i,j+1,k)-rhovstar(i,j-1,k))/dely
     &                +(rhowstar(i,j,k+1)-rhowstar(i,j,k-1))/delz
            End Do
          End Do
        End Do

!call subroutine sor to solve for pp
!tol is the tolerance that when reached, the solution is converged,
!sor will stop if tol is not reached by the time the max number of
!iterations (maxits) have been computed. Corrected pressure is
outputted
!in matrix ppsolved, noofitsor is the number of iterations computed
for
!convergence
        tolsor = 5e-5
        maxitssor=10000
        Call sor (imax,jmax,kmax,e,delx,dely,delz,delt,   !inputs
     &            tolsor,maxitssor,   !continued inputs
     &                   status,pp,noofitsor)   !ouputs

!update p with the corrected pressure from ppsolved
```

```
!alphap is an underrelaxation factor, this value can be adjusted if
the
!computation is converging slowly or is not converging
        alphap=0.2
        Do i=5,imax-4,2
          Do j=4,jmax-3,2
            Do k=5,kmax-4,2
              p(i,j,k)=pstar(i,j,k)+alphap*pp(i,j,k)
!check if solution has converged
              If (.not. tolex) Then
                If (abs(chcon(i,j,k)-e(i,j,k)).gt.tol) Then
                  tolex=.true.
                End If
              End If
!update pstar with new p values
              pstar(i,j,k)=p(i,j,k)
            End Do
          End Do
        End Do

!update pressure boundary conditions
        Do i=5,imax-4,2
          Do k=3,kmax-2,2
            pstar(i,2,k)=2.0*pstar(i,4,k)-pstar(i,6,k)
            pstar(i,jmax-1,k)=2.0*pstar(i,jmax-3,k)-
     &      pstar(i,jmax-5,k)
            pp(i,2,k)=2.0*pp(i,4,k)-pp(i,6,k)
            pp(i,jmax-1,k)=2.0*pp(i,jmax-3,k)-
     &      pp(i,jmax-5,k)
          End Do
        End Do

        Do i=5,imax-4,2
          Do j=4,jmax-3,2
            pstar(i,j,2)=2.0*pstar(i,j,4)-pstar(i,j,6)
            pstar(i,j,kmax-1)=2.0*pstar(i,j,kmax-3)-
     &      pstar(i,j,kmax-5)
            pp(i,j,2)=2.0*pp(i,j,4)-pp(i,j,6)
            pp(i,j,kmax-1)=2.0*pp(i,j,kmax-3)-
     &      pp(i,j,kmax-5)
          End Do
        End Do


!calculate new values for u and v from corrected pressure
        Do i=4,imax-3,2
          Do j=4,jmax-3,2
            Do k=5,kmax-4,2
              u(i,j,k)=(rhoustar(i,j,k)-delt/delx*(pp(i+1,j,k)
     &        -pp(i-1,j,k)))/rho
            End Do
          End Do
        End Do
        Do i=3,imax-2,2
```

```
          Do j=3,jmax-2,2
            Do k=3,kmax-2,2
              v(i,j,k)=(rhovstar(i,j,k)-delt/dely*(pp(i,j+1,k+1)
     &         -pp(i,j-1,k-1)))/rho
             End Do
            End Do
          End Do
          Do i=5,imax-4,2
            Do j=4,jmax-3,2
              Do k=4,kmax-3,2
                w(i,j,k)=(rhowstar(i,j,k)-delt/delz*(pp(i,j,k+1)
     &         -pp(i,j,k-1)))/rho
              End Do
            End Do
          End Do

!update boundaries
          Do j=4,jmax-3,2
            Do k=5,kmax-4,2
             u(imax-1,j,k)=u(imax-3,j,k)
            End Do
          End Do
          Do j=3,jmax-2,2
            Do k=3,kmax-2,2
              v(imax,j,k)=v(imax-2,j,k)
            End Do
          End Do
          Do j=4,jmax-3,2
            Do k=4,kmax-3,2
              w(imax-2,j,k)=w(imax-4,j,k)
            End Do
          End Do

!Export data to .csv file evey 500 iterations, overwriting the
previous
!file
        If (mod(count,500).eq.0) Then
!          Call logdata(imax,jmax,kmax,u,v,w,count)
        End If


!repeat calculation of p until solution converges
          If (count.gt.50) Then
            If (.not. tolex) Then
              status=solved
              go to 21
            End If
          End If
        End Do
        status=limit

21      If (status.eq.solved) noofit=count
!        Call logdata(imax,jmax,kmax,u,v,w,count)
```

```
      End

!Data output subroutine

      Subroutine logdata(imax,jmax,kmax,u,v,w,count)

      Real*8 u(imax,jmax,kmax),v(imax,jmax,kmax),w(imax,jmax,kmax)
      Integer imax,jmax,kmax,count

        Open (1,File='2D_ufieldxy.csv')
        Open (2,File='2D_ufieldxz.csv')
   10   Format(57(E12.4,','))
   20   Format(58(E12.4,','))
      write(1,*)count
      Do i=2,imax-1,2
      write(1,10)u(i,2,29),u(i,4,29),u(i,6,29),
     &           u(i,8,29),u(i,10,29),u(i,12,29),u(i,14,29),
     &           u(i,16,29),u(i,18,29),u(i,20,29),
     &          u(i,22,29),u(i,24,29),u(i,26,29),
     &          u(i,28,29),u(i,30,29),u(i,32,29),
     &          u(i,34,29),u(i,36,29),u(i,38,29),u(i,40,29),
     &          u(i,42,29),u(i,44,29),u(i,46,29),u(i,48,29),
     &          u(i,50,29),u(i,52,29),u(i,54,29)
     &          ,u(i,56,29),u(i,58,29)!,u(i,60,29),
!     &          u(i,62,29),u(i,64,29),u(i,66,29)
!     &          ,u(i,68,29),u(i,70,29),u(i,72,29),
!     &          u(i,74,29),u(i,76,29),u(i,78,29)
!     &          ,u(i,80,29),u(i,82,29),u(i,84,29),
!     &          u(i,86,29),u(i,88,29),u(i,90,29)
!     &          ,u(i,92,29),u(i,94,29),u(i,96,29),
!     &          u(i,98,29),u(i,100,29),u(i,102,29)
!     &          ,u(i,104,29),u(i,106,29),u(i,108,29),
!     &          u(i,110,29),u(i,112,29),u(i,114,29)
      End Do

      write(2,*)count
      Do i=2,imax-1,2
      write(2,10)u(i,30,1+2),u(i,30,1+4),u(i,30,1+6),
     &           u(i,30,1+8),u(i,30,1+10),u(i,30,1+12),u(i,30,1+14),
     &           u(i,30,1+16),u(i,30,1+18),u(i,30,1+20),
     &          u(i,30,1+22),u(i,30,1+24),u(i,30,1+26),
     &          u(i,30,1+28),u(i,30,1+30),u(i,30,1+32),
     &          u(i,30,1+34),u(i,30,1+36),u(i,30,1+38),u(i,30,1+40),
     &          u(i,30,1+42),u(i,30,1+44),u(i,30,1+46),u(i,30,1+48),
     &          u(i,30,1+50),u(i,30,1+52),u(i,30,1+54)
     &          ,u(i,30,1+56)!,u(i,30,1+58),u(i,30,1+60),
!     &          u(i,30,1+62),u(i,30,1+64),u(i,30,1+66)
!     &          ,u(i,30,1+68),u(i,30,1+70),u(i,30,1+72),
!     &          u(i,30,1+74),u(i,30,1+76),u(i,30,1+78)
!     &          ,u(i,30,1+80),u(i,30,1+82),u(i,30,1+84),
!     &          u(i,30,1+86),u(i,30,1+88),u(i,30,1+90)
!     &          ,u(i,30,1+92),u(i,30,1+94),u(i,30,1+96),
!     &          u(i,30,1+98),u(i,30,1+100),u(i,30,1+102)
!     &          ,u(i,30,1+104),u(i,30,1+106),u(i,30,1+108),
```

```
!     &          u(i,30,1+110),u(i,30,1+112),u(i,30,1+114)
      End Do

!      write(2,*)count
!      Do i=1,imax,2
!      write(2,20)v(i,1,29),v(i,3,29),v(i,5,29),
!     &           v(i,7,29),v(i,9,29),v(i,11,29),v(i,13,29),
!     &           v(i,15,29),v(i,17,29),v(i,19,29),
!     &           v(i,21,29),v(i,23,29),v(i,25,29),
!     &          v(i,27,29),v(i,29,29),v(i,31,29),
!     &          v(i,33,29),v(i,35,29),v(i,37,29),v(i,39,29)
!     &          ,v(i,41,29),v(i,43,29),v(i,45,29),
!     &          v(i,47,29),v(i,49,29),v(i,51,29)
!     &          ,v(i,53,29),v(i,55,29),v(i,57,29),
!     &          v(i,59,29)!,v(i,61,29),v(i,63,29)
!     &          ,v(i,65,29),v(i,67,29),v(i,69,29),
!     &          v(i,71,29),v(i,73,29),v(i,75,29)
!     &          ,v(i,77,29),v(i,79,29),v(i,81,29),
!     &          v(i,83,29),v(i,85,29),v(i,87,29)
!     &          ,v(i,89,29),v(i,91,29),v(i,93,29),
!     &          v(i,95,29),v(i,97,29),v(i,99,29)
!     &          ,v(i,101,29),v(i,103,29),v(i,105,29),
!     &          v(i,107,29),v(i,109,29),v(i,111,29)
!     &          ,v(i,113,29),v(i,115,29)
!      End Do
        Close(1)
        Close(2)
      End


!Successive over relaxation method
!This is an iterative technique that solves the pressure correction
!formula. Copied from Figure 5.25 p 177, "Numerical Methods
!with FORTRAN 77" by L.V. Atkinson et al.
!Modified by J. Coffel on 05.12.2016

      Subroutine sor (imax,jmax,kmax,e,delx,dely,delz,delt,
     &                tol,maxits,
     &                status,pp,noofit)

      Integer imax,jmax,kmax,count,i,j,k,limit,maxits,noofit,solved
      Integer status
      Real*8 tol,omega,sum,a,b,c,d,delx,dely,delz,delt
      Logical   tolex
      Parameter (solved=0,limit=1)
      Real*8      pp(imax,jmax,kmax),e(imax,jmax,kmax)

!Define parameters
      a=2.0*(delt/delx**2.0+delt/dely**2.0+delt/delz**2.0)
      b=-delt/delx**2.0
      c=-delt/dely**2.0
      d=-delt/delz**2.0
      omega=1.2566
! omega is the relaxation factor which is the amount the previous
```

```
!and current iterations are weighted to produce an average that is
!closer to the exact solution than the current iteration value
!alone. Omega is chosen arbitrarily as: 1.0< omega < 2.0

!initial starting values
      Do i=5,imax-4,2
        Do j=4,jmax-3,2
          Do k=5,kmax-4,2
            pp(i,j,k)=e(i,j,k)/a
          End Do
        End Do
      End Do

!start iteration
      Do count=1,maxits
        tolex=.false.
        Do i=5,imax-4,2
          Do j=4,jmax-3,2
            Do k=5,kmax-4,2
              sum=(-1.0/a)*(e(i,j,k)+b*(pp(i+2,j,k)+pp(i-2,j,k))
     &                              +c*(pp(i,j+2,k)+pp(i,j-2,k))
     &                              +d*(pp(i,j,k+2)+pp(i,j,k-2)))
              If (.not. tolex) then
                If (abs(sum-pp(i,j,k)).gt.abs(pp(i,j,k)*tol))
     &              tolex=.true.
              End If
              pp(i,j,k)= omega*sum+(1.0-omega)*pp(i,j,k)
            End Do
          End Do
        End Do
        If (.not. tolex) then
          status=solved
          go to 21
        End If
      End Do
      status=limit
      noofit=count
21    If (status.eq.solved) noofit=count

      End
```